Collisional dynamics of macroscopic particles in a viscous fluid

Thesis by

Gustavo Joseph

In Partial Fulfillment of the Requirements

for the Degree of

Doctor of Philosophy

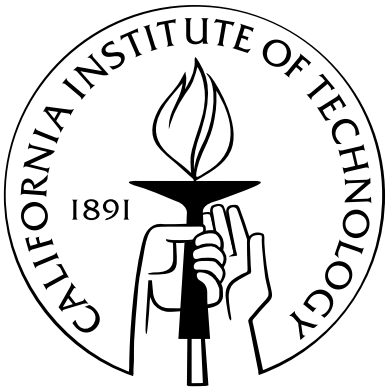

California Institute of Technology

Pasadena, California

2003

(Defended 22 May 2003)

Acknowledgements

First of all, I would like to thank Prof. Melany L. Hunt, my academic adviser during my stay at Caltech. Throughout the years she has been a source of invaluable wisdom, support, and friendship. For all her encouragement and guidance, I owe her a debt of gratitude.

I am also grateful to Dr. José Roberto Zenit Camacho, from whom I learned a simple way of looking at problems in order to extract non-trivial answers. From day one to D-day, he emphasized the importance of asking more questions than I wanted answered, and of letting the answers inspire new questions.

As a surrogate adviser and critical inquisitor, Prof. Christopher E. Brennen always found the time and energy to encourage me to press on. He has been an endless font of knowledge and enthusiasm.

Together with the aforementioned people, Prof. John F. Brady and Prof. Guruswami Ravichandran took time to review my Ph.D. dissertation and to serve on the committee. For their time and their insightful comments I remain ever thankful.

Back in 1998 I was going from door to door in the Thomas Laboratory, trying to find a glass paperweight that could be used as a thick target wall for my experiments. Prof. Paul C. Jennings had on a bookshelf a block of Zerodur—a piece of mirror from the W. M. Keck Observatory telescope—that he graciously lent me. It is no exaggeration to say that, without him, most of the work presented in this thesis would not have happened in its present form.

Lynn Burgess and Traci Provenzano made sure that sailing in the office was more often than not far smoother than sailing in the lab. Their support and enthusiasm as administrative assistants were pivotal during my graduate career. Funding and monies, ever necessary for supporting research, came from the California Institute of Technology, the Universidad Nacional Autónoma de México, and the National Science Foundation.

In Mexico, the sanity check was provided by my parents Pilar and Pedro and by my sister Mónica. They made sure I got where I am today, by laying a foundation on which they were certain anything could be built. In California, the sanity check outside Caltech was provided by Evelyn and Steve, my aunt and uncle. It has been said that, within the confines of Caltech, sanity has no place. I wouldn't go that far.

Indistinguishable to the untrained eye from the graduate students who have offices in the basement of Thomas, Prof. Charles S. Campbell, with his keen insights on science, politics, music, and literature alike, has expanded my horizons and provided hours of engaging and fruitful conversation.

As far as I can tell, Guillaume Lessard has always known just how far away to stay from jazz and liquor, and the Catalina Bar & Grill, The Jazz Bakery, and the Festival International de Jazz de Montréal can probably all attest to that end just as well as I can.

Patrick Hung's uncanny ability to carry a conversation without the introduction of any original material is something that I have admired for years. I sure hope he knows where his towel is. For Prashant K. Purohit I reserve the most obvious of acknowledgements: thanks, man! Michel Tanguay's theory and practice of stress management made many an afternoon and evening in Thomas all the more exquisite.

Special thanks go to Daniel M. Zimmerman, my suitemate in Avery House for almost a lustrum. A couple of years ago I spent some time proofreading one draft of his dissertation. In an editorial frenzy, armed with a purple pen, Dan chose to proofread several incarnations of my dissertation... and Guillaume's, and Patrick's.

Vilia and Jonas Zmuidzinas, and their daughters Regina and Lina, hold a dear place in my heart. Aside from my fellow students, it is they with whom I have spent the most precious times. Father Brian K. Muzas, Athena Castro, and so many other people who have touched my life outside academia at Caltech, complete the group of sanity checkers.

It would probably take too many lines to list the names of all the undergraduate students that made a difference during my stay at Caltech, both in Avery House and the Caltech Y. Of them, I have this to say: "They were playing Wagner. It's the most fun I've had in about six months."[1]

[1]Tyr Anasazi in Gene Roddenberry's Andromeda: "The Mathematics of Tears."

Abstract

This thesis presents experimental measurements of the approach and rebound of a particle colliding with a wall in a viscous fluid. Steel, glass, nylon, and Delrin particles were used, with diameters ranging from 3 to 12 mm. The experiments were performed using a thick Zerodur or Lucite wall with various mixtures of glycerol and water. Normal and tangential coefficients of restitution were defined from the ratios of the respective velocity components at the point of contact just prior to and after impact. These coefficients account for losses due to lubrication effects and inelasticity.

The experiments clearly show that the rebound velocity depends strongly on the impact Stokes number and weakly on the elastic properties of the materials. Below a Stokes number of approximately 10, no rebound of the particle occurs. Above a Stokes number of approximately 500, the normal coefficient of restitution asymptotically approaches the value for a dry collision. The data collapse onto a single curve of restitution coefficient as a function of Stokes number when normalized by the dry coefficient of restitution.

Oblique collisions in a fluid are qualitatively similar to oblique collisions in a dry system, with a lowered friction coefficient dependent on surface roughness. For smooth surfaces the friction coefficient is drastically reduced due to lubrication effects. Values for the friction coefficient are predicted based on elastohydrodynamic lubrication theory. The particle surface roughness was found to affect the repeatability of some measurements, especially for low impact velocities.

A significant retardation of a particle approaching a target at a low Stokes number was observed and quantified. The distance at which the particle's trajectory varies due to the presence of the wall is dependent on the impact Stokes number. The observed slowdown can be predicted from hydrodynamic theory to a good approximation.

An analysis of the erosion of ductile materials during immersed collisions is presented. The size of the crater formed by the impact of a single particle against a ductile target can be estimated from theory, and these estimates agree well with experimental measurements.

Contents

Tables

Figures

Nomenclature

Latin characters

a	Hertz contact radius
b	Target block thickness
C	Pressure–viscosity coefficient, Chu–Cameron power law
c	Specific heat
d_c	Crater diameter
d_p	Sphere diameter
E	Young's modulus
e	Coefficient of restitution
$\bar{e}$	Mean coefficient of restitution
E^*	Reduced elastic modulus
F	Tangential force of contact
f	Tangential force
G	Shear modulus
G^*	Reduced shear modulus
H	Plastic deformation crater depth

h Gap separation

h_m Minimum distance of approach

h_w Maximum distance of significant wall effect

I Moment of inertia

$\vec{J}$ Impulse due to collision

K Nondimensional radius of gyration

K_s Torsional stiffness of a string

M Mass of a sphere

M^* Reduced mass

$\hat{n}$ Unit vector joining the centers of two spheres

p Pressure

p_0 Pressure parameter, $\left[1-(1+Cp)^{-15}\right]/15C$; see §4.4.2

p_d Dynamic yield pressure

$p_{\max}$ Maximum pressure of contact

Q Viscous heat of impact

Q_p Plastic deformation energy

R Radius of a sphere

r Radial coordinate

Re Reynolds number

St Stokes number

T Torque

T^* Torque coefficient; see equation (4.19)

U Translational velocity parallel to a wall

$\vec{v}$ Relative velocity of two spheres at the point of contact

V Velocity

v_i Impact velocity

v_r Rebound velocity

W Equivalent load due to impact

x_0, x_1 Elastic length scales; see Davis *et al.* (1986)

Greek characters

α_{in} Local angle of incidence

α_{out} Local angle of rebound

α^* Pressure–viscosity coefficient, Barus's exponential law

β Rotational coefficient of restitution

ϵ Elasticity parameter, $4\mu v_i R^{3/2}/\pi E^* x_0^{5/2}$; see Davis *et al.* (1986)

ε Sphericity

$\Delta\theta$ Temperature increase due to impact

λ Correction to Stokes's law due to a wall; see Brenner (1961)

λ_p Surface roughness correlation distance

μ Viscosity

μ_0 Viscosity at atmospheric pressure

μ_f Coefficient of sliding friction

ν Poisson's ratio

ρ_f Fluid density

ρ_p Particle density

σ_{el} Elastic limit stress

$\sigma_{\max}$ Maximum stress

σ_s Root-mean-square surface roughness

σ_y Yield strength

τ Period of an elastic collision

τ_p Period of a plastic collision

ϕ High Reynolds number correction to drag; see Clift *et al.* (1978)

χ Modified radius of gyration

ψ Nondimensional local angle of contact

Ψ_{in} Effective nondimensional angle of incidence

Ψ_{out} Effective nondimensional angle of rebound

ω Angular velocity

Chapter 1

Introduction

The mechanisms of impact and rebound of solid particles in a multi-phase system are of interest over a wide range of application areas. The oil industry, for instance, routinely relies on the transport and deposition of macroscopic particles during drilling operations. The ability to determine the location at which proppant particles will stop is fundamental to the success of hydraulic fracturing techniques (Smith and Hannah, 1996), since the solid particles are responsible for keeping the fracture open once the pressure of the fracturing fluid is lowered. The sand and rock fragments formed during drilling pose a problem of their own: as the drilling fluid carries these particulates back into the machinery, they impact upon pipe walls and pump components, causing considerable erosion. Many industrial processes suffer from this same slurry erosion mechanism.

There have been many studies reported on the erosion of materials by impacting particles. Finnie (1960) and Bitter (1963) developed models for determining the mass of surface material removed by the impact of a single particle. In practice, two types of wear occur simultaneously, one caused by the cutting action of free-moving particles and another caused by the repeated plastic deformation of the surfaces (which eventually results in fracture or breakage). As shown by Magnée (1995), the cutting action of the particles is more important for ductile materials, while deformation is more significant for brittle materials.

In slurry erosion—where many particles hit a container surface and cause wear—the parameter usually linked to the erosion damage rate is the kinetic energy of the particles. Any modeling of these flows requires a detailed understanding of the mechanics of individual collisions. In dry granular flows where the effect of the interstitial fluid is negligible, the en-

ergy dissipation due to the inelasticity of the contacts is often characterized by a coefficient of restitution, e, defined by the ratio of the rebound velocity v_r to the impact velocity v_i,

$$e = -\frac{v_r}{v_i}. \tag{1.1}$$

In a similar manner, an effective coefficient of restitution may be useful in describing a collision in which the effects of the interstitial fluid are important. Such a coefficient must account for the viscous dissipation and the kinetic energy needed to displace the fluid between the surfaces, in addition to the inelasticity of the contact.

1.1 Coefficient of restitution

"Two seemingly identical black spheres, with marked differences in their physical properties. They have the same density, mass, color and appearance; yet when dropped to the floor, one jumps wildly, the other is motionless." This is the text with which Edmund Scientific advertises their *Happy and Unhappy Balls* product (Edmund Scientific, 2003). Contrary to what is usually expected of a rubber ball, when the unhappy ball is dropped vertically onto the floor, it stops dead without bouncing. On the other hand, the happy ball bounces to a height almost equal to the drop height. If one were to test the elastic properties of as a hard floor and a soft membrane under tension by bouncing a happy ball on them, the ball would bounce equally well on both surfaces. One might be tempted to conclude that the surfaces have comparable properties. The differences between the two are much more obvious when one also tests the surfaces using an unhappy ball, since the latter only bounces appreciably from the stretched membrane. However, this test alone does not indicate whether the energy loss occurs mainly in the floor or mainly in the ball.

An interesting experiment is to collide a happy ball with an unhappy ball, since the physics of this type of collision is relevant to problems in the physics of sports where a ball is struck by a bat or club or racquet. The particularities of a ball's construction undoubtedly affect the ball's coefficient of restitution. Take, for instance, the average coefficient of restitution of an American or National League baseball from 1924 through 1942. Those balls had

rubber-cushioned cork centers and a coefficient of restitution of 0.46 ± 0.01 (Briggs, 1945). To stretch the supply of rubber, in 1943 the American and National Leagues substituted balata cork centers for the rubber-cushioned cork centers that had been used in baseballs before World War II. The coefficient of restitution of the official balls in 1943 dropped to 0.40 ± 0.01, from which Briggs concluded that a hard-hit fly ball with a 1943 center might be expected to fall about 30 feet shorter than a pre-war ball hit under the same conditions. A modern-day Major League baseball[1] is required to have a coefficient of restitution of 0.546 ± 0.032 (Adair, 2002).

The construction of a ball, however, is not the only factor that affects its rebound. The playing surface is equally important. Tennis players and commentators universally agree that balls bounce much more slowly and much higher off a clay court than off grass, despite the fact that calculations based on available data show that the differences should be relatively small. In tennis, a difference of 1% in ball speed can translate to a difference of several feet in ball position, so a 1% difference can win or lose a match. In baseball, a wet outfield can cause the ball to be less lively or to bounce in an unexpected direction, providing a runner with enough time to score the winning run.

The first theoretical treatment of the impact and rebound of two solid objects is due to St.-Venant, who suggested that the total period of a collision is given by the time that it takes a compressive wave to travel across the solid and be reflected back (Love, 1927, §284). While this approximation is applicable when the bodies are relatively long, the collision of small bodies is in general determined by the deformation of the regions of contact. In a dry system, if the deformations are elastic, the process can be described by the Hertz contact theory (Timoshenko and Goodier, 1970, §140). In the more general case, where some plastic deformation occurs, the collision period is further prolonged.

According to Hertzian theory, the maximum radius of contact a of a sphere of density ρ_p and radius R normally impacting an elastic half-space at a velocity V is given by

$$a = \left(\frac{3RW}{4E^*} \right)^{1/3}, \tag{1.2}$$

[1]Since the 2000 season, there is no distinction between American and National League baseballs. All official balls are now labeled Major League Baseball.

where W is the equivalent load due to the impact and is obtained from

$$W = \frac{4}{3} R^2 E^* \left(\frac{5\pi}{4E^*} \rho_p V^2 \right)^{3/5}. \tag{1.3}$$

The reduced modulus $E^* = \left[\left(1-\nu_1^2\right)/E_1 + \left(1-\nu_2^2\right)/E_2 \right]^{-1}$ is a function of the Young's moduli E_1, E_2 and Poisson's ratios ν_1, ν_2 of the two bodies. The period τ of a collision under these conditions is given by

$$\tau = \frac{2\sqrt{\pi}\,\Gamma\left(\frac{7}{5}\right)}{\Gamma\left(\frac{9}{10}\right)} \frac{a^2}{VR} \approx 2.87 \left(\frac{M^2}{RE^{*2}V} \right)^{1/5}, \tag{1.4}$$

where $M = \frac{4}{3}\rho_p \pi R^3$ is the mass of the particle. The collision time τ is on the order of microseconds for elastic collisions of glass or metal objects a few centimeters in size. In those materials, the velocity of a compressive wave is generally in excess of $1000\,\mathrm{m\,s^{-1}}$.

For collisions where plastic deformation occurs, the total time of impact is the sum of two times: the time of elastic rebound, τ, given by equation (1.4) and the time of plastic indentation, τ_p. The latter can be estimated by assuming that the plastic deformation occurs under a dynamic pressure, p_d, proportional to the yield strength of the material (Johnson, 1985, §11.5). This assumption leads to a plastic indentation time,

$$\tau_p = \left(\frac{\pi M}{8 R p_d} \right)^{1/2}, \tag{1.5}$$

which is independent of the impact velocity. For a hard metallic object of a few centimeters in size colliding with a softer metal wall, τ_p is on the order of a few hundred microseconds.

This thesis is an examination of the effect that an interstitial fluid has on the rebound of a sphere, be it a ball on a wet field or a solid particle in a multi-phase flow. Due to the importance of fully-immersed systems to industrial processes, the emphasis is placed on the latter. In discrete element simulations of dry flows, the coefficients of restitution are used as input parameters to model the collision of two particles or the collision between a particle and a wall. In general, constant coefficients of restitution are assumed, although it is possible to allow the coefficients to vary. The values, however, are often obtained from idealized

experiments that may not be representative of the conditions encountered in applications.

The knowledge of an effective coefficient of restitution that accounts for the combined effects of the interstitial fluid and the inelasticity of the contact would be useful for numerical simulations of liquid–solid flows, such as those found in the studies by Hu (1996), Glowinski *et al.* (1999), Nguyen and Ladd (2002), and ten Cate *et al.* (2002). In these simulations, the motion of the interstitial fluid is calculated directly; however, the solid surfaces are not allowed to touch because contact would break the lattice modeling of the fluid. When two solid particles come within one grid spacing, fluid nodes are excluded from regions between the solid surfaces, leading to a loss of mass conservation. A repulsive force between the particles is incorporated to prevent contact between solid surfaces. Potapov, Hunt, and Campbell (2001) proposed a combination of smoothed particle hydrodynamics (SPH) and the discrete element method to model flows containing macroscopic solid particles in a viscous liquid. Their SPH model breaks down when the solid particle separation becomes smaller than a kernel width, since a mono-layer of smoothed fluid particles becomes trapped between the solid surfaces. A model based on an effective coefficient of restitution could be used to approximate the solid contacts in liquid–solid flow simulations, significantly improving computational efficiency.

1.2 Liquid-immersed collisions

The problem of a sphere of mass M moving in a fluid toward a surface or toward another sphere has been studied by many researchers. Brenner (1961) analyzed the problem of a sphere moving toward a wall at small Reynolds number ($Re = \rho_f v_i d_p/\mu$, where ρ_f is the fluid density, v_i is the approach velocity, d_p is the reduced particle diameter, and μ is the fluid dynamic viscosity) and found that the hydrodynamic force diverges as the gap separation, h, tends to zero; therefore, in the absence of elasticity of the particles or of the fluid, a rebound of the particles would not be possible. In a later study by Davis, Serayssol, and Hinch (1986), the particle surfaces are allowed to deform elastically due to the increase in hydrodynamic pressure. As a result, some of the incoming kinetic energy of the particle is stored as elastic strain energy. This strain energy is released after the particle comes to rest,

resulting in a rebound of the particles. However, since fluid always remains in the gap between the particles, physical contact between surfaces does not occur. The results from their analysis showed that the maximum particle deformation and the rebound of the particle after collision (measured in terms of the ratio of the rebound velocity v_r to the approach velocity v_i), depend on the particle Stokes number, $St = Mv_i/6\pi\mu R^2 = (1/9)Re(\rho_p/\rho_f)$ and an elasticity parameter, $\epsilon = 4\mu v_i R^{3/2}/\pi E^* x_0^{5/2}$, where x_0 is the position within the gap between the undeformed surfaces at which the velocity is v_i, and $R = d_p/2$ is the particle radius. Since their analysis assumes that the Reynolds number based on the distance x_0 is much less than one, the results are independent of the fluid density.

Barnocky and Davis (1989) extended the analysis of Davis *et al.* (1986) to include the variation of the density and viscosity with pressure. They observed that an increase in the density of the fluid during compression could enhance the rebound of an impacting particle, even when the particle was completely rigid. The increase in viscosity with pressure results in the fluid behaving like an elastic solid, significantly affecting the deformation of an elastic particle and enhancing the rebound of the particle from a surface. The perturbation analysis by Kytömaa and Schmid (1992) examined the effect of fluid compressibility on a collision between two particles by assuming that the solid is incompressible. Using a linear representation for the density dependence on pressure, the particles do not rebound. However, they conjecture that a nonlinear dependence of the density on pressure might result in a rebound of the particles even when the particles are incompressible.

As pointed out by Smart and Leighton (1989), the thickness of the lubrication layer between two colliding particles is very small, and may be on the order of the size of the surface roughness. They argued that surface roughness may have a significant impact on models based on perfectly smooth particles, because contact may occur through microscopic surface imperfections.

Lundberg and Shen (1992) obtained experimental measurements of the coefficient of restitution for the case when a drop of fluid was placed in the gap between a sphere and a surface. Davis, Rager, and Good (2002) and Barnocky and Davis (1988) performed measurements of the apparent coefficient of restitution for the collision of spheres with a flat surface overlaid with a thin layer of viscous fluid. Their results show a critical Stokes num-

ber above which rebound occurs. For smooth surfaces, this critical Stokes number varies from approximately 0.25 to approximately 4. The data presented by Davis *et al.* (2002) collapse fairly well onto a single master curve, obtained from lubrication theory and scaling arguments.

Three experimental studies have examined the rebound of a particle falling at its terminal velocity and impacting a submerged surface. McLaughlin (1968), Gondret *et al.* (1999) and Gondret, Lance, and Petit (2002) dropped particles in a tank filled with various viscous fluids to study the transition from arrest to rebound. McLaughlin used steel spheres of different diameters in glycerol–water mixtures and a thick steel anvil as a target. Gondret *et al.* (1999) used glass beads and steel spheres in water, glycerol, and silicone oil; the surface was a relatively thin glass plate, twice as thick as the diameter of their largest particle. In a later study by Gondret *et al.* (2002), the target surface was thicker and particles of tungsten carbide, stainless steel, soda glass, Teflon, Delrin[2], polyurethane, and nylon were used. In all three studies, the authors observed that there was no rebound of the particle for Stokes numbers below a certain threshold. Gondret *et al.* (1999) reported no rebound at $St = 12$, but did report a rebound at $St = 29$, which was obtained with a steel ball falling in silicone oil. McLaughlin reported no rebound at $St = 10$, but did report a rebound at $St = 19$. Neither McLaughlin nor Gondret *et al.* (1999) reported data for Reynolds numbers from approximately 150 to 5000. As noted by McLaughlin, the motion of the falling particle was erratic due to the shedding of vortex rings in the wake of the sphere. Gondret *et al.* (2002) reported measurements for a range of Reynolds numbers of approximately 2 to 2000; no rebound was reported for $St = 12$, but rebound did occur at slightly higher Stokes numbers.

The results published by Joseph *et al.* (2001) constitute the bulk of Chapter 3 of the present thesis. Normal collisions of spheres with a wall immersed in a liquid were performed by means of a pendulum device. Joseph *et al.* observed no rebound for $St \approx 10$ or lower. The repeatability of the experiments was found to be dependent on the surface roughness of the materials, in particular for $St < 80$. For higher impact velocities the coefficient of restitution asymptotically approached the value for dry collisions.

In a related study by Zhang *et al.* (1999), spheres were dropped onto a stationary sphere

[2]Teflon® and Delrin® are registered trademarks of E. I. du Pont de Nemours and Company.

in a liquid such that both collinear and oblique collisions could be achieved. Their measurements were favorably contrasted with lattice-Boltzmann simulations and with a mechanistic model that describes the collision process.

1.3 Thesis outline

The goal of the research documented in this thesis is to investigate the fundamental mechanics of the collision of solid objects immersed in fluid. In particular, the work focuses on the effects of a surrounding liquid on the rebound of a single sphere impacting a flat wall, both perpendicularly and obliquely. A summary of the current literature that describes solid–liquid interaction during rebound has been presented above.

The work presented in the thesis is largely experimental, and Chapter 2 provides a description of the experimental apparatus used. The characterization of the different components of the experimental device and a description of the experimental technique are also presented.

Chapter 3 concentrates on experiments performed for particle trajectories normal to the impacted wall; collisions where the particle impacts obliquely with the wall are presented in Chapter 4. Theoretical models are developed to contrast the results of the immersed collisions with results of dry collisions from the literature.

The proper characterization of particle collisions in a liquid depends upon the ability to accurately predict the particle velocity upon contact. Chapter 5 analyzes the effect of a wall on the velocity of a particle, both experimentally and theoretically, with good agreement between the two.

The theoretical models from Chapters 3 and 5 are used in Chapter 6 as a basis for predicting the wear caused by repeated deformation of a surface as a consequence of the impact of free-moving particles in a flow.

A summary of the present work and some future directions are presented in Chapter 7. The possibility of using the obtained models as a basis for numerical simulations of the interaction of multiple particles is also discussed.

Chapter 2

Experimental setup

A pendulum configuration like the one proposed by Zenit and Hunt (1999) was used to control the trajectory of a particle colliding with a wall in a viscous fluid. The impact velocity was controlled by varying the initial inclination angle. The resulting collisions were monitored using a high-speed digital video camera. The experiments were performed in glycerol–water mixtures with viscosities ranging from 1 to 60×10^{-3} Pa $\cdot$ s and with particles ranging from 3 to 13 mm in diameter. The particle–fluid density ratio was between 1.1 and 7.8. With these parameters, the Stokes number defined using the velocity just prior to impact ranged from 10 to approximately 2000. For validation purposes, some experiments were also performed in air.

2.1 Description of the apparatus

A fine nylon string of diameter between 50 and 130 µm was attached to a sphere that was positioned at an initial angle ϕ_i with respect to the vertical. The particle was then released without rotation from a pair of nylon- or Teflon-lined tweezers. The wall was positioned such that contact occurred at $\phi = 0$. To examine oblique collisions, the azimuthal orientation of the wall was adjusted such that its normal formed an angle α with the plane of the pendulum. A schematic representation of the experimental setup is shown in Figure 2.1.

A Redlake *Motion*Scope® 8000S monochrome high-speed digital camera (Redlake, 2002) was used to capture the trajectories of the spheres. The movies obtained from the camera were archived on **S-VHS** tape for subsequent processing. Most of the experiments were

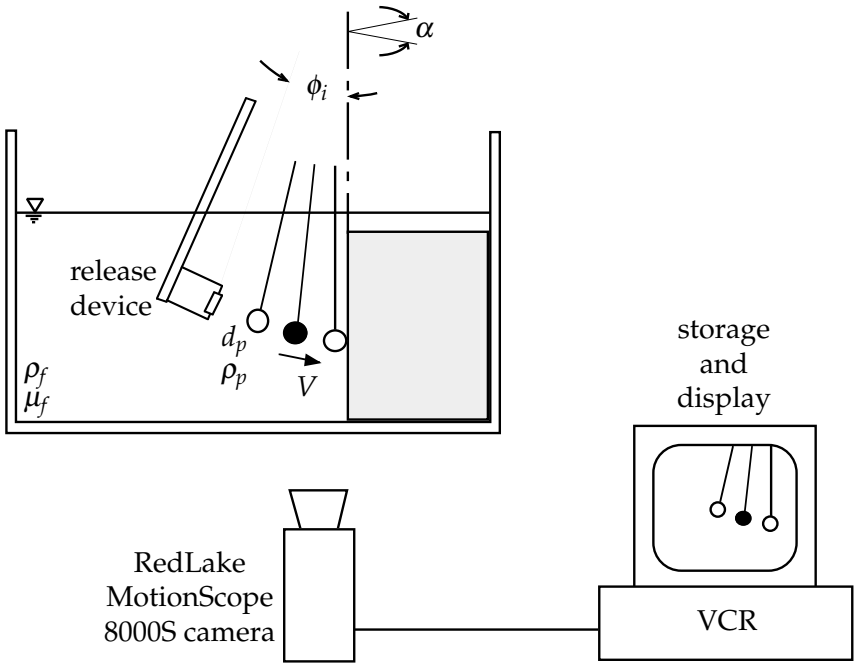

Figure 2.1: Schematic representation of the experimental setup.

recorded at 1000 frames per second. In the majority of cases the sampling resolution was 240×210 8-bit pixels. The setup was such that for the experiments involving normal collisions (Chapter 3) the focal plane of the high-speed camera was parallel to the plane of the pendulum. Oblique collisions (Chapter 4) were recorded from below, as shown in Figure 2.1, so that the deviation from the normal could be quantified.

The necessary illumination for high-speed video recording was provided by two 250 W Lowel Pro-light focusing halogen spotlights. The heat generated by these lamps was sufficient to noticeably warm up the liquid in the tank. The spotlights were left off in order to minimize this heating, except for a short time before each experimental run to allow for the light intensity to stabilize.

The mechanical and geometrical properties of the various components of the experimental apparatus are characterized in the following sections.

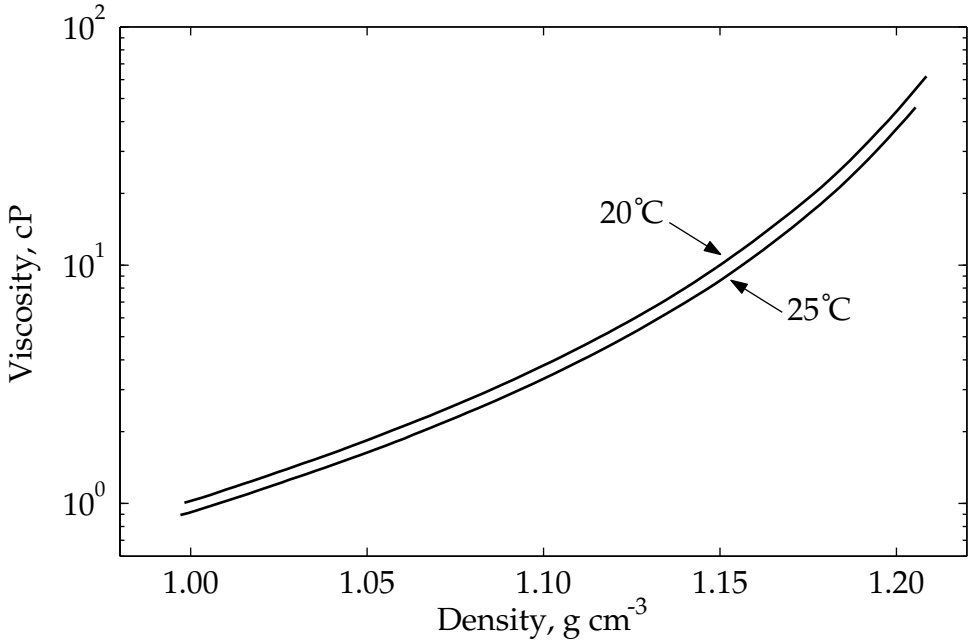

Figure 2.2: Viscosity as a function of density for glycerol–water mixtures between 0% and 80% glycerol by weight.

2.1.1 Surrounding fluid

Aqueous glycerol solutions (0 to 80% wt., 1 to 60×10^{-3} Pa · s) were used as the surrounding fluid for the experiments. Glycerol is completely miscible with water, which allows for a large range of viscosities to be explored by changing the mix proportions. Tabulated values for the density and viscosity of these solutions are readily available (Green and Maloney, 1997; Lide, 2001) and are presented in Appendix C. The specific gravity of the solutions was measured using a hydrometer. The viscosity was then determined from the tabulated data. Figure 2.2 shows the viscosity plotted as a function of mixture density for the lowest and highest temperatures explored in this thesis. Note that the viscosity of glycerol–water mixtures is highly temperature-sensitive; for this reason, the temperature of the liquid was measured at each run with a mercury thermometer. In order to guarantee a stable viscosity, experiments were always run within a 1°C temperature window.

The boiling point of glycerol at atmospheric pressure is 290°C. At 25°C the vapor pressure of glycerol is well below 1 Pa; the vapor pressure of water at that temperature is on the order of 3 kPa. For the concentrations used, water tends to evaporate from the surface of

the solution. As the water evaporates, denser, more viscous glycerol is left behind, making it necessary to regularly stir the mixture. It is important to wait for the air bubbles to clear the liquid after mixing, since they affect the density measurements and interfere with the video imaging.

2.1.2 Pendulum string

Each particle used was suspended from nylon string to form a pendulum. Several strings were used, all of them Dai-Riki Velvet leaders[1] in sizes ranging from 6X (∅ 130 µm) to 9X (∅ 50 µm). The leaders were attached to the spheres using cyanoacrylate contact glue, as described in Appendix A. Depending upon the concentration of glycerol used, a leader is approximately neutrally buoyant. The diameter of the string used for making each pendulum was chosen so that the string diameter was at least 50 times smaller than the sphere diameter. For the experimental conditions explored, the drag coefficient of the string (a cylinder) is similar to that of the sphere. The overall drag force is dominated by the drag on the sphere, since the latter has a larger cross-sectional area. The string's drag contribution amounted to less than 1% of the overall drag force, and was therefore neglected.

In the case of oblique collisions, the torsional stiffness of the string had to be considered. Modeling the string as a linear torsional spring, the torsional oscillation of the pendulum is governed by the equation $I_0\theta'' + K_s\theta = 0$, where I_0 is the polar moment of inertia of the sphere about its center and K_s is the torsional stiffness of the string suspending it. The general solution is $\theta(t) = A\cos\omega_0 t + B\sin\omega_0 t$, where $\omega_0 = \sqrt{K_s/I_0} = 2\pi f$. Therefore,

$$K_s = 4\pi^2 f^2 I_0 = \frac{32}{15}\pi^3 \rho \frac{R^5}{\tau^2}, \tag{2.1}$$

where the polar moment of inertia of a solid sphere, $I_0 = \frac{2}{5}mR^2 = \frac{8}{15}\pi\rho R^5$, has been substituted in. By measuring the period τ of oscillations of a 12.7 mm steel ball bearing ($\rho = 7780\,\mathrm{kg\,m^{-3}}$), the torsional stiffness of the different strings can be calculated from equation (2.1). The results are summarized in Table 2.1.

The contact time for an elastic dry collision, based on equation (1.4), is on the order

[1] Fly-fishing casting lines.

Table 2.1: Torsional stiffness of pendulum strings.

String	$\varnothing\,(\mu\mathrm{m})$	$\tau\,(\mathrm{s})$	$K_s \times 10^9\,(\mathrm{N\,m})$
6X	127	6.648	3846.4
8X	76	17.229	572.8
9X	51	41.568	98.4

of 5 µs for contacts involving steel or glass. For collisions in which plastic deformation occurs, the period becomes longer and can be estimated from equation (1.5). Zenit, Hunt, and Brennen (1997) showed that the duration of an immersed collision is somewhat protracted, presumably because the particle impact speed is reduced by the fluid. The amount of energy that can be recovered in the tangential direction from an oblique contact is related to the lateral stiffness of the bodies in contact, κ_{contact}. The elastic timescales $\tau_{\text{collision}}$ and τ_{string}, corresponding to the lateral stiffness of contact and the torsional stiffness of the string, respectively, are related by the ratio

$$\frac{\tau_{\text{string}}}{\tau_{\text{collision}}} = \frac{\sqrt{\kappa_{\text{contact}}/m}}{\sqrt{K_{\text{string}}/I_0}} \approx \frac{1}{R}\sqrt{\frac{\kappa_{\text{contact}}}{K_{\text{string}}}}, \tag{2.2}$$

where $\kappa_{\text{contact}} = 8aG^*$ is the lateral stiffness of a sphere–plane contact (see Carpick, Ogletree, and Salmeron, 1997; Colchero, Luna, and Baró, 1996). The reduced shear modulus, $G^* = \left[(2-\nu_1)/G_1 + (2-\nu_2)/G_2\right]^{-1}$, depends on G_1 and G_2, the sphere and wall shear moduli, and ν_1 and ν_2, the respective Poisson's ratios.

Based on the times of contact for a typical steel–glass collision and on the measured periods of oscillation in Table 2.1, we have from equation (2.2) that $\kappa_{\text{contact}}/K_{\text{string}} \approx 10^{10}$. The torsional stiffness of the string can therefore be neglected when analyzing oblique collisions with a pendular setup like the one proposed. Furthermore, the stiffness of the string has no effect on the experimental measurement, since each experimental sample spans at most 0.2 seconds, a duration two orders of magnitude shorter than the torsional stiffness timescale.

Table 2.2: Properties of particles used in collision experiments.

Material	d_p (mm)	ε	ρ_p (kg m^{-3})	E (GPa)	ν	σ_s (μm)	λ_p (μm)
Glass beads	3.0	0.0625	2540	60	0.23	0.1384	44.70
	4.1	0.0588	2540	60	0.23	0.0502	41.06
	6.0	0.0476	2540	60	0.23	0.0721	49.76
Glass sphere	6.35–12.7	0.0031	2540	60	0.23	0.1305	22.59
Steel	4.1–12.7	0.0024	7780	190	0.27	0.0236	48.04
Nylon	6.35	0.0031	1140	2.76	0.40	2.0114	41.86
Delrin	12.7	0.0039	1400	2.80	0.35	0.7960	101.49

2.1.3 Particles and target blocks

Five different particle types, with diameters ranging from 3 to 12 mm, were used in the experiments. The particle properties, such as density, ρ_p, Young's modulus, E, Poisson's ratio, ν, diameter, d_p, and sphericity, ε (defined for a given particle as the difference between the largest diameter and the smallest diameter, divided by the nominal diameter), are summarized in Table 2.2. The sphericity values were computed from the particle dimensional tolerances in the manufacturer-provided specifications. The particles included glass grinding beads, glass spheres, steel ball bearings, and nylon and Delrin spheres. Glass grinding beads are inexpensive, and have a significant variation in particle diameter and a lower value of ε. Glass spheres have much tighter size tolerances, a consequence of having been ground into a spherical shape. The table also includes the root-mean-square surface height, σ_s, and the correlation distance, λ_p, measured from the scanning electron microscopy images discussed in §2.1.4.

Most of the experiments presented in this thesis were performed using two different materials as targets: Zerodur[2] (a glass-like material) and Lucite[3]. The properties of the blocks are given in Table 2.3. The blocks were chosen so that their thickness, b, was much larger than the particle diameter (see Goldsmith, 1960; Sondergaard, Chaney, and Brennen, 1990). For comparison, a 6.35 mm glass plate was also used. The surfaces were polished in order to minimize the effect of wall roughness on the experiments. Due to the chamber

[2]Zerodur® is a registered trademark of Schott Glass Technologies.
[3]Lucite® is a registered trademark of Lucite International Ltd.

Table 2.3: Properties of walls used in collision experiments.

Material	$b\,(\mathrm{mm})$	$\rho\,(\mathrm{kg\,m^{-3}})$	$E\,(\mathrm{GPa})$	ν
Glass	6.35	2540	65	0.23
Zerodur	75.0	2530	91	0.24
Lucite	50.8	1100	40	0.32

size of the scanning electron microscope used, it was not possible to measure the surface properties of the Zerodur block. However, the analysis of a small sample from the Lucite block showed that the polished surfaces had a roughness comparable to that of the steel particles.

2.1.4 Surface roughness

The surface roughness is quantified using two parameters as presented in Table 2.2. The root-mean-square surface roughness, or standard deviation of the surface height, σ_s, describes the variation in surface elevation with respect to a flat or mean (reference) surface. In addition to σ_s, the profile of a random surface may be characterized by its autocorrelation function (Thomas, 1999) that describes the similarity between the height, z, of two points of the surface separated some distance, x, along the surface. As the horizontal distance between two surface points increases, the autocorrelation function decreases toward zero since the correlation between the heights of those two surface points decreases. The maximum distance at which a significant correlation occurs is called the correlation length, λ_p, and is defined as the displacement for which the autocorrelation function is equal to e^{-1} (~ 0.36788).

Figure 2.3 shows scanning electron microscopy images of the surfaces of the five kinds of particles used in these experiments and of the Lucite target block. Figures 2.3(a)–(c) show the surface structures of the glass beads. The smaller beads tend to have more pits than the larger ones. In all cases, the asperities are abrupt and have a fairly long correlation distance. In contrast, the ground glass spheres, shown in Figure 2.3(d), have smoother asperities with a short correlation distance. The steel ball bearings are smooth with some isolated scratches along the surface, as shown in Figure 2.3(e). The plastic spheres have both a large r.m.s.

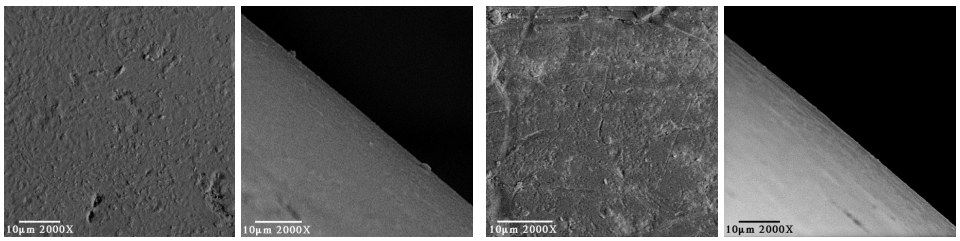

(a) Glass bead, 3.00 mm, ×2000 (b) Glass bead, 4.10 mm, ×2000

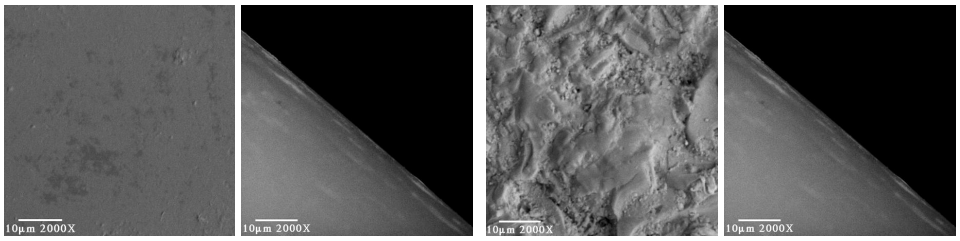

(c) Glass bead, 6.00 mm, ×2000 (d) Glass sphere, 6.35 mm, ×2000

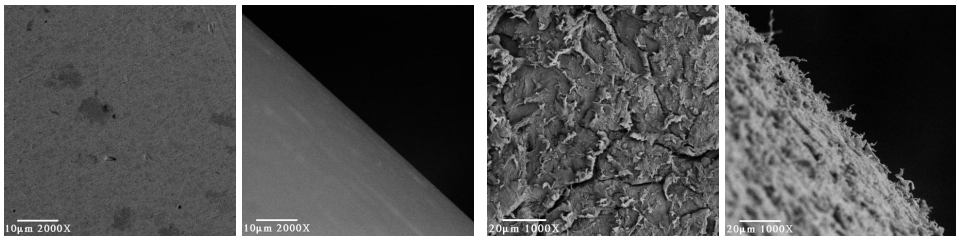

(e) Steel sphere, 6.35 mm, ×2000 (f) Nylon sphere, 6.35 mm, ×1000

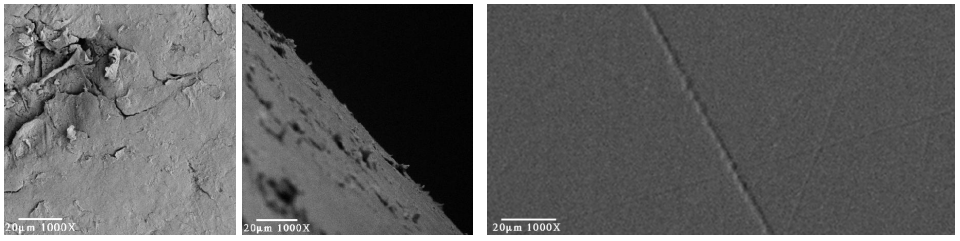

(g) Delrin sphere, 12.70 mm, ×1000 (h) Lucite wall, ×1000

Figure 2.3: SEM photographs of the surfaces of the particles used in the experiments.

roughness and a long correlation distance. The nylon sphere, portrayed in Figure 2.3(f), has an intricate surface with filaments of material towering above the mean surface. The Delrin sphere, shown in Figure 2.3(g), has a surface covered with a regular distribution of small Delrin flakes. It was not possible to obtain a profile image of the target blocks, by virtue of them being flat. However, the analysis of multiple head-on images of small samples from the Lucite block revealed surface roughness characteristics similar to those of the steel particles. Figure 2.3(h) shows the worst scratch encountered on the Lucite samples; most other scratches on the Lucite samples resemble the thinner ones that are barely visible in the figure.

2.2 Experimental technique

The motion of the sphere was filmed using a high-speed digital camera with framing rates up to 2000 frames per second. The typical sampling resolution was 240 pixels wide by 210 pixels high. The resulting digital movie was processed to determine the position of the centroid of the particle in each frame. A description of the tracking algorithm is given in Appendix B. Since the images were taken such that typically 160 pixels appeared across the diameter of the particle, the precision of the position could be determined within 0.3% of a particle diameter, corresponding to a resolution of one-half of a pixel.

Figure 2.4 is an example of the position–time and velocity–time plots recorded at 500 frames per second of a particle approaching the Zerodur wall in water. The data correspond to a 6.35 mm diameter glass particle released from an initial angle of 12° and supported by a line of length 10.5 cm. Two lines are drawn through the five data points before and after impact. For all the data presented in this thesis, line fits were done over five to ten points, depending on the framing rate. In all cases, the correlation coefficient of the line to the data had a value of 0.995 or higher, which is within the resolution of the measurement. The slopes of the fitted lines give the rebound and impact velocities (v_r and v_i), which are used to calculate the coefficient of restitution for a normal impact,

$$e = -\frac{v_r}{v_i}.$$

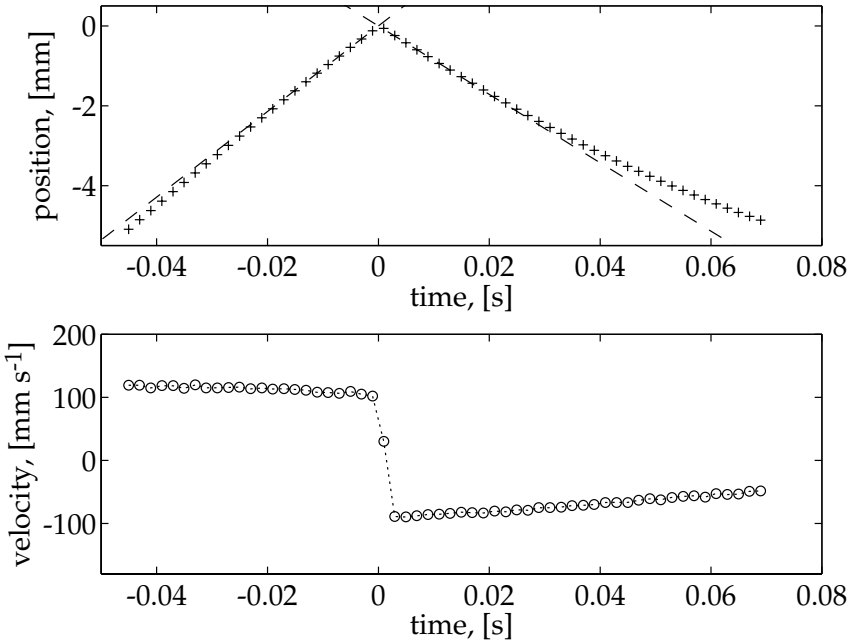

Figure 2.4: Particle position and velocity for a 6.35 mm glass particle released from an angle of 12° impacting the Zerodur wall in water. For this collision, the coefficient of restitution is 0.8 ($Re = 745$, $St = 211$).

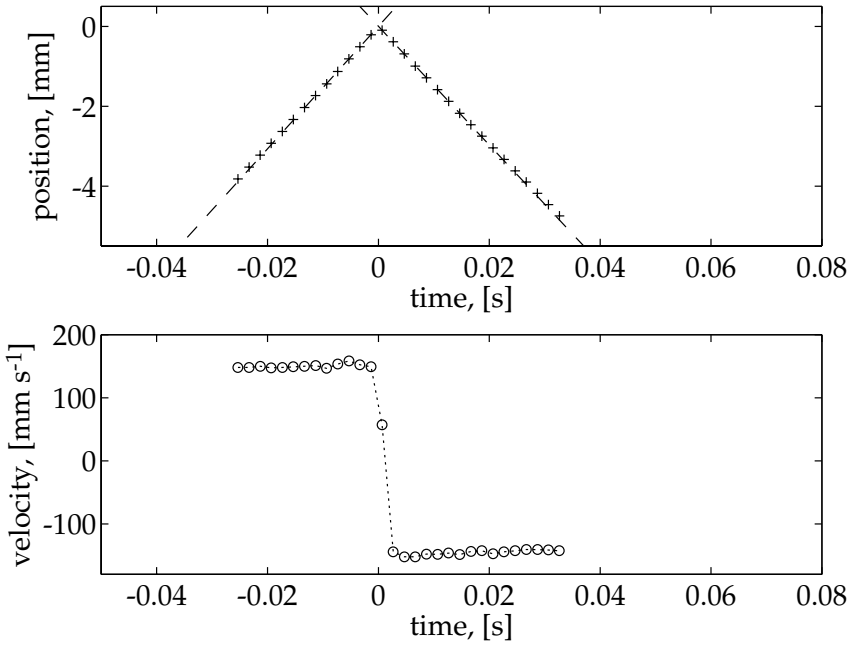

Figure 2.5: Particle position and velocity for a 6.35 mm glass particle released from an angle of 12° impacting the Zerodur wall in air. For this collision, the coefficient of restitution is 0.968 ($Re = 62.5$, $St = 15000$).

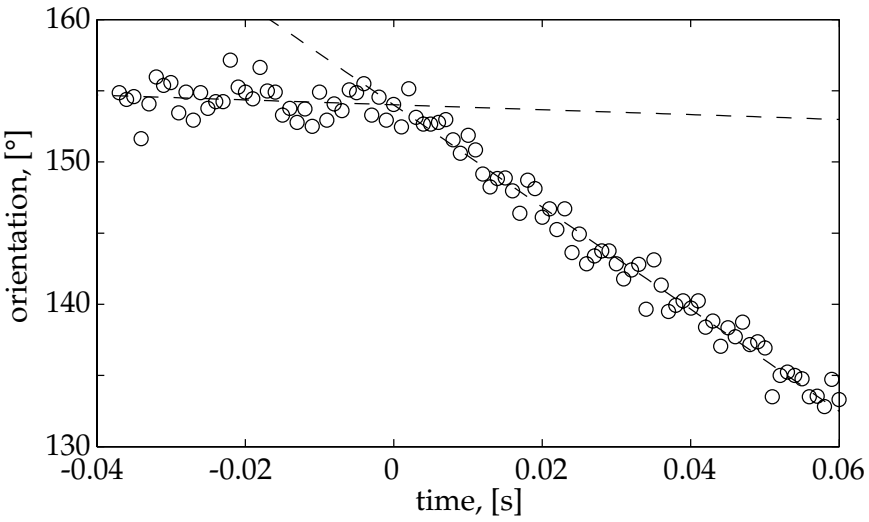

Figure 2.6: Particle position and velocity for a 12.7 mm glass particle in an aqueous solution of glycerol (45% wt.) impacting the Zerodur wall at an angle $\alpha = 20^\circ$. The angular velocities before and after impact are $0.3\,\mathrm{rad\,s^{-1}}$ and $6.26\,\mathrm{rad\,s^{-1}}$, respectively. For this collision, the normal coefficient of restitution is 0.708 ($Re = 374$, $St = 95$).

The origin in the figure represents the point at which the particle reverses its direction of motion and is determined from the intersection of the approach and rebound line fits. The value of the position coordinate represents the gap between the particle and the wall. The velocity of the particle, shown in Figure 2.4, is obtained from the discrete sampled position data using a first-order backward differencing scheme. For comparison, Figure 2.5 shows similar position–time and velocity–time data for the same particle impacting the Zerodur wall in air. When the particle is immersed in a liquid (Figure 2.4), the trajectory shows a slight deceleration due to viscous drag as it approaches the wall, which is not observed in the collision in air (Figure 2.5).

In order to determine the angular velocity of the particles in the oblique collision experiments, two black dots were painted at almost diametrically opposing positions, such that the high-speed camera could see both dots. The positions of these dots were tracked when processing the movie. The angular orientation of the particle was then determined from the slope of a line joining the tracked dots. Figure 2.6 is an example of an angular orientation–time plot obtained from the rotation tracking. The data correspond to a 12.7 mm diameter glass sphere released from an initial angle of 18° supported by a line of length 10 cm. The

plane of the pendulum forms an angle $\alpha = 20^{\circ}$ with the normal of the Zerodur target. Two line fits are done over the entire range of data points before and after impact. The split between the two ranges of data corresponds to the point at which the particle reverses its direction of travel and is determined from the translational velocity plot (similar to Figure 2.4). The slopes of the lines fitted to the angular orientation give the angular velocities before and after impact.

Chapter 3

Normal collisions

The analysis of the impact and rebound of macroscopic particles in a fluid begins with the study of collisions where the trajectory of the impacting particle is perpendicular to the impacted wall. Collisions where the surrounding fluid is air are examined first, in order to validate the applicability of the experimental setup to the measurement of coefficients of restitution. The effect of the surrounding fluid on the collisions is then determined by analyzing experiments performed in aqueous solutions of glycerol. A simple model based on elastohydrodynamic theory is found to predict the effect of the fluid on the coefficient of restitution with moderate accuracy. The effect of surface roughness on the repeatability of the measurements is also discussed.

3.1 Dry coefficients of restitution

To assess the accuracy of the presented experimental setup, and to provide a comparison base for the data, a series of measurements of the dry coefficient of restitution was obtained. In a dry collision, the effect of the surrounding fluid is assumed to be negligible.

For impacts of glass and steel particles against the Zerodur wall within a range of velocities of 40–360 $\mathrm{mm\,s^{-1}}$, the mean coefficient of restitution, $\bar{e}$, is 0.97 ± 0.02, which agrees with the values measured by Foerster *et al.* (1994). For the same particles and velocity range with the Lucite wall, the value is lower, $\bar{e} = 0.92 \pm 0.03$. For the collisions of nylon and Delrin particles, the value is approximately $\bar{e} = 0.90 \pm 0.03$, corresponding to a range of velocities of 50–120 $\mathrm{mm\,s^{-1}}$. The velocities of the glass and steel particle impacts are less

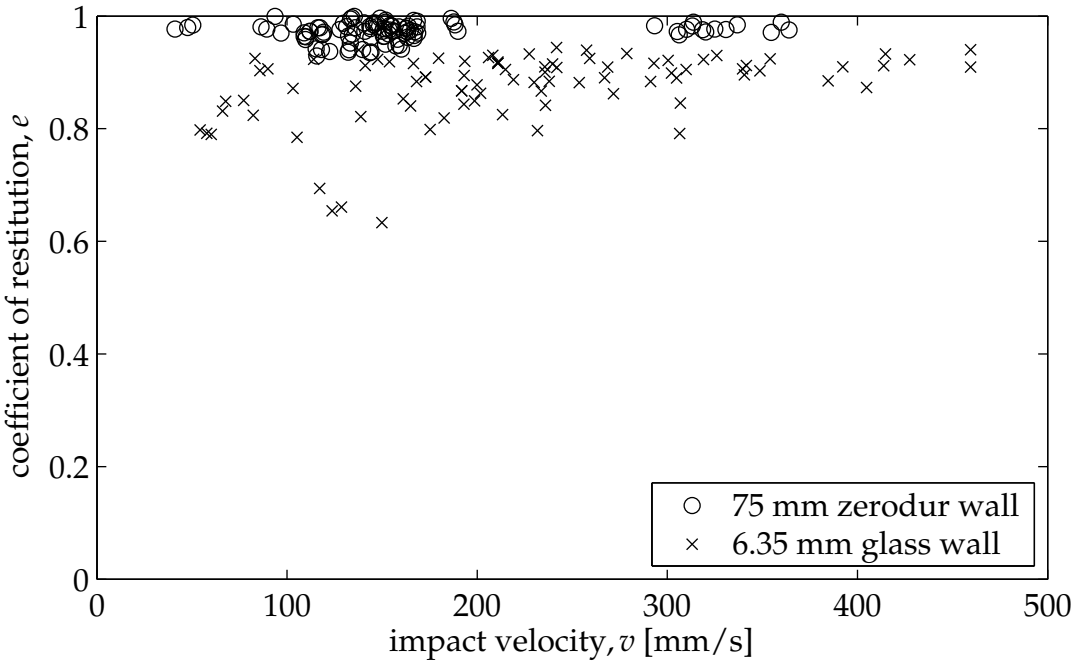

Figure 3.1: Effect of the wall thickness on the dry coefficient of restitution of a 6 mm glass bead. The mean coefficient of restitution is $\bar{e} = 0.977 \pm 0.019$ for the collisions with the 75 mm Zerodur wall and $\bar{e} = 0.877 \pm 0.062$ for the collisions with the 6.35 mm glass wall.

than the velocity corresponding to the fully plastic impact region, for which the coefficient of restitution has been shown to decrease with increasing impact velocity (Goldsmith, 1960; Johnson, 1985).

The measurements made using the thin glass wall resulted in lower coefficients of restitution. An example of these measurements is shown in Figure 3.1, for the cases of a 6 mm glass bead colliding with the Zerodur wall and the thin glass wall. With either a glass or steel impact particle, for the same velocity range, the average value of the coefficient of restitution was lower and the standard deviation was higher ($\bar{e} = 0.88 \pm 0.07$). The lower coefficient of restitution values are in agreement with the measurements obtained by Goldsmith (1960), Sondergaard *et al.* (1990), and Davis *et al.* (2002). In those studies, the reduction of the coefficient of restitution was attributed to the wall thickness. With a thin wall, the elastic waves generated by the particle collision can be reflected back to the impact point during the particle contact time.

3.2 Coefficient of restitution with fluid effects

Figure 3.2 shows the coefficients of restitution measured for the different glass impact particles on the Zerodur wall in water, and glycerol in water mixtures, as a function of the impact Stokes number St. The data indicate that the coefficient of restitution increases with the Stokes number based on the impact velocity. The data show error bars that represent the correlation values of the line fits used to calculate the approach and rebound velocities. One of the data sets is taken with the Zerodur wall inclined 18° with respect to the vertical, such that the particle is still accelerating at impact; the data using the inclined wall are consistent with the other data sets. For the cases where the particle's position did not vary with time after impact, a value of zero is assigned to the coefficient of restitution. Generally, for St less than 80, the scatter of the data is large and outside the error bars. A possible reason for this scatter is discussed in §3.4.

Figure 3.3 shows the measured coefficients of restitution as a function of the impact Stokes number for steel impact particles on the Zerodur wall in several glycerol–water mixtures. The measured coefficients of restitution follow the same trend as in the experiments with the glass particles, but the variance of the results is smaller.

Measurements were also obtained for collisions with the nylon and Delrin particles. The measurements obtained for collisions of these particles on the Zerodur wall in water are shown in Figure 3.4. All measurements obtained for immersed collisions—of glass, steel, and plastic particles—are shown in Figure 3.5, as a function of the collisional Stokes number. Also included are the data for collisions of a 6.35 mm glass sphere in air. The trend is the same for all the materials, regardless of the particle diameter and density, indicating that the Stokes number is the appropriate parameter to represent the results. Within experimental uncertainty, the data show the coefficient of restitution to be independent of the ratio of the solid phase density to the fluid phase density. For example, in the range of Stokes numbers between 100 and 300, the data for the 6.35 mm glass ($\rho_p/\rho_f = 2.5$), for the 12.7 mm Delrin ($\rho_p/\rho_f = 1.4$) and for the 6.35 and 7.93 mm steel ($\rho_p/\rho_f = 7.8$) appear to collapse to the same range of coefficients of restitution. The data also show that the coefficient of restitution is zero for Stokes numbers less than approximately $St_c = 15$.

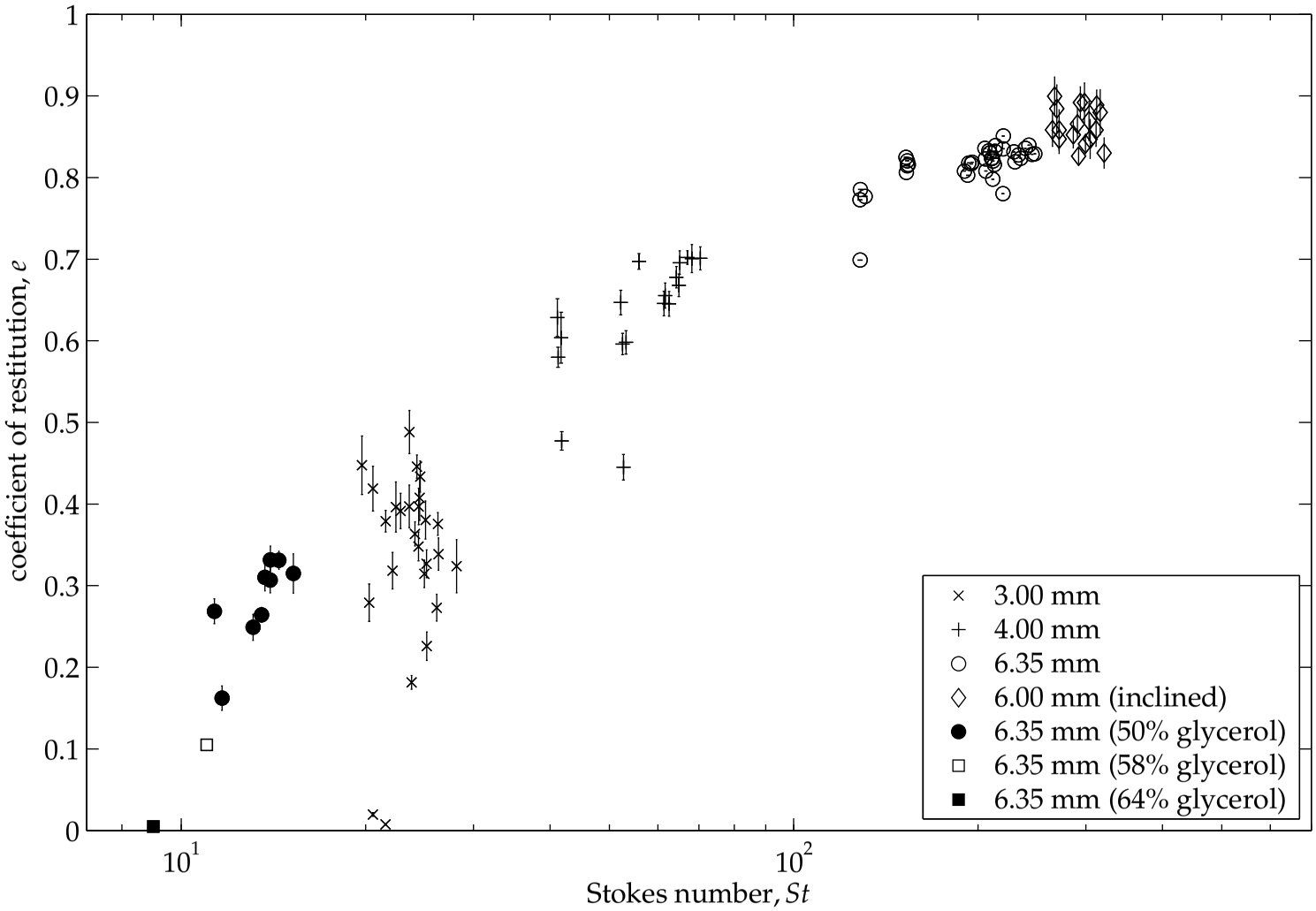

Figure 3.2: Coefficient of restitution, e, as a function of Stokes number based on the impact velocity for collisions of glass particles on the Zerodur wall in water and glycerol–water mixtures.

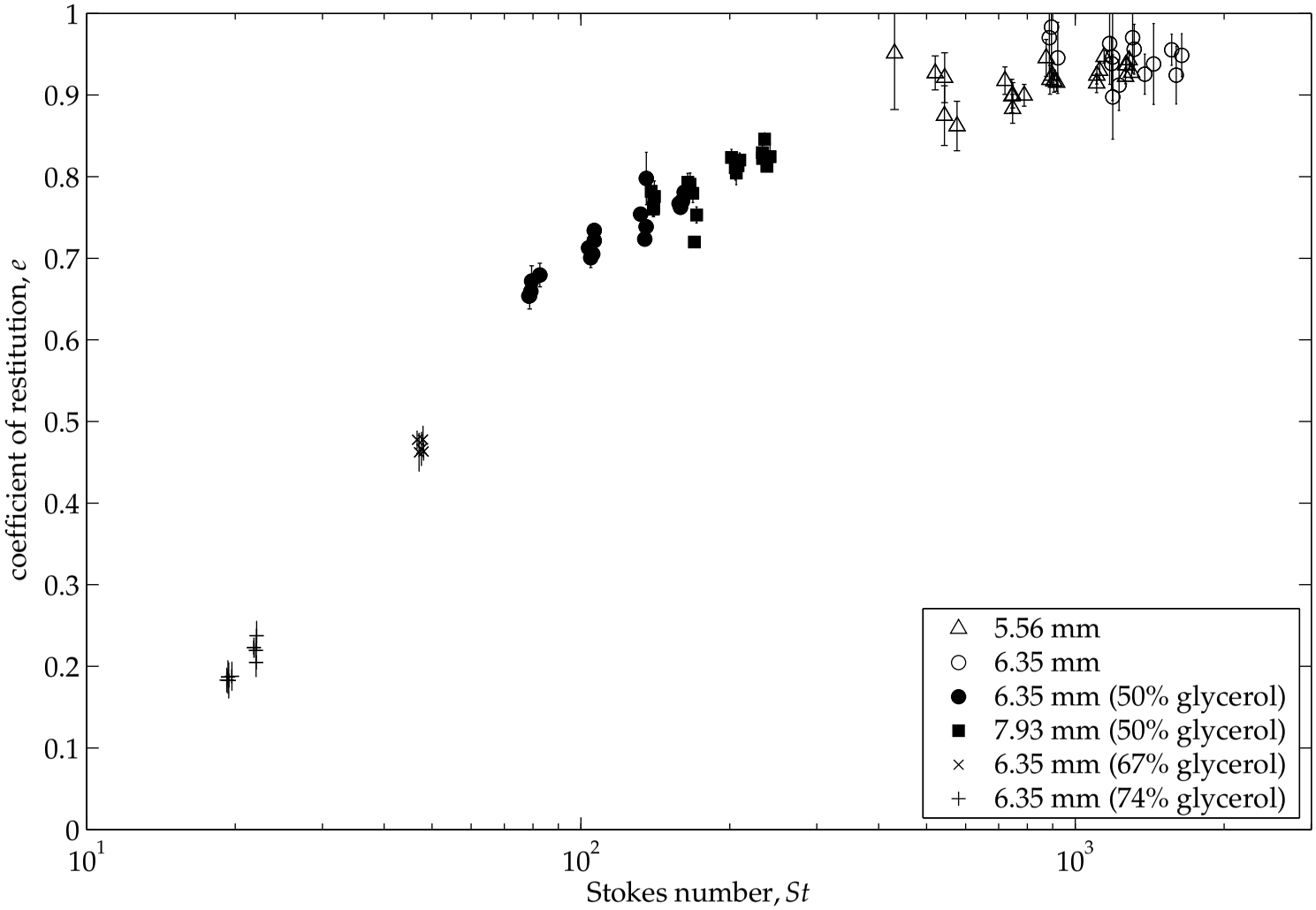

Figure 3.3: Coefficient of restitution, e, as a function of Stokes number based on the impact velocity for collisions of steel particles on the Zerodur wall in water and glycerol–water mixtures.

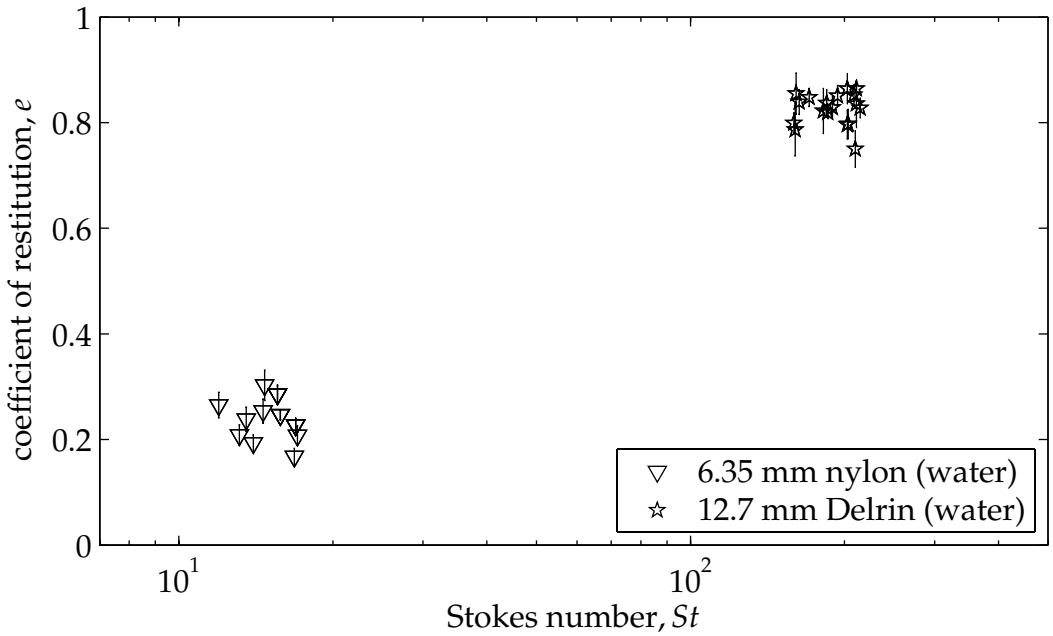

Figure 3.4: Coefficient of restitution, e, as a function of Stokes number based on the impact velocity for collisions of plastic particles on the Zerodur wall in water.

In addition to the data using the Zerodur wall, a Lucite wall was also used; the results are presented in Figure 3.6. Again, the data show that the coefficient of restitution depends on the impact Stokes number, and that the coefficient is zero for Stokes numbers less than a critical value. In comparing the data for Zerodur and Lucite walls, the coefficients of restitution for the Lucite appear to be slightly lower than those for the Zerodur. This difference is also observed in the dry coefficient of restitution. A direct comparison between the data for collisions on Zerodur and on Lucite is presented in §3.3.

Some data were also taken using the thin glass plate. Similar to those found for the dry collisions, the data with the thin plate show a decrease in the average coefficient of restitution and a significant increase in scatter. At Stokes numbers between 100 and 200 the average coefficient of restitution is 0.56, which is approximately 20% less than the value found using the Zerodur wall. In addition, the standard deviation has increased to approximately ± 0.10. The critical Stokes number also appears to be somewhat lower than for the Zerodur wall.

Figure 3.7 shows the immersed collisions of steel particles on the Zerodur wall, and also the measurements by McLaughlin (1968) and Gondret *et al.* (1999, 2002). The data compare

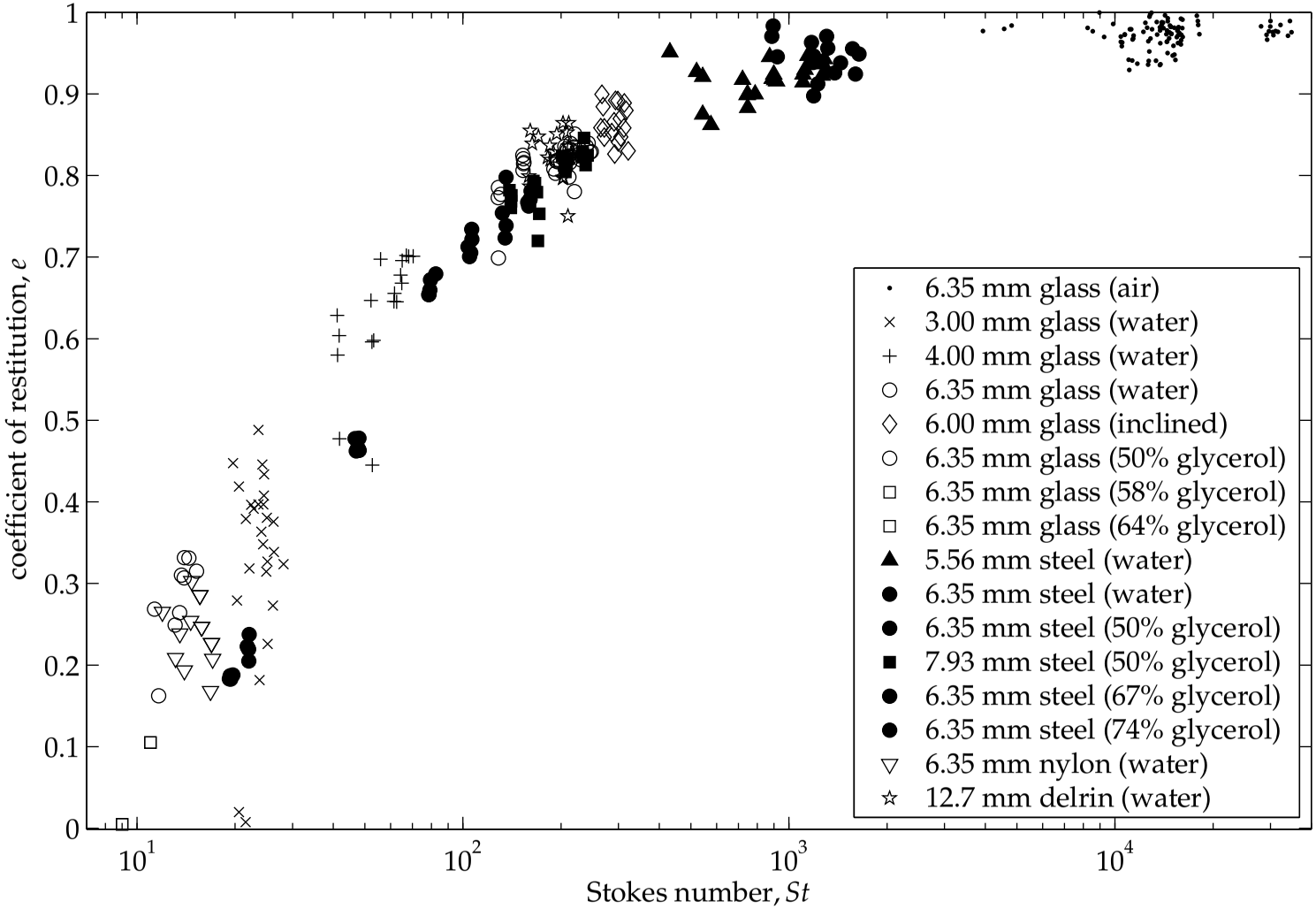

Figure 3.5: Coefficient of restitution, e, as a function of Stokes number based on the impact velocity for collisions of all particles on the Zerodur wall in water.

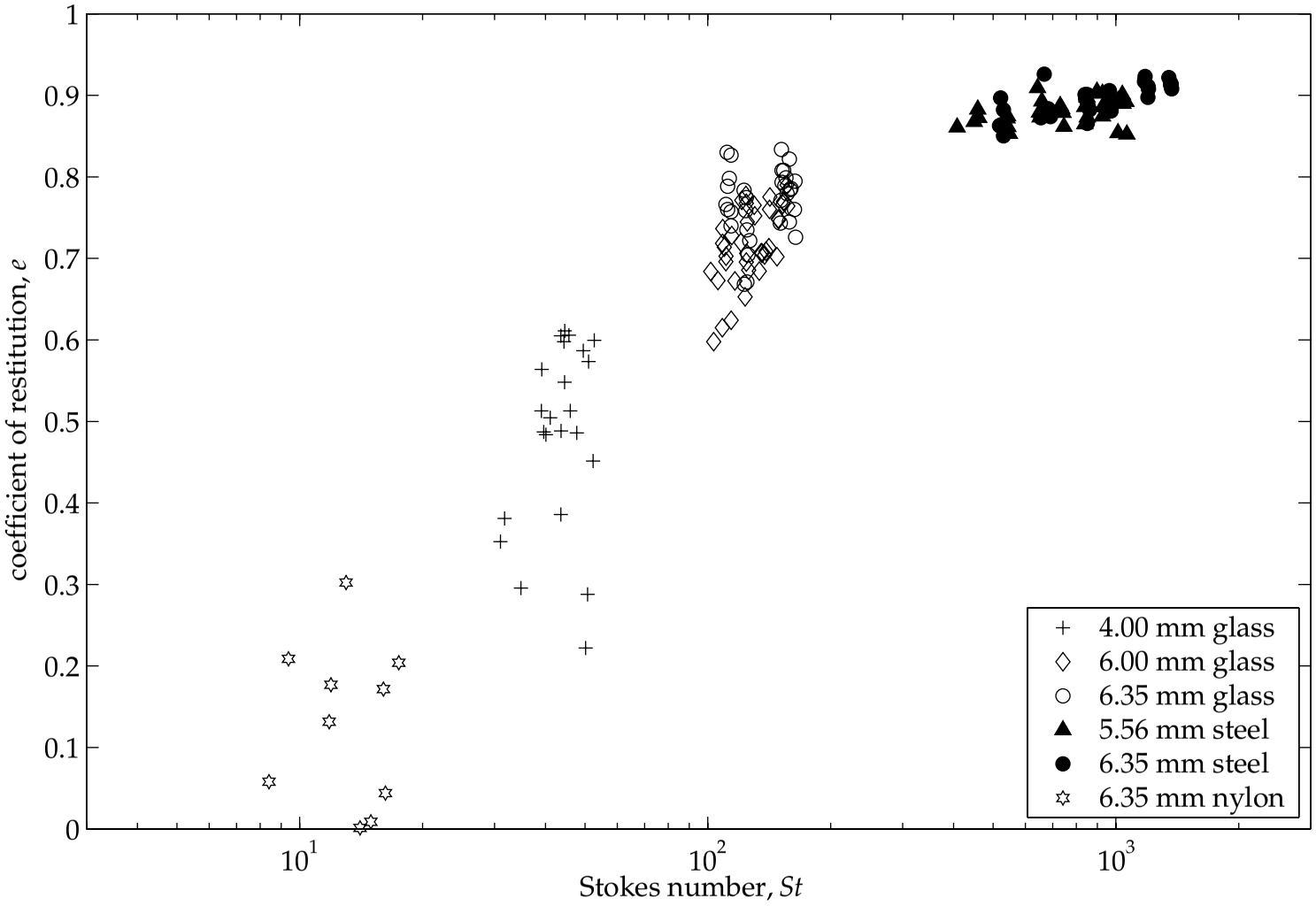

Figure 3.6: Coefficient of restitution, e, as a function of Stokes number based on the impact velocity for collisions of all particles on the Lucite wall in water.

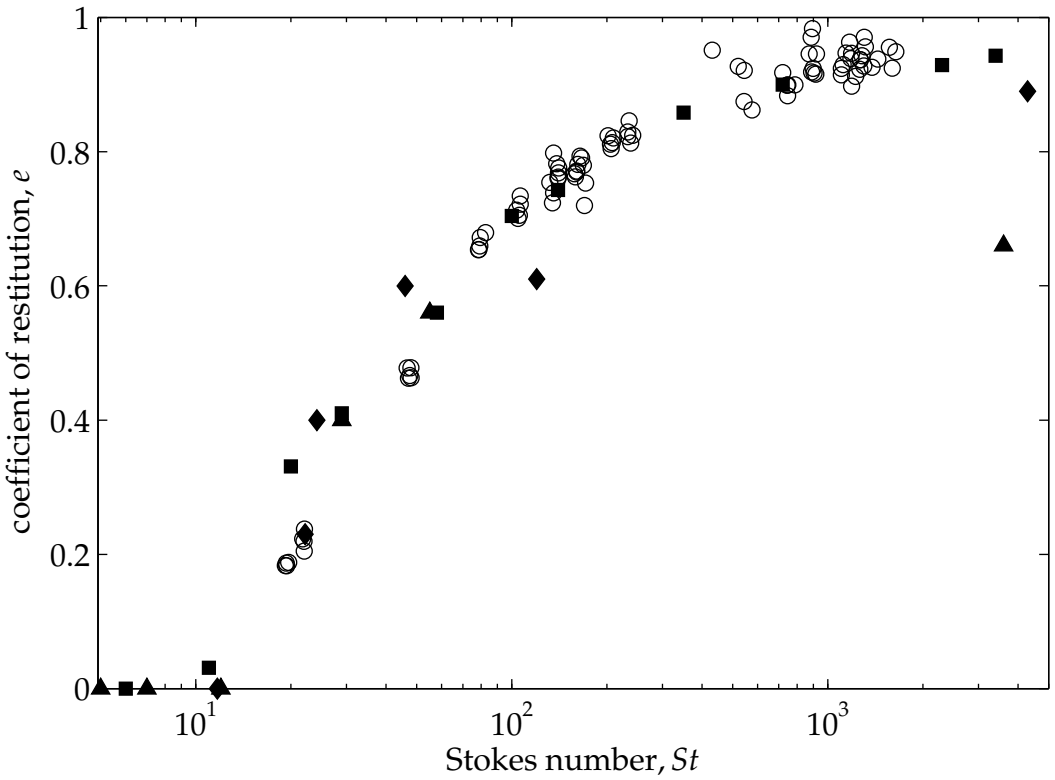

Figure 3.7: Coefficient of restitution, e, as a function of Stokes number for collisions of steel particles on a Zerodur wall (○). Also shown are the results obtained by McLaughlin (1968) (♦), corresponding to steel ball bearings impacting an anvil, and by Gondret *et al.* (1999, 2002) (▲, ■), corresponding to steel spheres impacting a glass wall.

well with the present measurements except for the values at high Stokes number measured by Gondret *et al.* (1999), which may be a result of the thin wall used in their experiments. These measurements seem to have been corrected in the later experiments of Gondret *et al.* (2002).

3.3 Comparison with elastohydrodynamic theories

Since the rebound velocity depends on the elastic properties of the materials, the experiments done with the Zerodur and Lucite walls were compared. The coefficients of restitution for the Lucite were found to be slightly lower than those for the Zerodur. The results for the two walls compare well when presented as a ratio of the immersed and dry coefficients

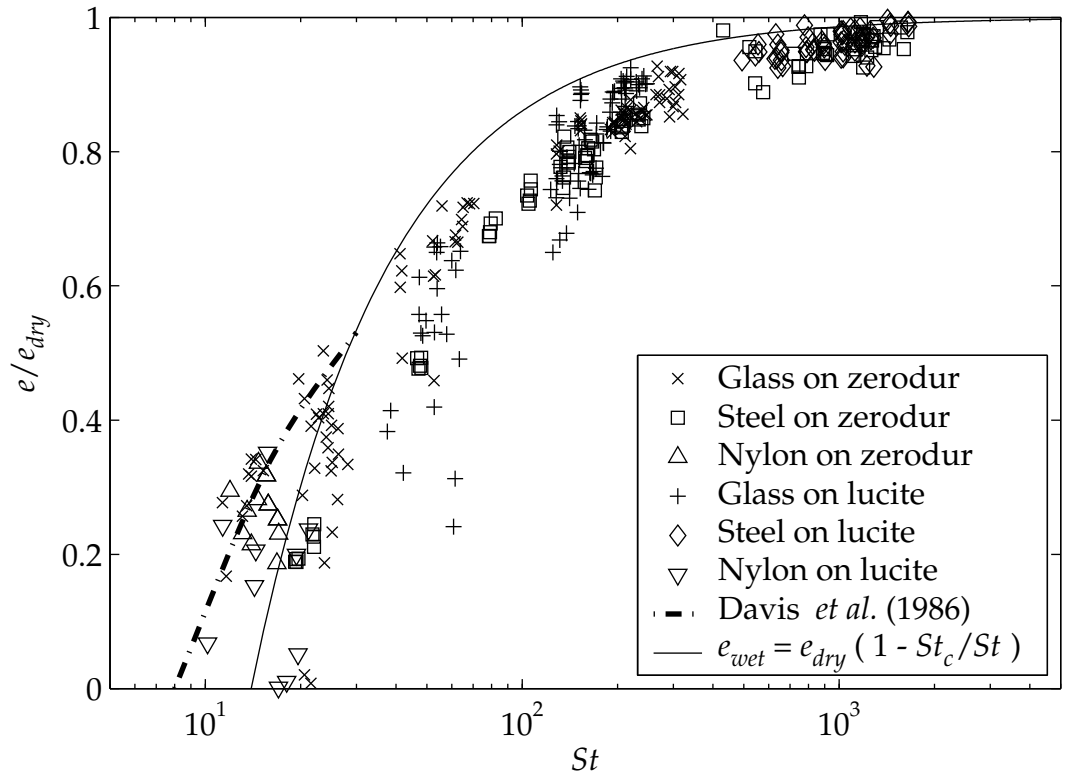

Figure 3.8: Effective coefficient of restitution, e, scaled by the dry coefficient of restitution, e_{dry}, as a function of Stokes number, for immersed particle–wall collisions. The dashed–dotted line shows the coefficient of restitution from the calculations by Davis *et al.* (1986) for a value of the elasticity parameter $\epsilon \approx 10^{-8}$. The solid line shows the coefficient of restitution from equation (3.4) for $e_{dry} = 0.98$ and $x_c/x_0 = 10^{-3}$.

of restitution, as shown in Figure 3.8.

Following the analysis proposed by Davis *et al.* (1986), the viscous component of the coefficient of restitution for an immersed collision can be obtained. Davis *et al.* performed calculations to predict the maximum rebound velocity of elastic particles colliding in a viscous fluid. They characterized the collisions with two parameters, the particle Stokes number and an elasticity parameter, ϵ, defined in §1.2. For the experiments performed in this study, the values of ϵ ranged from 10^{-7} to 10^{-8}. The predictions by Davis *et al.* for $\epsilon = 10^{-8}$ were used, such that comparisons could be made between their calculations and the present measurements. The dashed–dotted line in Figure 3.8 shows this prediction indicating a sharp increase in e as St increases from the critical value. Predictions for $\epsilon = 10^{-7}$ would

result in slightly higher values of e than those for $\epsilon = 10^{-8}$. It is important to note that the Davis *et al.* study predicted that the two surfaces would not come into contact and that the rebound would result from the stored elastic energy. The present comparison suggests that the elastohydrodynamic theory may be extended to slightly inelastic surfaces by normalizing the results with the values for dry collisions.

A different method of obtaining the coefficient of restitution for an immersed collision was proposed by Barnocky and Davis (1988). The model is based on the assumption that the lubrication approximation breaks down at a critical distance, comparable to the size of the particle surface roughness.

From lubrication theory, the hydrodynamic force exerted on a sphere approaching a wall is

$$F_{drag} = 6\pi\mu R u \frac{R}{x} = -m\frac{\mathrm{d}u}{\mathrm{d}t}, \tag{3.1}$$

where x is the gap between the surface of the particle and the wall. To estimate the viscous dissipation produced by a particle colliding with and rebounding from a wall, the equation of motion is integrated in two parts. The first (approach) portion is evaluated from x_0 to the critical distance, x_c, at which the lubrication approximation breaks down due to surface roughness. The second (rebound) portion is evaluated from x_c back to x_0, in order to obtain the total velocity decay.

For the approach, a collision velocity, $u_c = u(x = x_c)$, is obtained,

$$\frac{u_c}{u_0} = 1 + \frac{1}{St_0}\ln\frac{x_c}{x_0}, \tag{3.2}$$

where St_0 is the particle Stokes number at x_0. The velocity after impact is taken as $e_{dry}u_c$, which accounts for the solid–solid contact. Therefore, the rebound velocity of the particle as it returns to x_0 is

$$\frac{u_r}{u_0} = e_{dry}\frac{u_c}{u_0} + \frac{1}{St_0}\ln\frac{x_c}{x_0} = e_{x_0}. \tag{3.3}$$

Note that u_r/u_0 is an effective coefficient of restitution, e_{x_0}, defined at a position x_0, that accounts for losses within the lubrication layer and due to solid–solid contact. This effective

coefficient of restitution is found to be

$$e_{x_0} = e_{dry} + \frac{1 + e_{dry}}{St_0} \ln \frac{x_c}{x_0}, \tag{3.4}$$

where x_c/x_0 can be estimated from the physical variables of the problem. Considering a typical value of surface roughness size on the order of 0.1 μm and assuming $x_0 = R/100$, a typical value of x_c/x_0 is approximately 10^{-3}. The solid line in Figure 3.8 shows the comparison between the prediction from equation (3.4) for $e_{dry} = 0.98$ and $x_c/x_0 = 10^{-3}$ and the experimental measurements. It is important to note that the mechanics of the flow in the gap between the particle and the wall may be significantly affected by the presence of asperities on the surface of the particle. Hence, the dry coefficient of restitution may not capture all the losses associated with the solid–solid contact. In addition, the model assumes that the Stokes drag law is valid for the whole range of experiments. Despite these simplifications, the model compares qualitatively well with the experimental measurements. The rapid change of the coefficient of restitution is captured by the model for small values of Stokes number. According to the model, the critical Stokes number at which rebound first occurs is higher for lower values of the dry coefficient of restitution, which seems to be inconsistent with the experiments. For higher values of the Stokes number, the model underestimates the fluid dissipation occurring during the collision but predicts well the weak dependence of the coefficient of restitution on Stokes number.

3.4 Influence of the particle roughness

A distinctive feature of the measured coefficients of restitution is that the variance increases as the impact Stokes number decreases. During the experiments, special care was taken to ensure that nominal conditions were kept constant for a given experimental set. The variance of the measured coefficient of restitution was observed to be larger than the experimental error for St less than 80 in the experiments done with glass and nylon particles. In the experiments with steel particles, this large variance was not observed. The differences in surface properties among the particle types may account for the observed differences in

Table 3.1: Typical collision parameters for *St* less than 80.

d_p (mm)	v_i (mm s^{-1})	μ (Pa · s)	h_m (μm)	σ_s/h_m	A_h (μm^2)	λ_s (μm^2)	A_h/λ_s
Glass beads							
3.0	25	0.001	0.0063	21.96	859.4	3595.9	0.239
4.1	50	0.001	0.0100	5.02	2794.6	3034.3	0.921
Glass sphere							
6.35	50	0.005	0.0243	5.37	6703.5	918.7	7.297
Steel							
6.35	80	0.024	0.0449	0.53	12310.3	4153.4	2.964
6.35	100	0.014	0.0396	0.60	14716.2	4153.4	3.543
Nylon							
6.35	20	0.001	0.0276	72.88	6324.2	3154.2	2.005

variance.

As a particle approaches the wall, Davis *et al.* (1986) predict a closest distance of approach, h_m, which depends on the elasticity parameter ϵ and the Stokes number. For the collisions presented here, the scaled approach distance h_m/x_1, where $x_1 = (4\mu v_i R^{3/2}/\pi E^*)^{2/5}$, varies from approximately $1/4$ to $1/3$ and is nearly independent of ϵ and *St* for *St* greater than the critical value. Hence, it is possible to use the results of the study by Davis *et al.* to estimate the closest distance of approach for various collision conditions.

Calculated values of $h_m = x_1/3$ are found in Table 3.1 for experimental conditions corresponding to *St* less than 80. These values are compared with the r.m.s. surface roughness, σ_s. As shown in the table, this comparison suggests that h_m is larger than σ_s only for the steel spheres; for the glass sphere and beads, and the nylon particle, σ_s is significantly larger than h_m. Also presented in Table 3.1 is the contact area $A_h = \pi a^2$ calculated from Hertzian contact theory, which predicts that the radius of the contact is given by equation (1.2). This area is compared with an average roughness area $\lambda_s = 1.8\lambda_p^2$. Over a wide range of finite sampling intervals, λ_s is the area in which, on average, one asperity can be found (Johnson, 1985). Hence, the ratio of the Hertzian contact area to the roughness correlation area increases as the number of asperities involved in a contact event increases.

A possible explanation for the variation in the measured coefficients of restitution involves these two ratios. For the steel particles, σ_s is smaller than the calculated distance h_m

and the effective contact area is larger than λ_s. Under these conditions, the variability from collision to collision is expected to be small, which is consistent with the repeatable results for the steel particles shown in Figure 3.5. When h_m is smaller than σ_s and the effective collision area is much larger than λ_s, such as for the glass sphere or the nylon particle, the particle and surface may interact through the tops of the asperities. Although the fluid may still lubricate the surfaces of the asperities, the latter differ in size and orientation, which may contribute to the scatter in the data. In addition, the fluid trapped in the crevices may change pressure as it is compressed. As a result, the rebound velocity may be more variable from experiment to experiment. When h_m is smaller than σ_s and the effective collision area is smaller than λ_s, the roughness may or may not be directly involved in a given collision. Hence, for the small glass beads, the variability in the rebound velocity may result from relatively large asperities being contacted on an irregular basis.

As the particle velocity is increased, both h_m and the Hertzian contact area increase. These effects may contribute to the smaller scatter found at higher Stokes numbers. In addition, the rebound of the particle at low velocities may be affected by other factors. Even when great care is taken to keep the experimental conditions as constant as possible, any asymmetry in the release of the bead may cause a slight spin along the axis of the string of the pendulum. Consequently, the local asperities involved in a particular collision may be different from the ones involved in a subsequent collision, adding to the dispersion of the data.

3.5 Summary

The experimental measurements show the dependency of the coefficient of restitution on the Stokes number. The coefficient of restitution increases with increasing Stokes number beyond a certain critical value of approximately 10. The elastic properties of the particles and the walls do not have a significant impact on the measured coefficients. However, if the wall is not of sufficient size, the coefficient of restitution is reduced and the scatter in the measurements is increased. These results compare well with experimental studies in the literature.

The analysis proposed by Davis *et al.* (1986), which predicts a rapid increase of the coefficient of restitution for low Stokes numbers, compares well with the measurements when presented as a ratio of the immersed and dry coefficients of restitution. Based on this analysis and on the surface properties of the particles, an explanation of the variance of the data was proposed. A simple analytical model based on the one proposed by Barnocky and Davis (1988), and similar to the one proposed by Davis *et al.* (2002), also compares favorably with the experimental data. The characteristic variance observed in the measurements of the immersed coefficients of restitution for St less than 80 appears to be a consequence of the interaction of the surface roughness of the particles and the fluid trapped between them. The observed variance was on the order of the experimental uncertainty for smooth particles and considerably larger for the rougher particles.

Chapter 4

Oblique collisions

Normal collisions between spheres and flat walls were discussed in the previous chapter. While the normal case provides great insight into the physics of immersed collisions, most real-world impacts can be expected not to occur in a trajectory strictly perpendicular to the plane of contact. Oblique collisions of spheres against flat walls are now analyzed.

First, the different theories that describe dry oblique collisions are presented and summarized. Based on these theories and on experimental data from the literature, the applicability of the pendulum setup to the characterization of oblique collisions is verified. Oblique collisions of spheres immersed in liquid are then analyzed. The qualitative and quantitative differences between oblique collisions of smooth and rough spheres are discussed and contrasted. The immersed collisions are also contrasted with the results from dry collisions. Finally, a model that accounts for the fluid effects is presented.

4.1 Oblique impact of spheres

The oblique contact of an elastic sphere and a flat surface can be analyzed based on Hertzian contact theory (Timoshenko and Goodier, 1970), which describes the contact of two spherical objects. The flat surface is represented by letting one of these spheres have an infinitely large mass and radius. An oblique collision can be considered as a superposition of the normal and tangential components of relative motion, with the interaction in the normal direction described by Hertzian theory. Two distinct interaction mechanisms are recognizable in the tangential direction: sliding and rolling. In sliding interactions, the relative

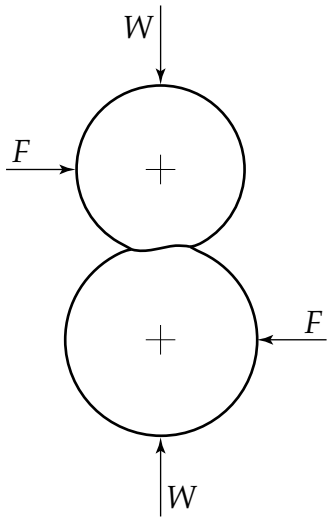

Figure 4.1: Oblique loading of two spheres.

velocity of the contacting surfaces is nonzero. In rolling interactions, the surfaces at the point of contact do not move with respect to each other even if the relative velocity of the centers of mass of the contacting objects is nonzero.

Assume momentarily that tangential interaction between the sphere and the surface is not significantly affected by the elastic deformation of the surfaces in the normal direction. Further assume that the sphere begins to slide in a direction parallel to the wall. If the contact surfaces are not ideally smooth, the sphere experiences an opposing force as a consequence of friction. For a large enough frictional force, the relative velocity of the contacting surfaces drops to zero while the velocity of the center of mass of the sphere is nonzero. From that instant until the end of the collision, the sphere rolls on the flat surface.

In a physical system, the elastic deformation of the contacting surfaces cannot be neglected. Mindlin (1949) studied the case where two homogeneous, isotropic, elastic bodies are pressed together with a constant force W and then subjected to a tangential force F, as shown in Figure 4.1. If $F > \mu_f W$, where μ_f is a constant coefficient of friction, gross sliding occurs throughout the contact area, whereas, for lower values of F, Mindlin concluded that a circular inner region of the contact area remains stuck while a surrounding annulus slides or micro-slips. It should be pointed out that the contact region is not necessarily circular. Cattaneo (1938) derived the equations corresponding to elliptic contact surfaces. These

equations are analogous to the equations for circular contacts and, in general, the circular contact approximation is of satisfactory accuracy.

This approach has the problem of assuming a constant load W throughout. As colliding particles come into contact, deform, and eventually rebound, the load conditions are not that simple. This limitation was addressed by Mindlin and Deresiewicz (1953), who proposed solving cases where the normal and tangential loads vary by applying the following set of rules:

1. The contact radius is given by Hertz contact theory.
2. Slip is initiated whenever, in the absence of slip, F at any point exceeds the product $\mu_f W$ at that point.
3. Slip progresses concentrically, forming an "annulus of slip."
4. The inequality $F \leq \mu_f W$ holds throughout the contact area.
5. The adhered portion of the contact surface is subjected to a change of tangential traction and undergoes a rigid-body tangential displacement.
6. The evolution between two equilibrium states can be described by a quasi-static process.

The approach described by Mindlin and Deresiewicz is applicable to a wide variety of collisions. Their result is valid for the case when the spheres are first compressed normally and then sheared. Walton (1978) studied the case where the two motions occur simultaneously. Under those conditions, Walton concluded that if slip occurs, then it will be in the form of sliding, *i.e.*, slip over the whole of the contact area. Elata (1996) warns against misusing the force–displacement relations obtained by Walton by regarding them as path-independent. These relations are path-dependent, and are derived assuming a fixed ratio between the normal and tangential displacements of contact. When used to describe certain cyclic contact displacements, Walton's relations predict a net energy generation without any work being done, which violates the second law of thermodynamics.

Since the loading history depends on both the compliance of the contact and the motion of the particles, the problem is well suited to a numerical solution that steps forward in time. Maw, Barber, and Fawcett (1976) developed such a method. The analysis presented below closely follows the procedure detailed by Maw *et al.* The contact region is divided by a series of n equi-spaced concentric circles of radius ai/n $(i = 1, \ldots, n)$, which define the limits of a series of tangential traction distributions such that the total traction f at radius r is

$$f(r) = \sum_{i=j}^{n} f_i \left(1 - \frac{n^2 r^2}{a^2 i^2}\right)^{1/2}, \tag{4.1}$$

where j is the smallest integer greater than nr/a. The n coefficients f_i can be obtained by solving a mixed boundary-value problem in elasticity. A provisional division into slip and stick regions can be assumed. In slip regions, the tangential traction is $f(r) = \pm\mu_f p(r)$, where $p(r)$ is the local normal contact pressure. In stick regions, the tangential displacement is prescribed. The mixed boundary-value problem in elasticity can now be solved and the solution tested to see whether the original assumption was correct. In slip regions, the relative incremental displacement must be in the correct sense for the assumed frictional traction. In stick regions, the tangential traction must be below the frictional limit. The assumption is changed for any failed region and a new solution is obtained. Convergence is rapid. The following is an outline of the solution proposed by Maw *et al.* (1976) for a sphere impacting a half-space.

1. Using the Hertz theory, find the solution to the normal contact problem.

2. By proposing a distribution of tractions of the form

$$f(r) = \begin{cases} \left(1 - r^2/a^2\right), & 0 \le r \le a, \\ 0, & r > a, \end{cases} \tag{4.2}$$

   and following the method used by Mindlin (1949), find the relative tangential displacements u_T in the direction of the traction.

3. Stepping forward in time, find the new displacements and loads by assuming a provi-

sional division into stick and slip regions.

4. Test the obtained solution to ensure consistent tangential tractions, *i.e.*, verify that the tangential traction does not exceed the friction limit in stick regions and that the assumed slip direction is adequate in slip regions.

5. Once a satisfactory solution has been obtained, find the change in velocity during the present time step from momentum considerations. The tangential force, found by integrating equation (4.1) over the contact area,

$$F = \frac{2\pi a^2}{3} \sum_{i=1}^{n} i^2 \frac{f_i}{n^2}, \tag{4.3}$$

produces a change in angular and linear velocity,

$$\delta v_T = -\frac{F\delta t}{M} - \frac{FR^2\delta t}{I} = -\frac{F\delta t}{M}\left(1 + \frac{1}{K^2}\right), \tag{4.4}$$

where $K = \left(I/MR^2\right)^{1/2}$ is a nondimensional radius of gyration and $v_T = v + \omega R$ is the instantaneous value of the tangential velocity at the point of contact.

6. With the new tangential velocity, find the corresponding tangential displacements u_T and repeat the procedure for the next time increment.

In order to achieve more generality, Maw *et al.* (1976) proposed two nondimensional parameters, applicable to all materials and experimental conditions. The first, χ, is a modified radius of gyration and is defined by

$$\chi = \frac{(1-\nu)\left(1 + 1/K^2\right)}{2-\nu}. \tag{4.5}$$

The second parameter, ψ, is a nondimensional local angle of contact, and is defined by

$$\psi(v_T) = \frac{2(1-\nu)v_T}{\mu_f (2-\nu) v_{N,in}}. \tag{4.6}$$

Nondimensional angles of incidence and reflection, ψ_{in} and ψ_{out}, can be determined for

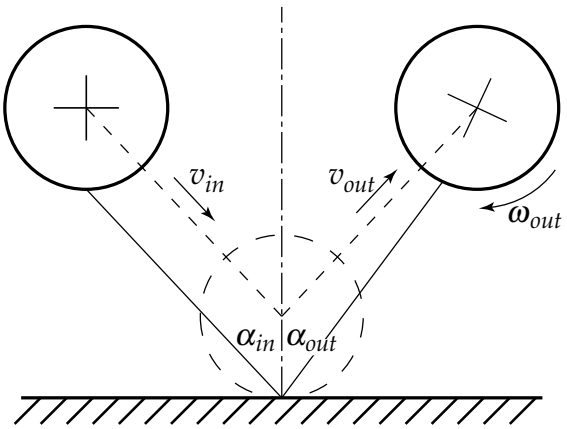

Figure 4.2: Schematic representation of the oblique collision of a sphere with a flat surface. The sphere approaches the wall with no spin.

corresponding $v_{T,in}$ and $v_{T,out}$. A positive angle of reflection is one in which the tangential velocity of the point of contact retains the same sense. The parameter ψ can be interpreted physically with respect to the parameter χ as follows. For values of $\psi \leq 1$, which correspond to small angles of incidence, the normal load is considerably larger than the tangential force of the particle and the surfaces stick during contact, although some microslip may be observed in the periphery of the contact area where the normal load is markedly lower. For values of ψ between 1 and $(4\chi - 1)$, corresponding to intermediate ranges of the incidence angle, the collision starts in gross slip. In this range the traction produced by friction is large enough that the sliding velocity drops to zero before the end of the collision, and the process transitions instantaneously from gross slip to full stick. Collisions at larger angles, where $\psi \geq (4\chi - 1)$, occur entirely in gross slip.

A drawback of this otherwise general approach is that, in order to evaluate ψ from experimental measurements, a prior quantitative evaluation of the coefficient of sliding friction is required. At the beginning of a collision, the only independent input variable for a given system is the effective angle of incidence, with the material properties captured by χ and μ_f. The local angles of incidence, α_{in}, and rebound, α_{out}, at the contact area, shown in Figure

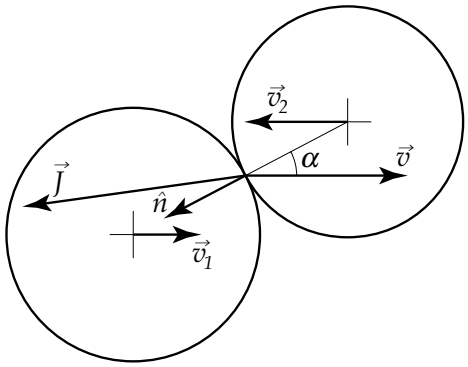

Figure 4.3: Two spheres in an oblique collision.

4.2, are given by

$$\tan\alpha_{in} = \frac{v_{T,in}}{v_{N,in}} = \frac{\mu_f(2-\nu)}{2(1-\nu)}\psi_{in} \equiv \Psi_{in} \qquad \text{and} \tag{4.7a}$$

$$\tan\alpha_{out} = \frac{v_{T,out}}{v_{N,in}} = \frac{\mu_f(2-\nu)}{2(1-\nu)}\psi_{out} \equiv \Psi_{out}. \tag{4.7b}$$

Instead of evaluating a continuously varying force–displacement relationship for the collision of elastic particles, it is often preferable to specify an instantaneous collision operator for the equivalent system of rigid particles. Walton (1993) presents a reasonably accurate description of collisions between macroscopic spheres by introducing a three-parameter model:

1. a normal coefficient of restitution, e;
2. a rotational coefficient of restitution, β, for contacts that are not continuously sliding during the entire collision; and
3. a coefficient of sliding friction, μ_f, for sliding or grazing collisions.

The rotational coefficient of restitution is the same as the roughness coefficient β introduced by Lun and Savage (1987). Unlike the description by Maw *et al.* (1976), Walton's model implies that slipping and sticking regions do not coexist in a given impact.

For two colliding spheres of radii R_1 and R_2 and masses M_1 and M_2 (Figure 4.3), the

velocities before and after collision are related by the impulse exerted by one sphere on the other,

$$\vec{J} = M_1 \left(\vec{v}_{1out} - \vec{v}_{1in}\right) = -M_2 \left(\vec{v}_{2out} - \vec{v}_{2in}\right). \tag{4.8}$$

The relative velocity $\vec{v}$ of the point of contact is given by

$$\vec{v} = \left(\vec{v}_1 - \vec{v}_2\right) - \left(R_1\omega_1 + R_2\omega_2\right) \times \hat{n}, \tag{4.9}$$

where $\hat{n}$ is the unit vector that joins the centers of the two spheres.

The normal coefficient of restitution is given by

$$e = -\frac{\hat{n} \cdot \vec{v}_{out}}{\hat{n} \cdot \vec{v}_{in}}, \tag{4.10}$$

where $0 \leq e \leq 1$, and changes in the angular velocities of the spheres are given by

$$\frac{I_1}{R_1}\left(\omega_{1out} - \omega_{1in}\right) = \frac{I_2}{R_2}\left(\omega_{2out} - \omega_{2in}\right) = -\hat{n} \times \vec{J}. \tag{4.11}$$

For sliding collisions, the coefficient of sliding friction dictates the relation

$$\left|\hat{n} \times \vec{J}\right| = \mu_f \left(\hat{n} \cdot \vec{J}\right), \tag{4.12}$$

where $\mu_f \geq 0$, between the normal and tangential components of the impulse. Combining equations (4.8)–(4.12) we obtain

$$\vec{J}_{sliding} = -M^* \left(1 + e\right) \left[\hat{n}\left(\vec{v} \cdot \hat{n}\right) - \mu_f \frac{\vec{v} \cdot \hat{n}}{\left|\vec{v} \times \hat{n}\right|}\left(\vec{v} - \hat{n}\left(\vec{v} \cdot \hat{n}\right)\right)\right], \tag{4.13}$$

where $M^* = \left(M_1^{-1} + M_2^{-1}\right)^{-1}$ is the reduced mass. Note from the definition of Ψ_{in} in equation (4.7a) that $-\vec{v} \cdot \hat{n} / \left|\vec{v} \times \hat{n}\right| = 1/\Psi_{in}$.

Application of this method leads to a sliding solution of the form

$$\Psi_{out} = \Psi_{in} - \mu_f \left(1 + e\right)\left(1 + 1/K^2\right). \tag{4.14}$$

For non-sliding collisions, the obtained solution is

$$\Psi_{out} = -\beta\Psi_{in}. \tag{4.15}$$

The effective angles of incidence and rebound, Ψ_{in} and Ψ_{out}, are those defined in equation (4.7). Since in Walton's model μ_f and β are mutually exclusive properties of the contact point, it is not possible to extract either of their values from an individual collision without knowing beforehand whether or not the collision involves gross sliding. This limitation can be circumvented by plotting Ψ_{out} as a function of Ψ_{in}. From such a plot, the slope of equation (4.15) and the intercept of equation (4.14) can be used to determine β and μ_f, respectively (Maw, Barber, and Fawcett, 1981; Foerster *et al.*, 1994),

$$\beta = -\frac{\Psi_{out}}{\Psi_{in}} \tag{4.16}$$

and

$$\mu_f = \frac{\Psi_{in} - \Psi_{out}}{(1+e)\,(1+1/K^2)}. \tag{4.17}$$

Equation (4.16) can be considered valid for the entire range of collisions, from sliding to sticking (or rolling). In that sense, a value of $\beta = -1$ indicates full, non-dissipative sliding, since it results from identical $v_{T,in}$ and $v_{T,out}$. The case when $\beta = 0$ corresponds to a rolling contact, where $v_{T,out} = 0$. A value of $\beta = 1$ suggests a collision with full recoil, where $v_{T,out} = -v_{T,in}$. Non-zero values between these extrema indicate dissipation during the collision, either frictional losses for sliding collisions or inelasticity in the contact for collisions with recoil.

A plot of equation (4.17) for the entire range of collisions has two distinct regions. The first one, where the calculated μ_f steadily grows towards a plateau, corresponds to non-sliding collisions. The second one is the plateau itself, where a fairly constant value of μ_f indicates sliding collisions. By considering β valid for the entire range of collision angles α, equations (4.16) and (4.17) can be rewritten as

$$\mu_f = \frac{2\,(1+\beta)}{7\,(1+e)}\Psi_{in}, \tag{4.18}$$

where the square of the nondimensional radius of gyration of a homogeneous sphere, $K^2 = I/MR^2 = 5/2$, has been substituted in. The coefficients of restitution e and β and the incidence angle Ψ_{in}, from which μ_f can be calculated, are all measurable quantities.

4.2 Dry collisions

In order to validate the applicability of the pendulum setup to the measurement of oblique collisions, a series of experiments was performed with a 12.7 mm steel ball bearing impacting a Zerodur block. The azimuthal orientation of the wall was adjusted such that its normal formed an angle α_{in} with respect to the plane of the pendulum. The spheres were released from an angle $\phi_i = 15^\circ$ with respect to the vertical (see Figure 2.1). The specifics of the particle tracking algorithm used are described in Appendix B.

The measurements made using the pendulum setup in air compare favorably with the experiments of Maw *et al.* (1981), where pucks on an air table were made to collide with a polished steel block of matching specification. The pucks used by Maw *et al.* were sliced by spark erosion from commercial steel ball bearings. Figure 4.4 shows the comparison between the collision of a 101.6 mm diameter steel puck impacting a steel wall and a 12.7 mm steel sphere impacting a Zerodur wall. The mean normal coefficient of restitution of the latter was $\bar{e} = 0.97 \pm 0.02$, which agrees with the values measured in §3.1.

From the linear fits to the Ψ_{out} vs. Ψ_{in} plot shown in Figure 4.4, the values of the rotational coefficient of restitution ($\beta = 0.34 \pm 0.07$) and the coefficient of sliding friction ($\mu_f = 0.11 \pm 0.003$) were calculated from equations (4.16) and (4.18). These values are consistent with those measured by Maw *et al.* (1981) and Foerster *et al.* (1994).

4.3 Collisions in a liquid

Measurements were obtained for collisions of glass and steel spheres on the Zerodur wall in glycerol–water mixtures. Figure 4.5 shows the normal coefficient of restitution e obtained from these measurements. Also included are the data for normal collisions (from Figures 3.2 and 3.3). The data are plotted as a function of a modified Stokes number,

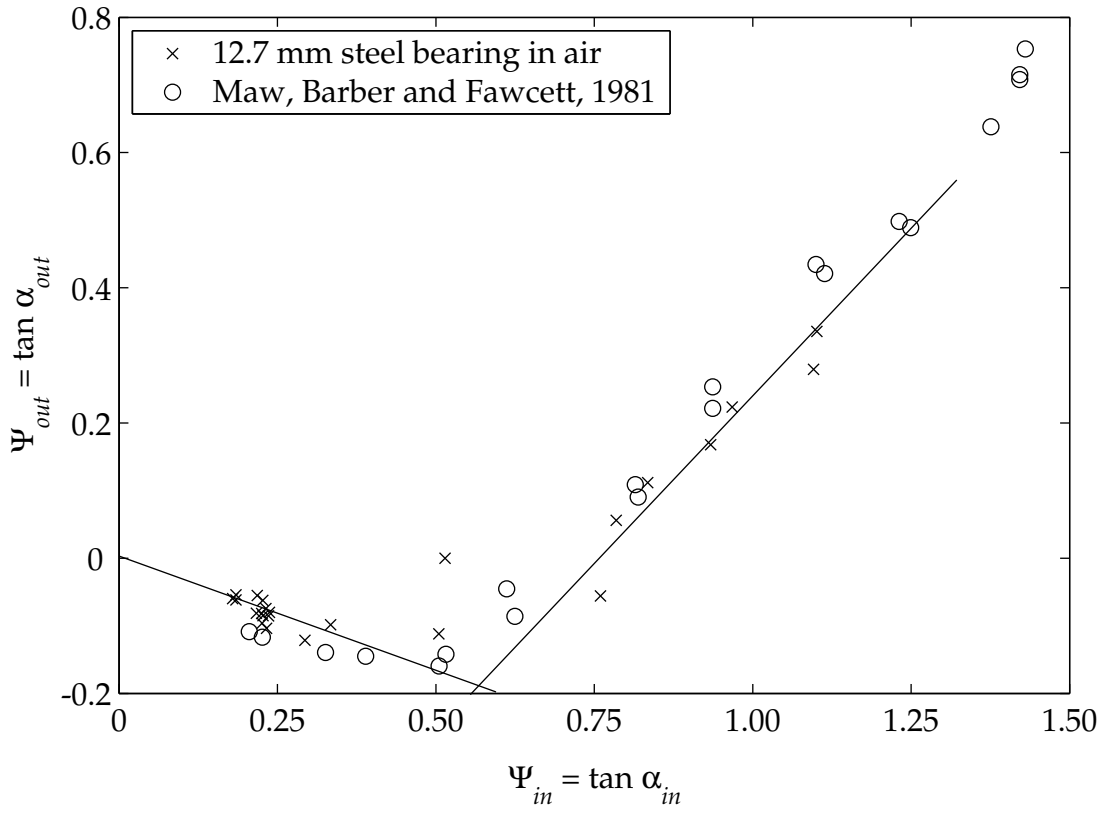

Figure 4.4: Comparison between the experimental results of Maw *et al.* (1981) and the oblique collision of a 12.7 mm steel sphere in air on a Zerodur wall.

$St\cos\alpha_{in} = 2\rho_p R v_{N,in}/9\mu$, based on the normal component of the impact velocity. The incident angle α_{in} is the angle formed by the trajectory of the contact point and the wall's normal. The trend is the same for all cases, regardless of the incident angle. Within experimental uncertainty, the data show the normal coefficient of restitution in oblique collisions to be independent of the tangential component of velocity. Hence, the results from §3.3 may be used directly in equation (4.18) when characterizing oblique immersed collisions.

Figure 4.6 shows the measured change in angular velocity after impact for a 12.7 mm steel ball bearing colliding with a Zerodur wall as a function of impact angle. The system is immersed in water ($T = 20$°C, $\mu = 1\times10^{-3}$ Pa · s). The data show error bars that represent the correlation values of the line fits used to calculate the angular velocities, as shown in Figure 2.6.

For values of α_{in} between zero and ten degrees, the angular velocity steadily increases as the tangential impact velocity increases. Beyond $\alpha_{in} = 10^\circ$ an angular velocity plateau

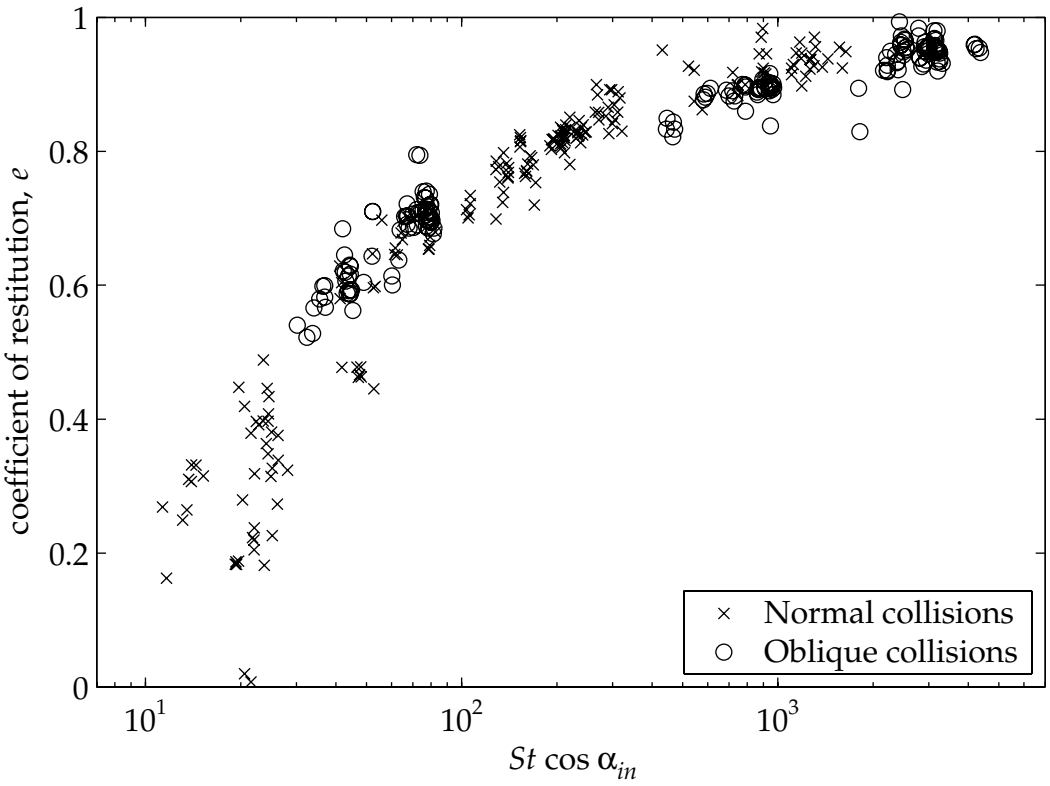

Figure 4.5: Effective normal coefficient of restitution, e, as a function of a modified Stokes number based on the normal velocity of impact, $St\cos\alpha_{in}$, for immersed oblique collisions in water and glycerol–water mixtures.

of roughly $\omega_{out} = 3\,\mathrm{rad\,s^{-1}}$ is reached. This suggests that for near-normal collisions there is little or no gross sliding of the particle, whereas gross sliding occurs promptly afterward. Figure 4.7 illustrates such behavior on the corresponding Ψ_{out} vs. Ψ_{in} plot. Compared with the data for dry collisions, there is little incursion of the data into negative values of Ψ_{out}, which indicates an absence of recoil in the collisions. The dotted line, of slope one, is the theoretical trajectory of a specular rebound with no rotation, and is provided for comparison purposes. The experimental data for $\Psi_{in} > 0.25$ clearly follow a slope one line with a negative intercept on the Ψ_{out} axis.

A plot of the derived rotational coefficient of restitution, based on equation (4.16), is presented in Figure 4.8. Each data point indicates the average value of the five distinct experimental runs performed for each angle α_{in}. Each error bar represents the standard deviation of the five averaged measurements. The rotational coefficient of restitution for near-normal

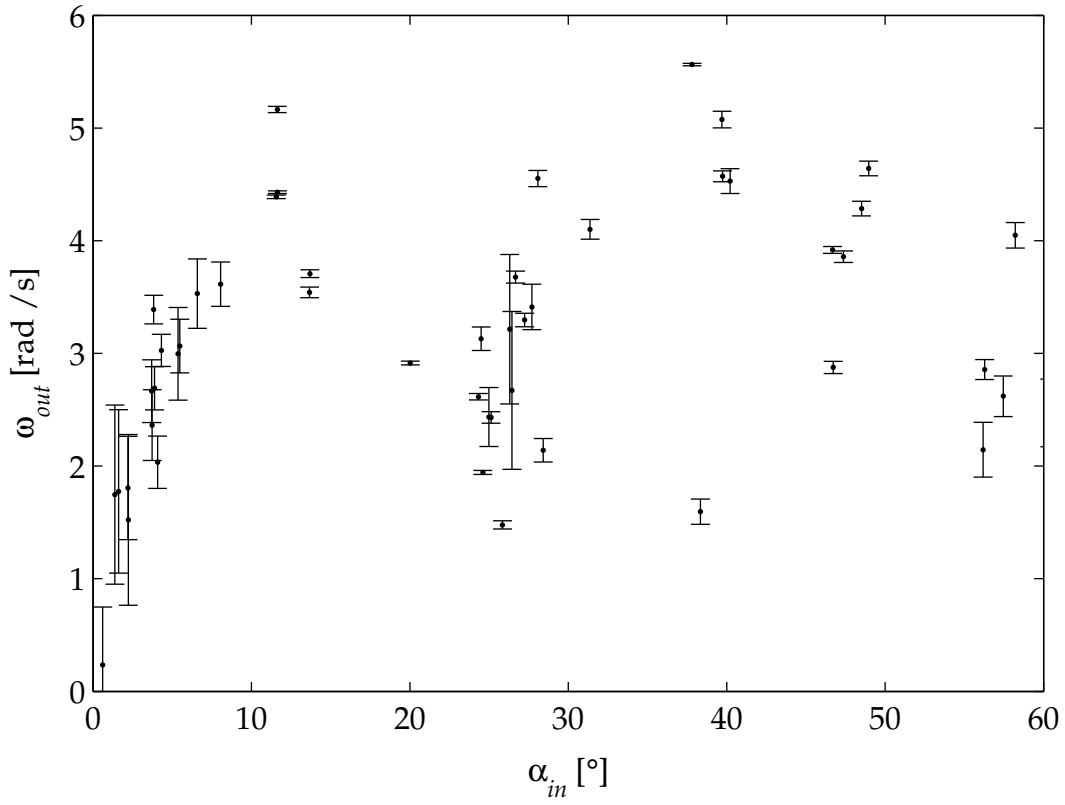

Figure 4.6: Measured angular velocity for a 12.7 mm steel ball bearing impacting obliquely without spin on a Zerodur wall. The surrounding fluid is water ($St = 2750$, $Re = 3170$).

collisions is $\beta = 0.46 \pm 0.16$, larger than what would be expected from the measurements by Foerster *et al.* (1994). However, the error associated with the individual measurements grows considerably as the tangential impact velocity decreases. Figure 4.8 also shows the coefficient of sliding friction, based on equation (4.17). The computed coefficient of friction for the sliding collisions, $\mu_f \approx 0.03$, is about one order of magnitude smaller than the coefficient of friction for a lubricated contact between steel and glass (Bowden and Tabor, 1950). A possible explanation of this frictional value is discussed in §4.4.

Figure 4.9 shows the measured after-impact angular velocities for a 12.7 mm glass sphere colliding with a Zerodur wall. The surrounding fluid is a 4.5×10^{-3} Pa · s aqueous solution of glycerol (45% wt.). The behavior is markedly different from that observed with steel collisions (Figure 4.6). While the angular velocity does reach a plateau of almost 9 rad s^{-1}, it only does so at fairly large collision angles (in excess of 30°). The richer behavior of these

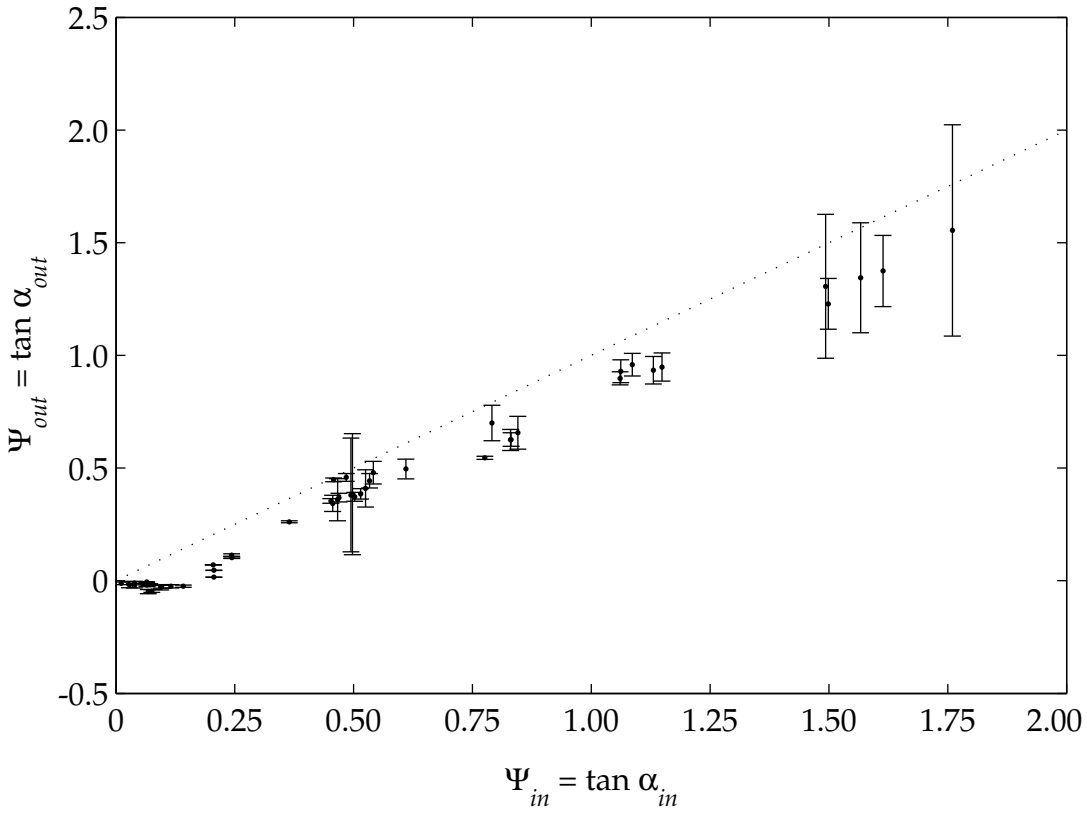

Figure 4.7: Nondimensional rebound angle as a function of the nondimensional incidence angle for a 12.7 mm steel ball bearing impacting obliquely without spin on a Zerodur wall. The surrounding fluid is water ($St = 2750$, $Re = 3170$).

collisions, shown in Figure 4.10, is qualitatively and quantitatively similar to that observed in the experiments of Maw *et al.* (1981) and Foerster *et al.* (1994), and also to the dry collision data shown in Figure 4.4. For small values of Ψ_{in} a positive value of the nondimensional rebound angle is observed, a consequence of micro-slip at the beginning of the impact, as identified by Maw *et al.* (1976). The collisions between 5° and 30° incident angle exhibit negative values of Ψ_{out}, indicative of recoil in the collision. Such recoil is presumably a consequence of solid–solid contact. It was shown in §3.4 that, for glass spheres, the mean surface roughness is larger than the elastohydrodynamic lubrication minimum distance of approach h_m. Therefore, solid–solid contact is to be expected.

For α_{in} in excess of 30° ($\Psi_{in} \approx 0.6$ and higher), gross sliding occurs throughout the collision. A large scatter is exhibited by the data beyond $\alpha_{in} = 55°$. For these angles the Stokes number based on the normal impact velocity is below 70. As discussed in §3.4, the

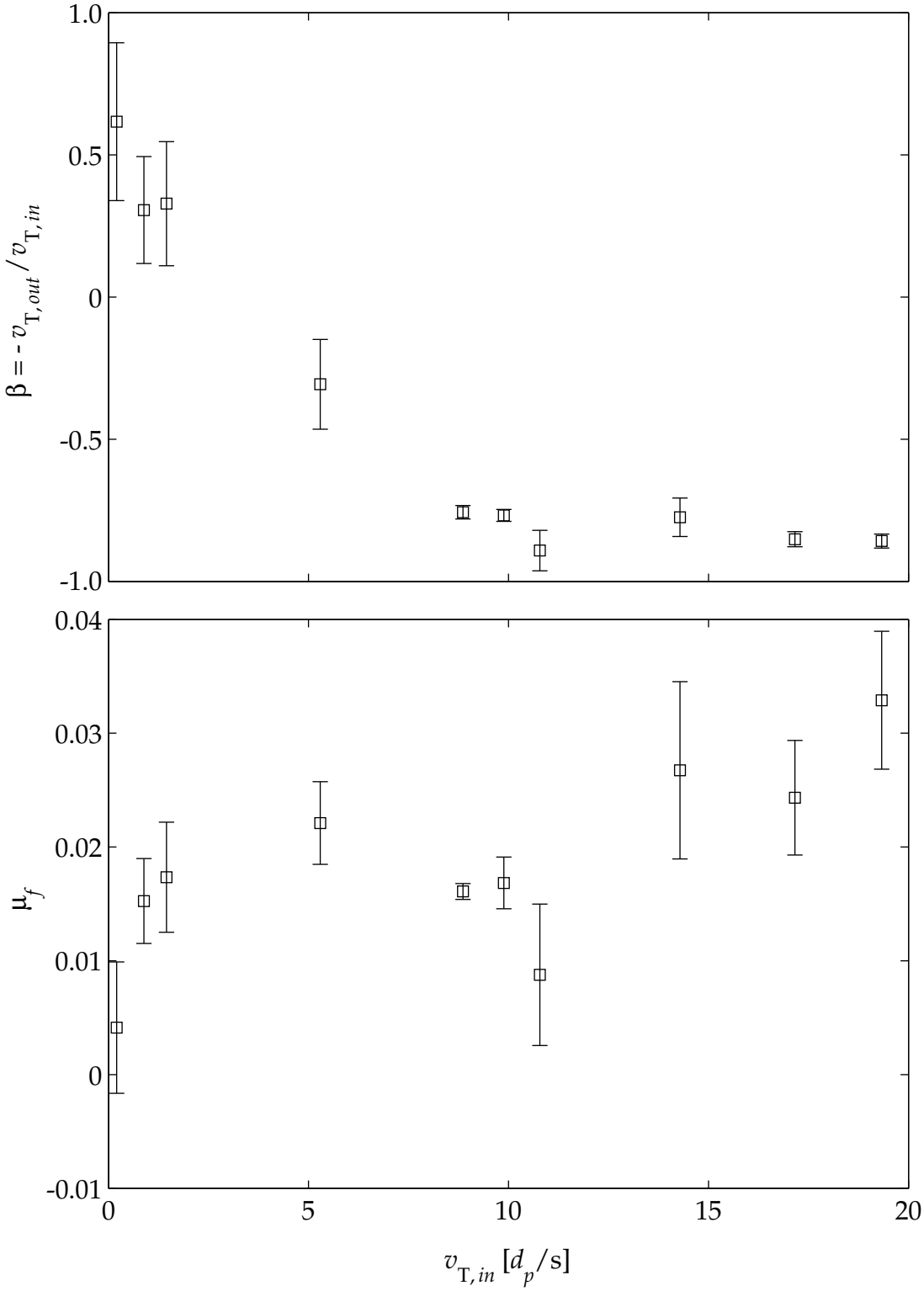

Figure 4.8: Measured rotational coefficients of restitution and computed effective coefficients of friction corresponding to the data from Figure 4.7. Each point (□) represents the average value of five distinct experimental runs (●). The error bar on each point indicates the standard deviation of the five measurements.

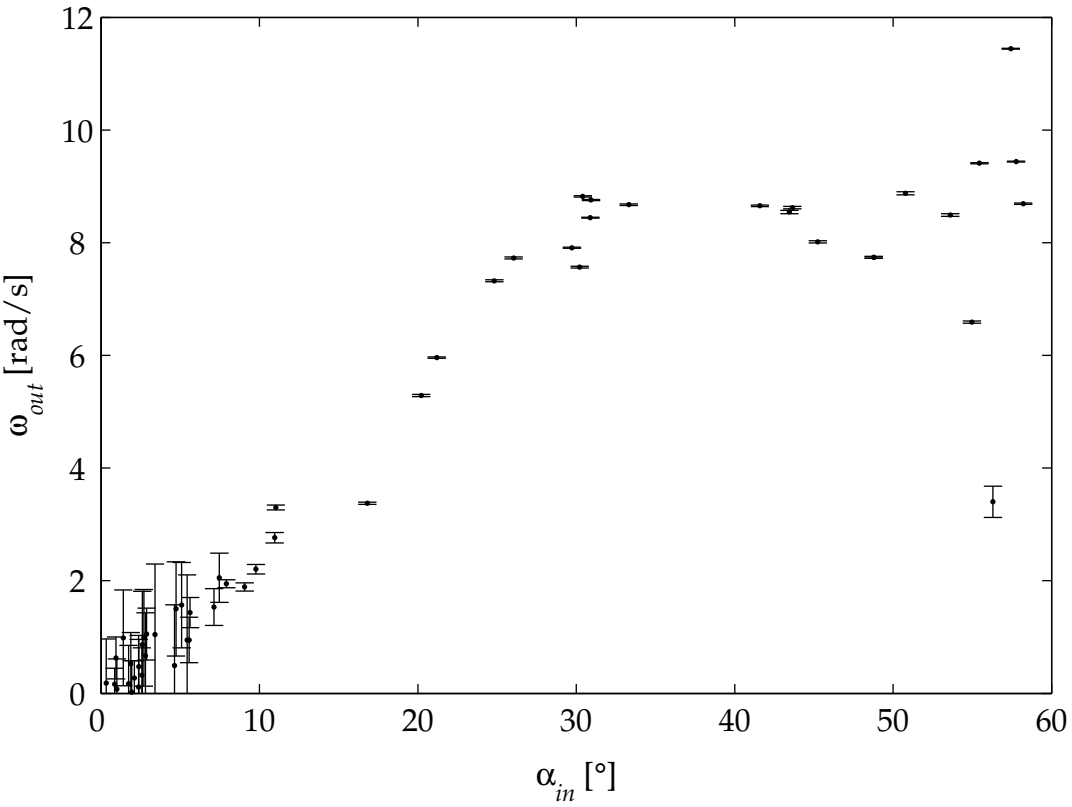

Figure 4.9: Measured angular velocity for a 12.7 mm glass sphere impacting obliquely without spin on a Zerodur wall. The surrounding fluid is a 4.5×10^{-3} Pa·s aqueous solution of glycerol (45% wt.; $St = 95$, $Re = 371$).

Hertzian contact area and the gap separation h_m decrease for decreasing collisional velocities. Both of these effects contribute to a larger scatter in the data (see Figure 3.2), since the local asperities at the point of contact affect the outcome of any individual collision.

A plot of the derived rotational coefficient of restitution, based on equation (4.16), is presented in Figure 4.11. The rotational coefficients of restitution for near-normal collisions correspond to a large error band. Also shown in Figure 4.11 is the coefficient of sliding friction, calculated from equation (4.17). The plot shows that for near-normal collisions there is no sliding, as anticipated from Figure 4.10.

For higher tangential velocities—higher incidence angles—the computed coefficient of friction is $\mu_f = 0.14 \pm 0.02$, consistent with the measurements of Bowden and Tabor (1950). Two regions can be identified on the plot of β. The middle three data points, where $\beta > 0$, correspond to collisions where recoil is observed. For these points, the computed coefficient

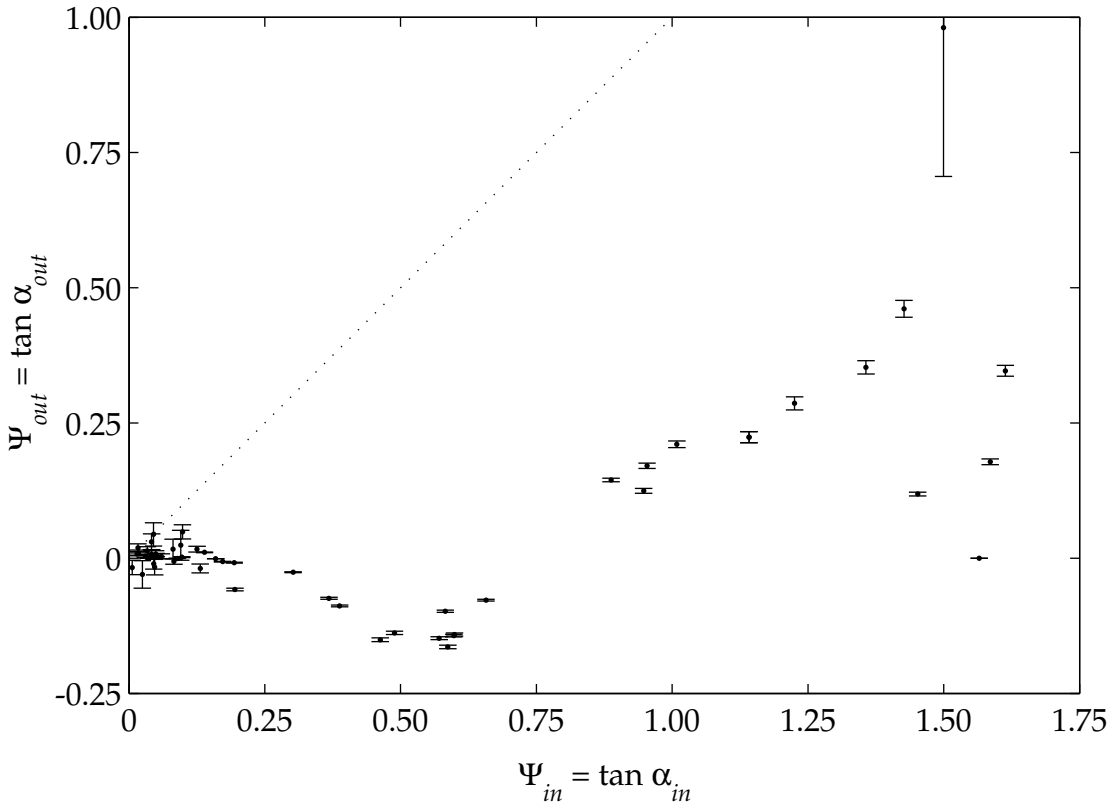

Figure 4.10: Nondimensional rebound angle as a function of the nondimensional incidence angle for a 12.7 mm glass sphere impacting obliquely without spin on a Zerodur wall. The surrounding fluid is a 4.5×10^{-3} Pa · s aqueous solution of glycerol (45% wt.; $St = 95$, $Re = 371$).

of friction is steadily rising and it can be interpreted as being proportional to the tangential force necessary to balance the tangential elastic compliance of the colliding objects. The rightmost three points, with $\beta < 0$, correspond to sliding cases where the frictional force between the surfaces is no longer enough to balance the tangential motion of the sphere. The seemingly high value of the coefficient of friction for the rightmost data point is an artifact of the variability of the data for $\alpha_{in} > 55°$.

Experiments were also performed with steel particles in glycerol–water solutions with concentrations of 37% and 78% by weight. Those concentrations correspond to viscosities of 3×10^{-3} Pa · s and 48×10^{-3} Pa · s, respectively. The results of those collisions are shown in Figures 4.12 and 4.13. Figure 4.12, for a 3×10^{-3} Pa · s ambient fluid, illustrates the same qualitative behavior as shown in Figure 4.7. Note that the experimental points in this case

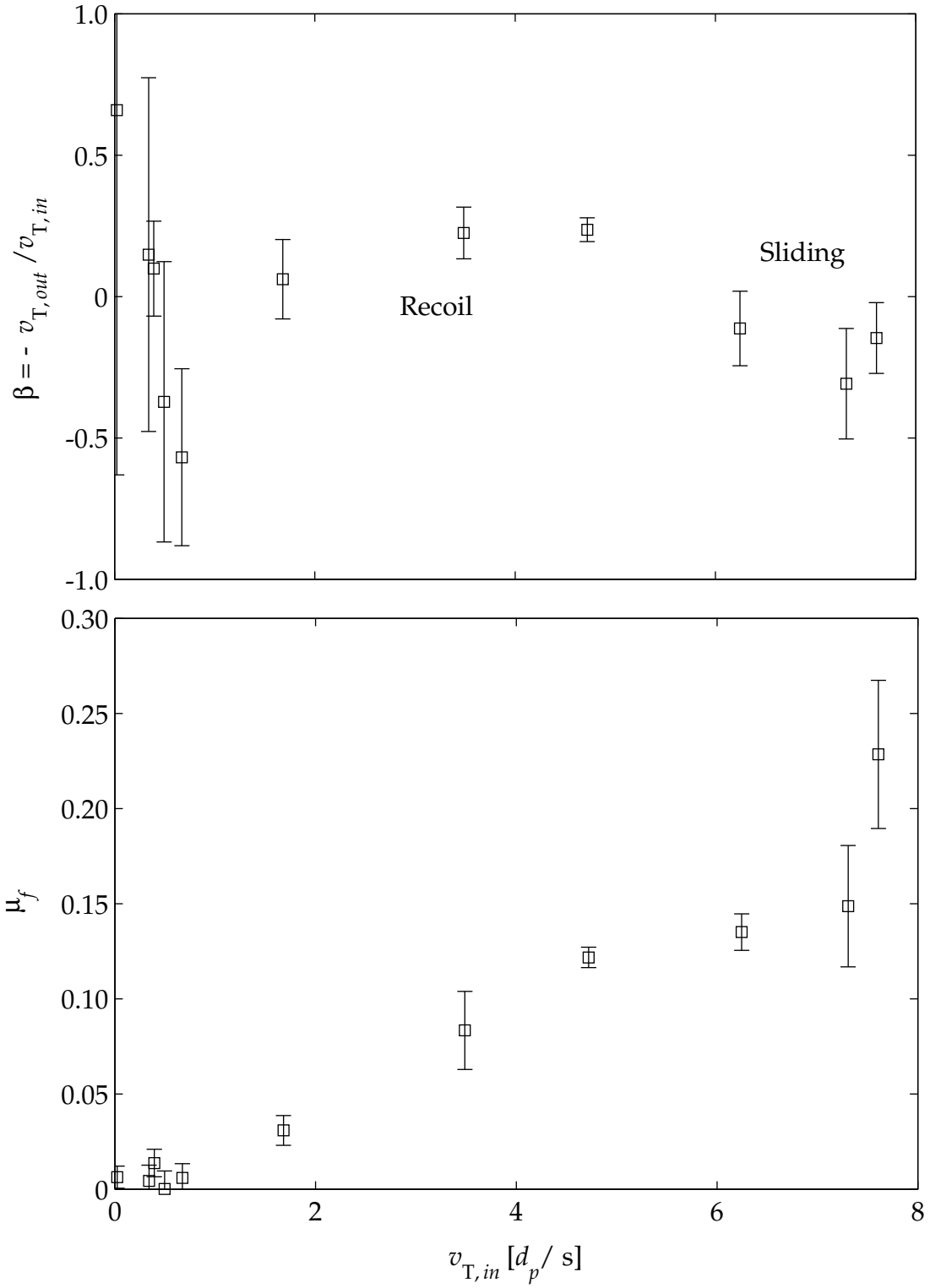

Figure 4.11: Measured rotational coefficient of restitution and computed effective coefficient of friction corresponding to the data from Figure 4.10. Each point (□) represents the average value of five distinct experimental runs (●). The error bar on each point indicates the standard deviation of the five measurements.

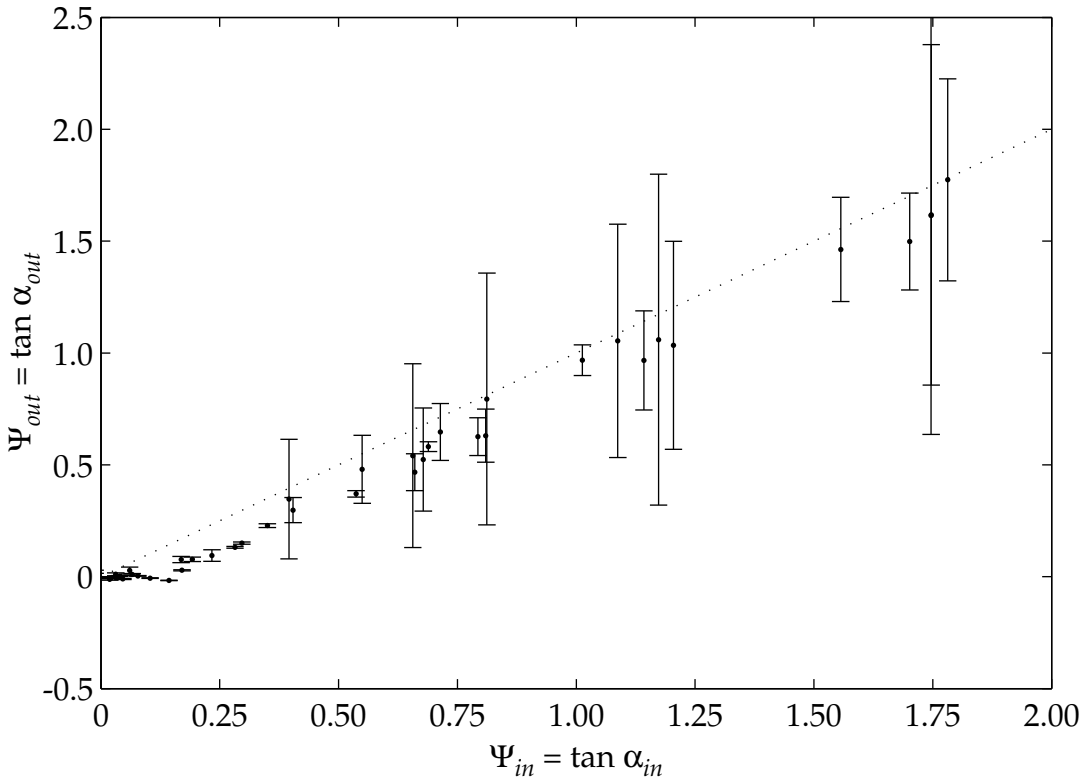

Figure 4.12: Nondimensional rebound angle as a function of the nondimensional incidence angle for a 12.7 mm steel ball bearing impacting obliquely without spin on a Zerodur wall. The surrounding fluid is a 3×10^{-3} Pa·s aqueous solution of glycerol (37% wt.; $St = 1025$, $Re = 1300$).

are closer than those from the collisions in water to the line indicating specular reflection. The slope of the data has a consistent value of one for collisions beyond $\Psi_{in} = 0.15$. Figure 4.14 shows the rotational coefficient of restitution for these collisions. The values quickly drop to a value of $\beta \approx -1$, indicative of sliding collisions. The coefficient of sliding friction computed from equation (4.18), shown in Figure 4.14, is 0.02 for all incidence angles greater than 10°.

The results for a 48×10^{-3} Pa·s surrounding liquid are shown in Figure 4.13, together with the data from collisions of glass in 45% glycerol–water presented in Figure 4.10. These two experimental sets correspond to similar collisional Stokes numbers (approximately 50 for the steel and 90 for the glass). The behaviors of the two are, however, markedly different. The data for steel lie close to the line of specular reflection and exhibit no recoil. The data

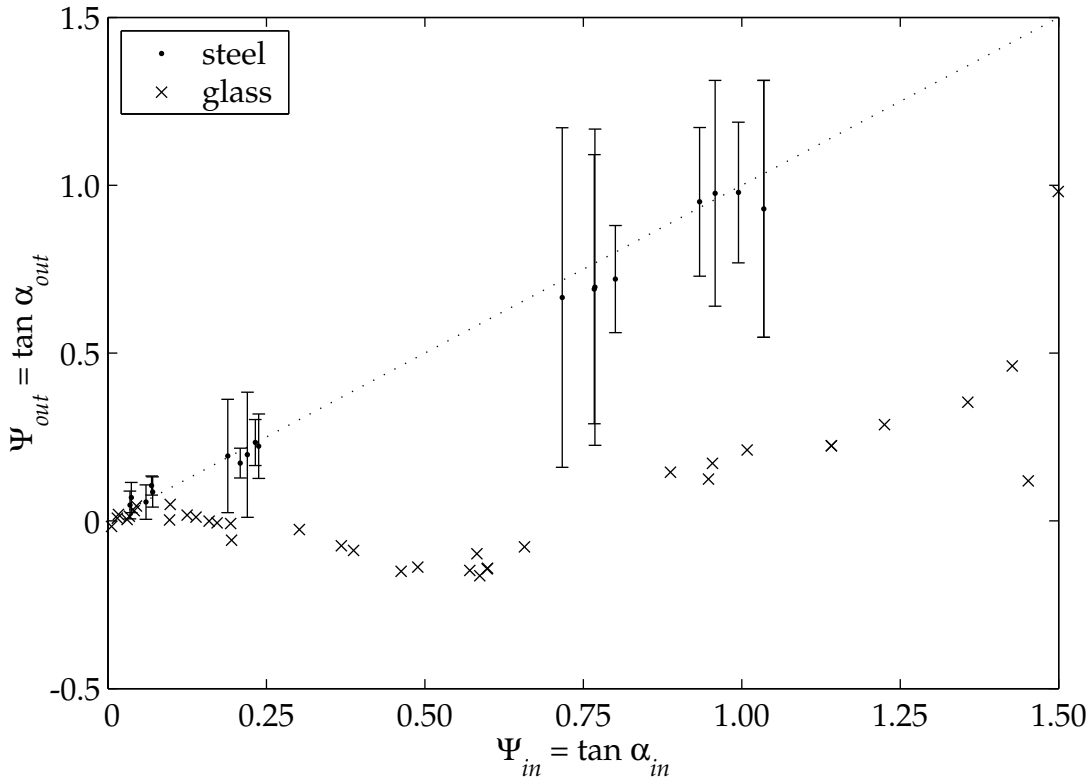

Figure 4.13: Nondimensional rebound angle as a function of the nondimensional incidence angle for a 12.7 mm steel ball bearing impacting obliquely without spin on a Zerodur wall. The surrounding fluid is a 48×10^{-3} Pa · s aqueous solution of glycerol (78% wt.; $St = 53$, $Re = 74$).

for glass, on the other hand, lie considerably far away from the specular reflection line and exhibit a coefficient of friction that slowly climbs to a value of approximately $\mu_f = 0.14$ (see Figure 4.11).

Figure 4.15 shows the calculated coefficient of rotational restitution for these experiments. The values, in the near vicinity of $\beta = -1$, indicate collisions with gross slip. Also shown is the computed friction coefficient , which exhibits a mean value of $\mu_f \approx 0.01$. The different behavior observed from the two materials can be explained by their surface roughness values. From the measurements presented in §3.4, the surface asperities on the glass beads are expected to pierce through the lubrication layer during a collision, whereas those on the steel ball bearings are not. The friction coefficient determined from the glass collisions, is consistent both with experimental values in the literature for dry and lightly lubri-

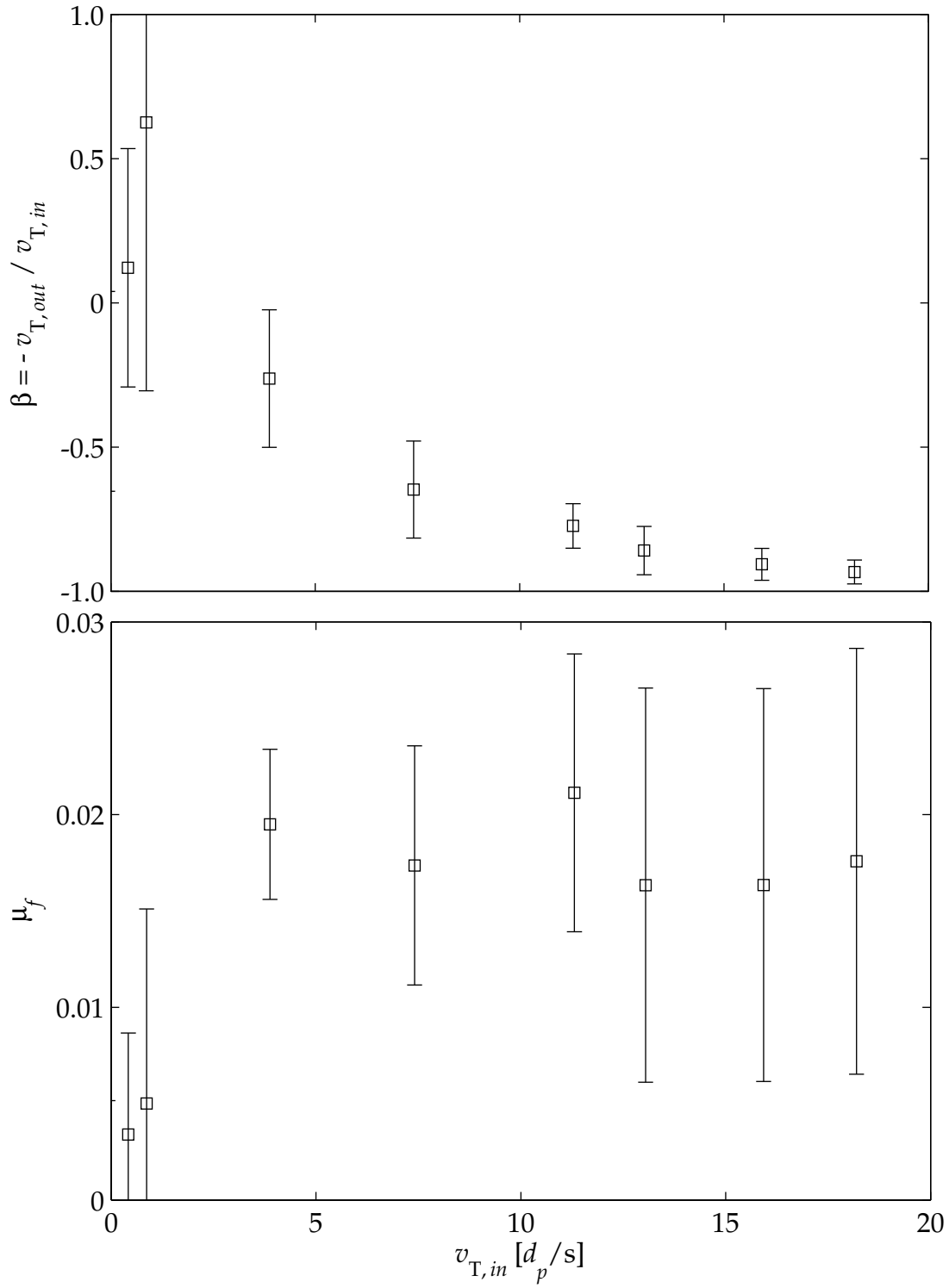

Figure 4.14: Measured rotational coefficient of restitution and computed effective coefficient of friction corresponding to the data from Figure 4.12. Each point (□) represents the average value of five distinct experimental runs (•). The error bar on each point indicates the standard deviation of the five measurements.

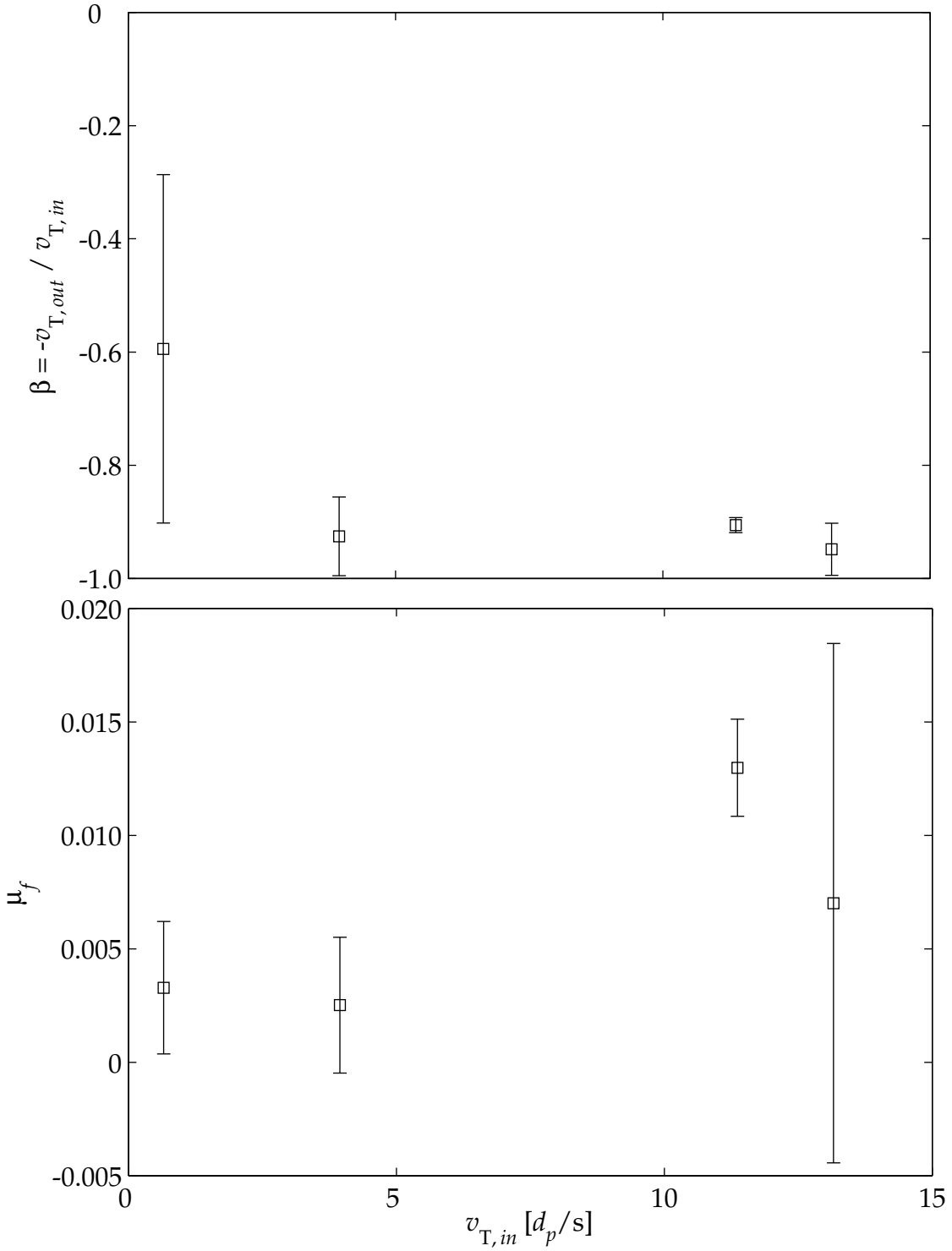

Figure 4.15: Measured rotational coefficient of restitution and computed effective coefficient of friction corresponding to the data from Figure 4.13. Each point (□) represents the average value of five distinct experimental runs (●). The error bar on each point indicates the standard deviation of the five measurements.

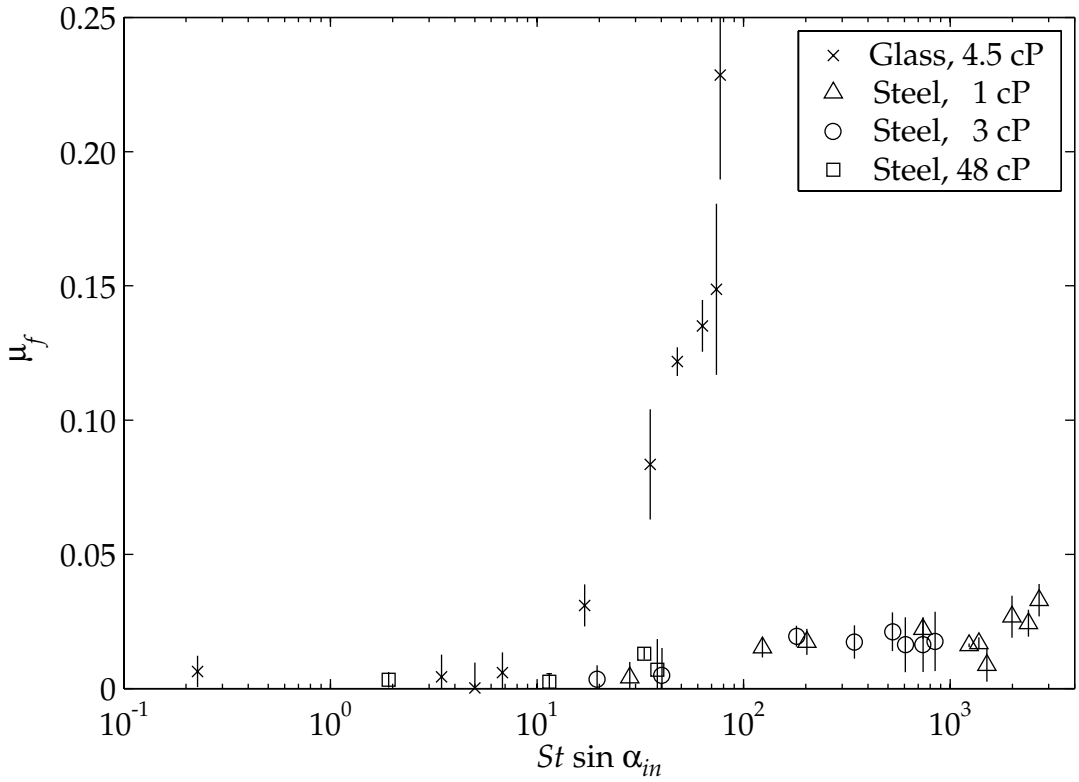

Figure 4.16: Coefficient of sliding friction, μ_f, as a function of a modified Stokes number based on the tangential velocity of impact, $St \sin \alpha_{in}$, for immersed oblique collisions in water and glycerol–water mixtures.

cated sliding and with the assumption that the surface roughness elements interact through the lubrication layer to form a solid–solid contact. In the case of the steel spheres, there are no roughness elements capable of protruding through the fluid layer; hence, all tangential force experienced by the particle should come from shear in the lubrication layer.

Figure 4.16 shows the computed friction coefficients, from Figures 4.8, 4.11, 4.14, and 4.15, as a function of a modified Stokes number based on the tangential impact velocity, $St \sin \alpha_{in}$. The friction coefficients collapse onto a single monotonically increasing function of the tangential Stokes number for glass collisions where $St \sin \alpha_{in} < 10$ and for all steel collisions. At $St \sin \alpha_{in} \approx 10$, the collisions with glass spheres diverge from the line formed by the rest of the data and their friction coefficients rapidly climb toward a value consistent with solid–solid contacts. The coefficient of rotational restitution, β, was also plotted as a function of modified Stokes numbers. None of those plots showed β to be functionally

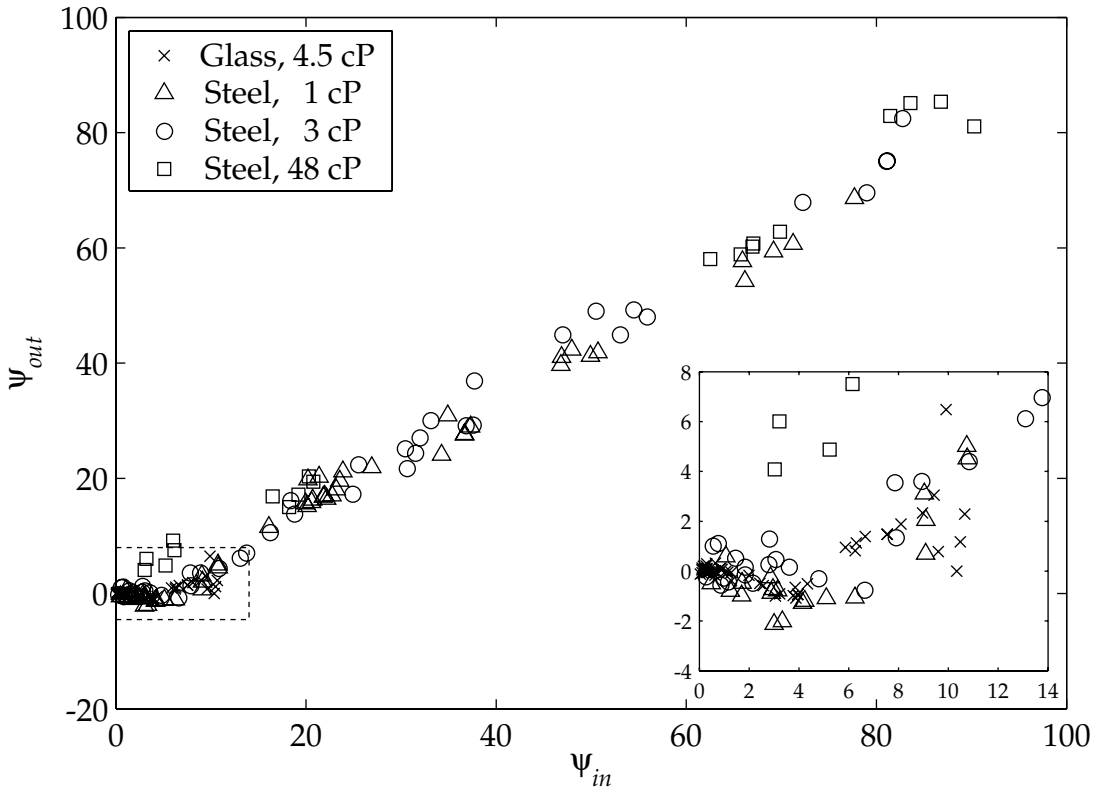

Figure 4.17: Local rebound angle, ψ_{out}, as a function of the local incidence angle, ψ_{in}, for immersed oblique collisions in water and glycerol–water mixtures.

dependent on Stokes number.

The observed trend for the friction coefficient in lubricated collisions is qualitatively consistent with elastohydrodynamic theory. During a near-normal collision the normal impact velocity is at its maximum. The minimum distance of approach, h_m, increases with increasing normal impact velocity; therefore, h_m decreases with increasing impact angle. In the case with glass, as the impact angle increases the gap becomes smaller until eventually ($St \sin\alpha_{in} \approx 10$ in Figure 4.16) the surface roughness elements make contact with the wall surface. In the cases with steel, the gap is thicker than the size of the asperities and solid–solid contact does not occur. The increasing coefficient of sliding friction is a consequence of the reduced gap separation and increased tangential velocity as the tangential Stokes number increases. These two effects combined amount to a higher shear rate and therefore a higher value of the friction coefficient.

Figure 4.17 shows the local angle of rebound, ψ_{out}, as a function of the local angle of inci-

dence, ψ_{in}, for all the immersed oblique collision experiments. The local angle of contact ψ corresponds to one of the collisional parameters introduced by Maw *et al.* (1976) and is defined in equation (4.6). The values shown in Figure 4.17 are a function of Ψ and μ_f and were obtained from equation (4.7). The individual plots of the effective angles of incidence and rebound shown in Figures 4.7, 4.10, and 4.12 collapse onto a single curve in Figure 4.17. The values of the effective angles of incidence and rebound from Figure 4.13, for collisions with steel in 78% wt. glycerol–water, do not fall on the same curve as the other three cases but lie somewhat above. Note, from Figure 4.15, that the experimental error in determining the friction coefficient for this last case is on the order of the friction coefficient itself, making it difficult to distinguish this case from a perfectly sliding collision (for which $\mu_f = 0$).

4.4 Mathematical modeling of the fluid effects

In the preceding section it was shown that, in the presence of solid–solid contact (Figure 4.10, glass spheres), an immersed oblique collision behaves like a dry oblique collision. For cases where, due to elastohydrodynamic lubrication, no solid–solid contact is expected (Figure 4.7, steel spheres), the collisions are qualitatively similar to dry collisions with a relatively small friction coefficient. The friction coefficient, computed from equation (4.18) and shown in Figure 4.16, falls for most cases within a range of μ_f from approximately 0.001 to 0.1. In the study of bearings and bushings, this range of frictional force is associated with systems that operate in an elastohydrodynamic lubrication regime (see Cameron, 1981). A possible explanation of the observed values of μ_f for the case of immersed collisions is given in this section.

4.4.1 Angular velocity after a lubricated impact

In order to determine the change in angular velocity of a sphere due to an oblique collision, the following idealized model is proposed. For the purposes of hydrodynamic torque computations, the particle is assumed to be a perfect sphere. The impact and rebound trajectory is divided into three stages, as shown in Figure 4.18: an *approach* stage, consist-

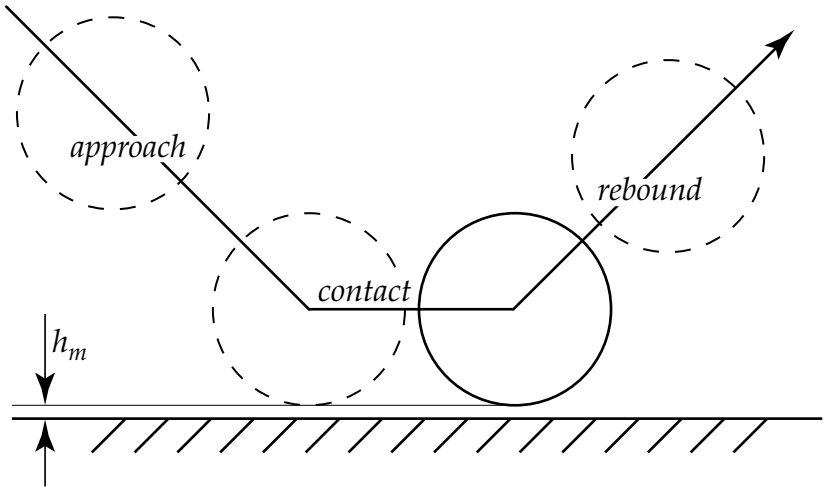

Figure 4.18: Idealized oblique collision. The sliding distance is greatly exaggerated.

ing of the superposition of the normal and tangential velocities v_N and v_T; a *contact* stage, where the sphere travels parallel to the wall at a gap separation h_m for a time τ equal to the contact time (equation (1.4); Zenit *et al.*, 1997); and a *rebound* stage, consisting again of a superposition of v_N and v_T.

Dean and O'Neill (1963) and O'Neill (1964, 1967) considered a spherical rigid particle undergoing parallel translational and rotational motion in the vicinity of a flat hard wall. Their analysis corresponds to the slow, viscous case where $Re \to 0$. The authors used specific bipolar coordinates, which allowed them to obtain exact solutions—expressed in terms of infinite series of Legendre functions—for the velocity and pressure distributions. Dean and O'Neill were then able to compute the nondimensional torque coefficients due to translational and rotational motion,

$$T_t^* = \frac{T_t}{8\pi\mu U R^2} \qquad \text{and} \tag{4.19a}$$

$$T_r^* = \frac{T_r}{8\pi\mu\omega R^3}, \tag{4.19b}$$

from their solution to Stokes's equations. Here U represents the translational velocity in the direction parallel to the wall, and ω represents an angular velocity about an axis parallel to the wall and perpendicular to the direction of translation.

As pointed out by Goldman, Cox, and Brenner (1967), these solutions converge poorly

(in a numerical sense) if the ratio of gap width to sphere radius is very small. Goldman *et al.* utilized the method of matched asymptotic expansions to explore the limit where the gap width tends to zero. Because of the linearity of the equations of motion, the combined effect of a simultaneous translational and rotational motion is the vector sum of the separate effects, $T = 8\pi\mu R^2 (U T_t^* + \omega R T_r^*)$.

In the absence of external torques on the sphere ($T = 0$), the balance of torque requires that

$$\frac{\omega R}{U} = -\frac{T_t^*}{T_r^*}. \tag{4.20}$$

In the limiting case where the sphere approaches the plane, the asymptotic solutions by Goldman *et al.* yield

$$T_r^* \sim -4 T_t^*. \tag{4.21}$$

For a perfect sphere approaching a wall without rotation, the only mechanism for spin generation is the translational motion. Equation (4.21) implies that there is no significant rotation until contact with the wall is achieved, since the counter-torque opposing rotation is large enough to prevent any translation-induced rotational motion. The contributions to the angular velocity of the approach and rebound stages depicted in Figure 4.18 are therefore negligible.

The torque T and the angular velocity ω of the particle are related by

$$T = \mathrm{d}(I\omega)/\mathrm{d}t = \tfrac{8}{15}\pi\rho_p R^5 \mathrm{d}\omega/\mathrm{d}t. \tag{4.22}$$

From equations (4.19) and (4.22) we obtain, in integral form, the change of angular velocity during a collision,

$$\Delta\omega = \frac{15\mu U}{\rho_p R^3} \int_0^t T^*(t)\,\mathrm{d}t. \tag{4.23}$$

Any initial angular velocity decays slowly due to the contribution of T_r^* to T^* in equation (4.23). From equation (4.21) it follows that, in the absence of solid–solid contact, the integral on the right-hand side of equation (4.23) must be zero. This is in direct contradiction to the experimental evidence, since measurements carried out with steel spheres, where no solid–solid contact is expected (see §3.4), do reveal a change in angular velocity.

Equation (4.23) is based on the assumption that the fluid viscosity remains constant throughout the collision. Barnocky and Davis (1989) showed that the hydrodynamic pressure that develops during a collision becomes large enough to cause the viscosity of the fluid to increase by several orders of magnitude. In particular, the pressure buildup during the collision process becomes sufficiently large that the corresponding viscosity increase causes the fluid in the gap between two colliding spheres to behave nearly as a solid. Barnocky and Davis concluded that the effect of the increase in viscosity on the normal component of a collision is minor. In the tangential direction, however, the nearly-solidified gap-fluid acts as a point force, imposing a torque on the particle.

4.4.2 Viscosity variation with pressure

A usual way of modeling the pressure dependence on viscosity is to follow Barus's law (Gohar, 2001),

$$\mu = \mu_0 \exp(\alpha^* p). \tag{4.24}$$

The pressure–viscosity coefficient α^* is a constant depending on the fluid, and μ_0 is the viscosity at the reference pressure (usually 1 atm). Tabulated values of α^* are readily available. In some cases, however, Barus's law vastly overpredicts the viscosity. In particular, Gohar (2001) warns against using Barus's law when estimating the friction force of a lubricated contact. A power law pressure–viscosity equation,

$$\mu = \mu_0 (1 + Cp)^{16}, \tag{4.25}$$

proposed by Chu and Cameron (1962), offers a more adequate relation for determining the frictional force. The coefficient C can be calculated from the pressure coefficient α^* by matching equations (4.24) and (4.25) at low pressures.

In order to evaluate the torque imposed on the particle, assume that the deformation of the contact area is Hertzian, as shown in Figure 4.19. The pressure distribution in the gap does not vary throughout the thickness of the fluid film, and is given by Reynolds's equation

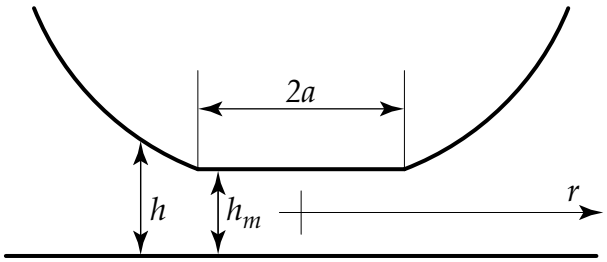

Figure 4.19: Elastohydrodynamic contact of a sphere and a wall.

for pure squeeze motion,

$$\frac{1}{r}\frac{\partial}{\partial r}\left(rh^3\frac{\partial p}{\partial r}\right) = 12\mu\frac{\partial h}{\partial t}. \tag{4.26}$$

Integrating equation (4.26) once gives

$$\frac{\partial p}{\partial r} = \frac{6\mu r}{h^3}\frac{\partial h}{\partial t}. \tag{4.27}$$

At this point it is convenient to define a pressure parameter,

$$p_0 \equiv \frac{1-(1+Cp)^{-15}}{15C}, \tag{4.28}$$

based on equation (4.25). Note that for high pressures $(1+Cp)^{-15} \to 0$ and $p_0 \to 1/15C$, a constant. Furthermore,

$$\frac{\mathrm{d}p_0}{\mathrm{d}r} = (1+Cp)^{-16}\frac{\mathrm{d}p}{\mathrm{d}r},$$

and hence, substituting equation (4.25) into equation (4.27), Reynolds's equation can be written as

$$\frac{\partial p_0}{\partial r} = \frac{6\mu_0 r}{h^3}\frac{\partial h}{\partial t}. \tag{4.29}$$

Within the Hertzian contact region the pressures are sufficiently high that $p_0 \to 1/15C$ and hence $(\partial p_0/\partial r) = (\partial h/\partial t) = 0$. The film thickness is therefore a constant, $h = h_m$. Since there is no pressure variation throughout the thickness of the film, the pressure in the contact zone has a Hertzian distribution,

$$p = p_{max}\sqrt{1-r^2/a^2}. \tag{4.30}$$

The radial variation of viscosity, from equations (4.25) and (4.30), is given by

$$\mu(r) = \mu_0 \left(1 + C p_{max} \sqrt{1 - r^2/a^2}\right)^{16}. \tag{4.31}$$

In a Hertzian contact the maximum pressure p_{max} is three-halves the mean pressure. From equations (1.2) and (1.3), the maximum contact pressure is

$$p_{\max} = \frac{3}{2}\frac{W}{\pi a^2} = \left(\frac{40}{\pi^4}\rho_p V^2 E^{*4}\right)^{1/5}. \tag{4.32}$$

Equation (4.29) cannot be used to evaluate the minimum distance of approach h_m. The film thickness (Gohar, 2001, §8.2.3) is given by the expression

$$h_m = 4.3384R \left(\frac{\mu_0 UC}{R}\right)^{5/7} \left(\frac{W}{E^* R^2}\right)^{-1/21}, \tag{4.33}$$

where U is the translational velocity in the direction parallel to the wall and the equivalent load W is given by equation (1.3). This empirical formula for h_m, presented in Gohar (2001) in dimensionless form, was obtained from extensive numerical simulations of elastohydrodynamic contacts.

The frictional traction F on the contact area is a consequence of the shear imposed on the gap by the tangential velocity of the sphere, and is given by the expression

$$F = \frac{2\pi U}{h_m} \int_0^a \mu(r) r \, \mathrm{d}r. \tag{4.34}$$

Combining equations (4.31) and (4.34), the friction coefficient $\mu_f = F/W$ takes the form

$$\mu_f = \frac{2\pi U \mu_0}{W h_m} \int_0^a \left(1 + C p_{max} \sqrt{1 - r^2/a^2}\right)^{16} r \, \mathrm{d}r. \tag{4.35}$$

Upon computing μ_f from equation (4.35) for the experimental conditions explored in this thesis, the calculated values of the friction coefficient are found to be much larger than those determined experimentally from equation (4.18). This discrepancy is due to the fact that the energy used in overcoming the viscous forces in the liquid is dissipated as heat, and

the resulting temperature rise in the film layer significantly reduces the viscosity.

4.4.3 Effect of temperature

A balance of the kinetic energy of a sphere, prior to and after impact, with the energy of deformation and viscous losses in the fluid,

$$\left\{\text{Kinetic Energy}\right\}_{in} = \left\{\text{Kinetic Energy}\right\}_{out} + \left\{\text{Inelasticity}\right\} + \left\{\text{Viscous Heat}\right\}, \quad (4.36)$$

can be used to estimate the change in temperature of the fluid film, since most of the energy dissipation of a collision occurs in the regions of contact. From the results in Chapter 3, equation (4.36) can be written as

$$Q = \frac{1}{2} M v_{N,in}^2 \left(e_{dry}^2 - e_{wet}^2 \right), \quad (4.37)$$

where Q is the viscous heat generated in the gap. For a liquid of density ρ_f and specific heat c, the change in temperature, $\Delta\theta$, in the contact region is given by

$$\Delta\theta = \frac{Q}{c\rho_f \pi a^2 h_m}. \quad (4.38)$$

This equation assumes that all the energy lost to viscous dissipation during the rebound is concentrated in the Hertzian gap. In reality, a volume of fluid somewhat larger than $\pi a^2 h_m$ absorbs the generated heat, and some of the heat is conducted away from the gap by the solid surfaces and the surrounding fluid. These effects make equation (4.38) an upper bound on the temperature increase.

Figure 4.20 shows the computed values of the lubrication friction coefficient, based on equation (4.35), for the experimental conditions explored in this thesis. The curves shown are computed for base viscosities at 20°C of 1, 3, and 48 cP, which correspond to aqueous solutions of glycerol with concentrations of zero, 37%, and 78% by weight, respectively. The combined effects of pressure and temperature have been considered when evaluating the viscosity of the interstitial fluid. Since it is not possible to directly determine from the above

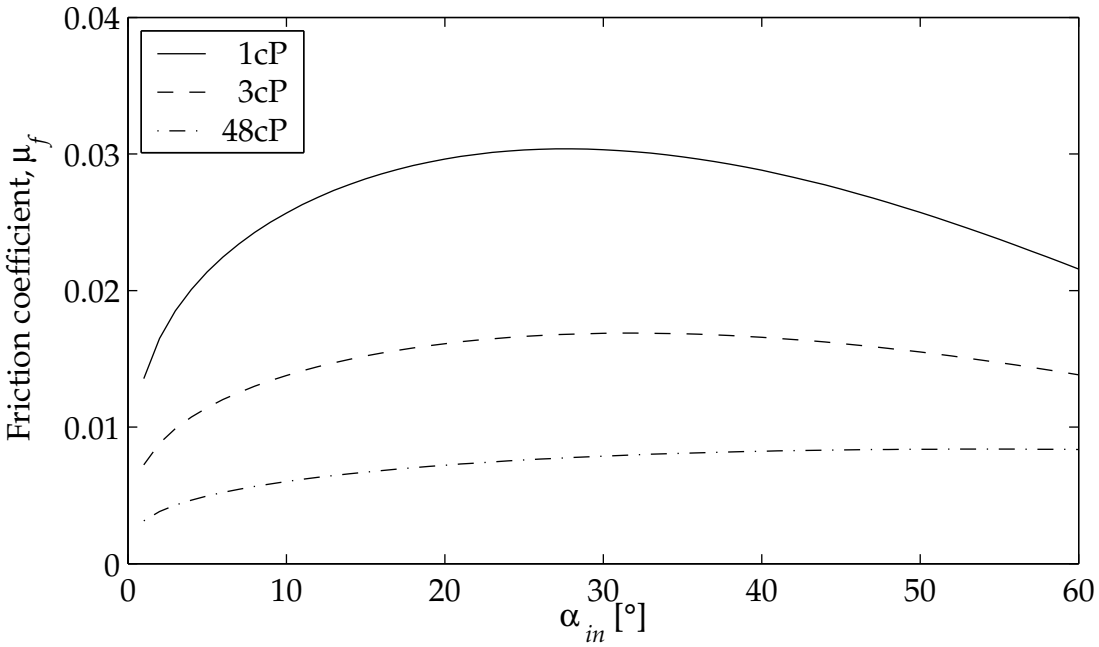

Figure 4.20: Friction coefficient, calculated from elastohydrodynamic lubrication theory, for the oblique collision of a 12.7 mm steel ball bearing in three different mixtures of glycerol and water. The predictions are based on equation (4.35).

equations the volume of fluid that absorbs the heat generated by viscous dissipation, an increase in temperature of approximately 45 K was assumed for the collisions in water. This estimated value is consistent with the temperature increase due to collisions, reported by Bowden and Tabor (1950). Even though those results are for experimental conditions quite different from the ones presented here, the choice of this value for the temperature increase is justified *a posteriori* by the comparisons in §4.4.4.

Several parameters had to be evaluated in order to compute the curves in Figure 4.20. The corresponding values are shown in Table 4.1. Experiments were performed using a 12.7 mm steel ball bearing colliding obliquely with the Zerodur wall. Aqueous solutions of glycerol with the concentrations and room-temperature viscosities detailed on the left-hand side of Table 4.1 were used as surrounding fluids.

Based on the specific heats of water and glycerol, the mix-averaged specific heat of each mixture was calculated. The values are reported on the right-hand side of Table 4.1. The specific heat of glycerol is listed for reference purposes, although no experiments were performed in 100% glycerol. Also reported in the table are the typical normal impact velocity,

Table 4.1: Parameters for the computation of elastohydrodynamic friction.

Glycerol, % wt.	visc., mPa · s	c	$v_{N,in}$	e_{wet}	Q	$\Delta\theta_{\max}$	μ_0
0	1	4.18	200 ± 50	0.95 ± 0.03	6.8	435	0.300
37	3	3.52	205 ± 75	0.88 ± 0.02	31.3	1920	0.528
78	48	2.79	197 ± 35	0.58 ± 0.05	98.7	2350	2.993
100	—	2.4	—	—	—	—	—

Aqueous solutions of glycerol. c ($\mathrm{kJ\,kg^{-1}\,K^{-1}}$); e_{wet} (dimensionless); $v_{N,in}$ ($\mathrm{mm\,s^{-1}}$); Q (μJ); $\Delta\theta_{\max}$ (K); μ_0 ($\mathrm{mPa \cdot s}$).

$v_{N,in}$, and the effective normal coefficient of restitution, e_{wet}, for each case. The mean dry coefficient of restitution of steel on Zerodur is $e_{dry} = 0.97 \pm 0.02$ (see §3.1).

The energy, Q, dissipated in the fluid as viscous heat is computed by substituting e_{dry} and e_{wet} into equation (4.37). The obtained values are listed in Table 4.1. Assuming that all the viscous heat is absorbed in the volume of fluid $\pi a^2 h_m$ within the contact area, the maximum temperature increase of the liquid, $\Delta\theta_{\max}$, is determined. The value for water is approximately 10 times larger than the estimated increase in temperature of 45 K, based on the values reported by Bowden and Tabor (1950). Note that, in reality, not all of the viscous dissipation energy is absorbed by the liquid in the contact gap. Some of the energy lost to viscous heating is dissipated in the liquid surrounding the contact area. A fraction of the energy dissipated in the gap as compressive heating is carried away from that region by conduction cooling, both to the solid surfaces and to the surrounding fluid. The convection cooling term is the only dissipation mechanism not generally thought to be significant in elastohydrodynamic contacts (Gohar, 2001, §4.5).

Taking into account the dissipation mechanisms detailed above, it is assumed here that the increase in temperature in the gap is between one-tenth of $\Delta\theta_{\max}$ (for water) and one-twentieth (for 78% wt. glycerol). The corrected viscosity of the fluid, μ_0, based on these assumed temperature increases, is reported in Table 4.1. The values of μ_0 obtained in this manner were substituted into equations (4.33) and (4.35) to generate the curves shown in Figure 4.20. The Hertzian radius of contact was evaluated from equation (1.2).

4.4.4 Comparison between experiments and theory

The curves obtained from equation (4.35) are now compared with the measured values for the coefficient of friction, as determined from equation (4.18). The experiments correspond to a 12.7 mm diameter steel sphere colliding obliquely with a Zerodur wall in glycerol–water mixtures. Figure 4.21 shows the curves from Figure 4.20 as individual plots, together with their corresponding experimental points. Each data point reflects the average of five distinct experimental measurements at a given incidence angle and impact velocity. The error bars are indicative of the dispersion of the averaged points and encompass one standard deviation.

Figures 4.21(b) and 4.21(c) show good agreement between the experimental measurements and the theory. For those cases a large fraction of the surrounding fluid (37% and 78%, respectively) is glycerol. The viscosity of glycerol, from the values tabulated in Gohar (2001), is dependent on pressure with a pressure coefficient $\alpha^* \approx 6 \times 10^{-9}\,\mathrm{Pa}^{-1}$. The corresponding coefficient C in equation (4.25) is approximately $375 \times 10^{-12}\,\mathrm{Pa}^{-1}$. On the other hand, Figure 4.21(a) has a region around $\alpha_{in} = 30^\circ$ where the experimental values of the friction coefficient are considerably lower than those predicted by equation (4.35). The upright triangles, $\triangle$, in Figure 4.21(a) correspond to the points reported in Figure 4.8. Those measurements were obtained with a pendulum made using a $\varnothing$ 127 µm leader. To ascertain that the torsional stiffness of the pendulum string is negligible, as determined in §2.1.2, a set of measurements was done using a $\varnothing$ 51 µm leader. The results obtained from those measurements are shown in Figure 4.21(a) with upside-down triangles, $\triangledown$. The same depressed values of the friction coefficient for incidence angles of approximately 30° were observed.

A possible explanation for the low values of the friction coefficient observed for water follows. At pressures up to about 150 MPa the viscosity of water decreases with pressure. As the pressure increases, water's hydrogen-bonded network of icosahedral water clusters, which is partially responsible for the viscosity of water, becomes deformed and loses strength. This reduction in cohesivity more than compensates for the reduced void volume between the water molecules, hence reducing the viscosity. At higher pressures water behaves like a nor-

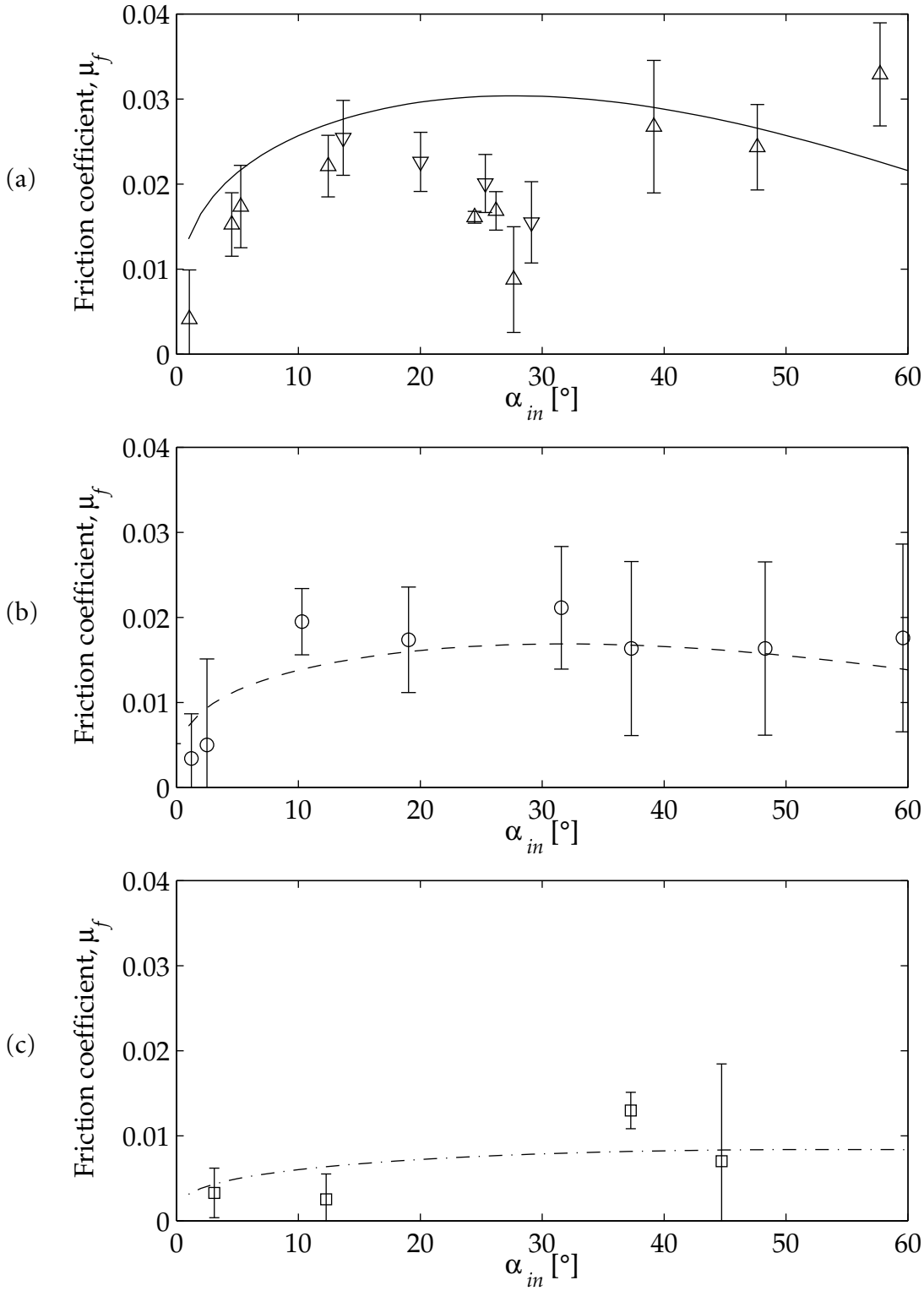

Figure 4.21: Comparison between theoretically calculated and experimentally measured friction coefficient values for collisions of a 12.7 mm steel ball bearing with the Zerodur wall. The surrounding fluids are (a) water, (b) a 37% wt. aqueous glycerol solution, and (c) a 78% wt. aqueous glycerol solution.

mal liquid and its viscosity, a function of the void fraction between the molecules, increases with pressure. With this in mind, the results with water are expected to exhibit a lower value than the prediction from equation (4.35), which assumes a power-law increase in viscosity with pressure.

4.5 Summary

Oblique collisions in a fluid exhibit characteristics similar to those of dry collisions. The results were described using a three-parameter model based on a normal coefficient of restitution, e, a rotational coefficient of restitution, β, and a coefficient of sliding friction, μ_f.

The measurements obtained from immersed collisions of rough particles are qualitatively and quantitatively similar to those obtained from dry oblique collisions. The observed rotational impulse during those impacts appears to be a consequence of the solid–solid contacts between the surface roughness elements of the colliding objects. In cases where the particles are smooth, there is a substantial decrease in the observed frictional force.

An analysis of the viscous shear in the lubrication gap for contacts of smooth spheres was performed. A model based on lubrication theory, which predicts within experimental uncertainty the frictional force experienced by a smooth sphere in a lubricated impact, was proposed. The model shows that knowledge of the combined effects of temperature and pressure on the fluid viscosity is necessary in order to estimate the tangential force during impact.

Chapter 5

Hydrodynamic effect of the wall

The proper characterization of particle collisions in a liquid depends upon the ability to accurately predict the particle velocity upon contact. For a small enough particle or a low enough far-field velocity, a significant retardation of the particle is observed as it approaches a target. The impact velocity of the particle is significantly smaller than the value predicted from viscous drag in an unbounded fluid. The effect of the wall on the approach of the particles used in the experiments described in the previous two chapters is examined here.

5.1 Approach of a particle to a wall

To quantify the effect of the wall on the trajectory of a particle, a series of experiments was performed with a free swinging immersed pendulum. The trajectories for a particle colliding with the wall and for a free swinging particle were compared for the same particle and the same initial release angle. The viscosity of the interstitial fluid was varied between $1\times10^{-3}\,\mathrm{Pa}\cdot\mathrm{s}$ and $12\times10^{-3}\,\mathrm{Pa}\cdot\mathrm{s}$. Figure 5.1 shows the trajectories for five cases. The velocities have been nondimensionalized by the velocity of the particle at a distance of 1.5 particle diameters from the wall. As seen in the figure, the velocity of the particle decreases due to viscous drag even before it reaches the vicinity of the wall. Note that, when the wall is present, there is a further reduction in the velocity of the particle as it approaches the wall. This additional retardation is due to an added mass effect, since the particle can no longer push the fluid forward ahead of its path and instead has to displace the fluid in a direction parallel to the wall. For $St = 9$ based on the impact velocity, the particle starts

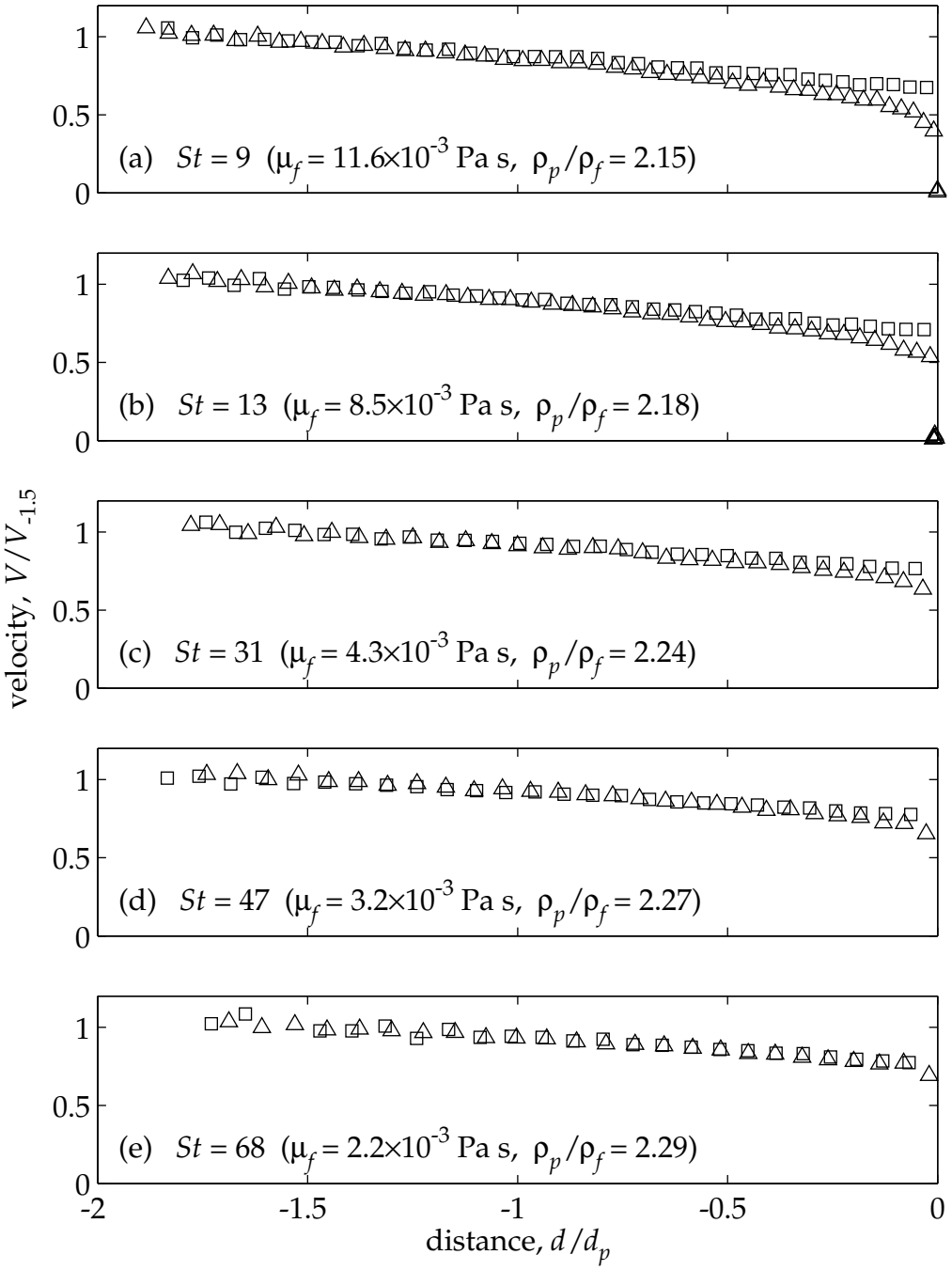

Figure 5.1: Comparison of the velocity–position plots for a particle colliding with a wall (△) and a free swinging pendulum (□). The subfigures correspond to the conditions indicated by the corresponding points in Figure 5.2.

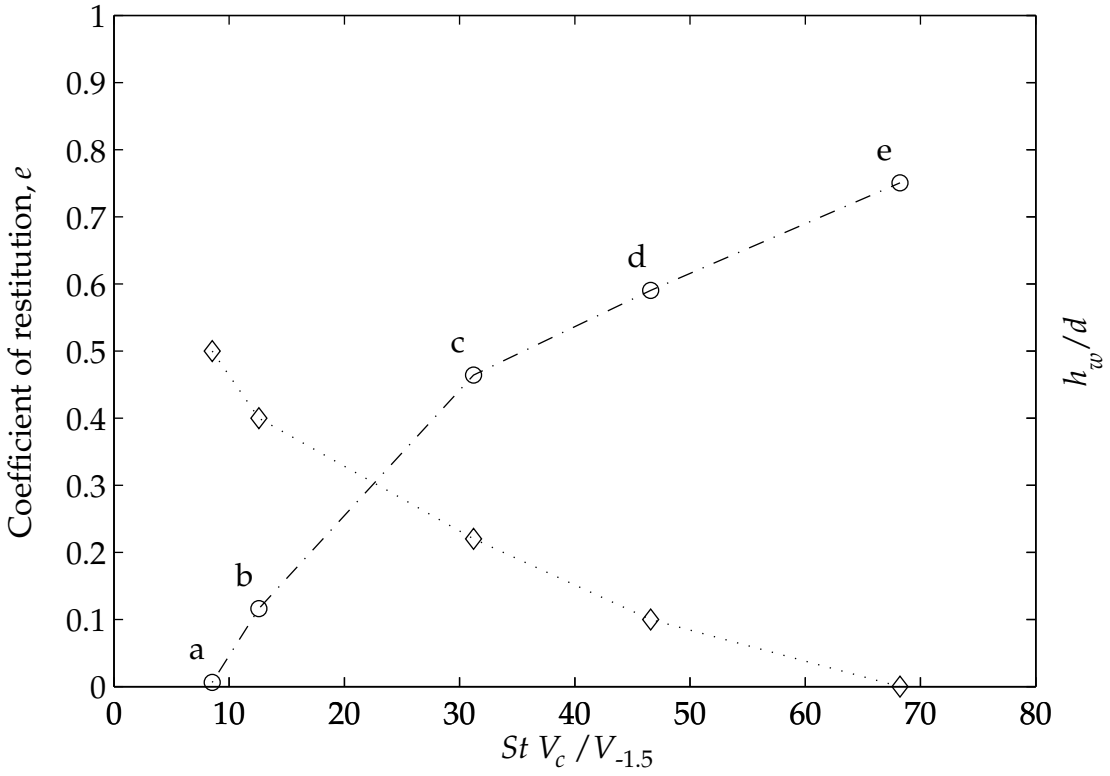

Figure 5.2: Coefficients of restitution (○) and critical distances (◇) corresponding to five trials with a 6.35 mm glass bead impacting on a Zerodur wall, immersed in glycerol–water mixtures with viscosities between (a) 11.6×10^{-3} Pa · s and (e) 2.2×10^{-3} Pa · s. The points are plotted as a function of the impact Stokes number, $StV_c/V_{-1.5}$.

decelerating at approximately 0.5 particle diameters from the wall, well ahead of the actual collision. This reduction of the velocity is also noticeable for $St = 13,\ 31,$ and 47 based on the impact velocity. By comparing the two trajectories, a distance, h_w, can be defined as a critical distance at which the velocity of the particle has dropped 5% below the velocity it would have if the wall were not there. The ratio of h_w to d_p is shown in Figure 5.2, indicating a decrease in h_w/d_p with Stokes number. For $St = 68$, there is no apparent deceleration due to the presence of the wall. The seemingly low velocity value for the last datum in Figure 5.1(e) is a consequence of the numerical differentiation of the position data obtained from the high-speed video; similar artifacts are observed in Figures 2.4 and 2.5. Figure 5.2 also shows the coefficients of restitution for the five experiments. Rebound did not occur for $St = 9$.

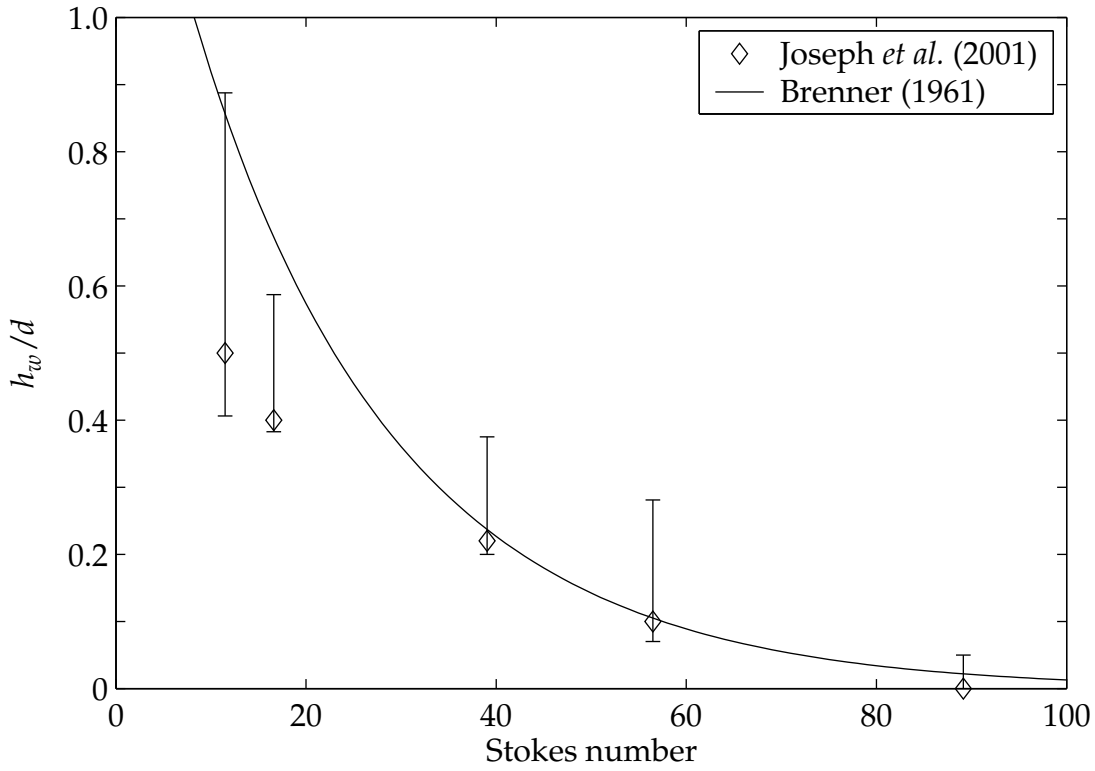

Figure 5.3: Distance, in particle diameters, at which a sphere has slowed down an additional 5% due to the presence of a wall, as a function of St at a distance of $1.5d_p$ from the wall. The solid line corresponds to the results of Brenner (1961) and the experimental points correspond to the cases in Figure 5.2. The error bars show the uncertainty of experimentally determining the point at which the additional retardation has reached 5%.

5.2 Comparison with hydrodynamic theory

The results presented by Brenner (1961) can explain the experimentally observed slowdown to a good approximation, as shown in Figure 5.3. Brenner's analysis, exact for the slow, viscous case, provides a means to determine the effect of the wall on an approaching particle. Since the hydrodynamic force diverges as the gap separation h tends to zero, Brenner's solution predicts the velocity of the particle to be zero at the time of impact. In most real cases the impact velocity of a particle is nonzero: part of the slowdown predicted by Brenner's theory is not experienced by the particle. We conclude that the theory provides an upper bound on the distance at which the effects of the wall are no longer negligible.

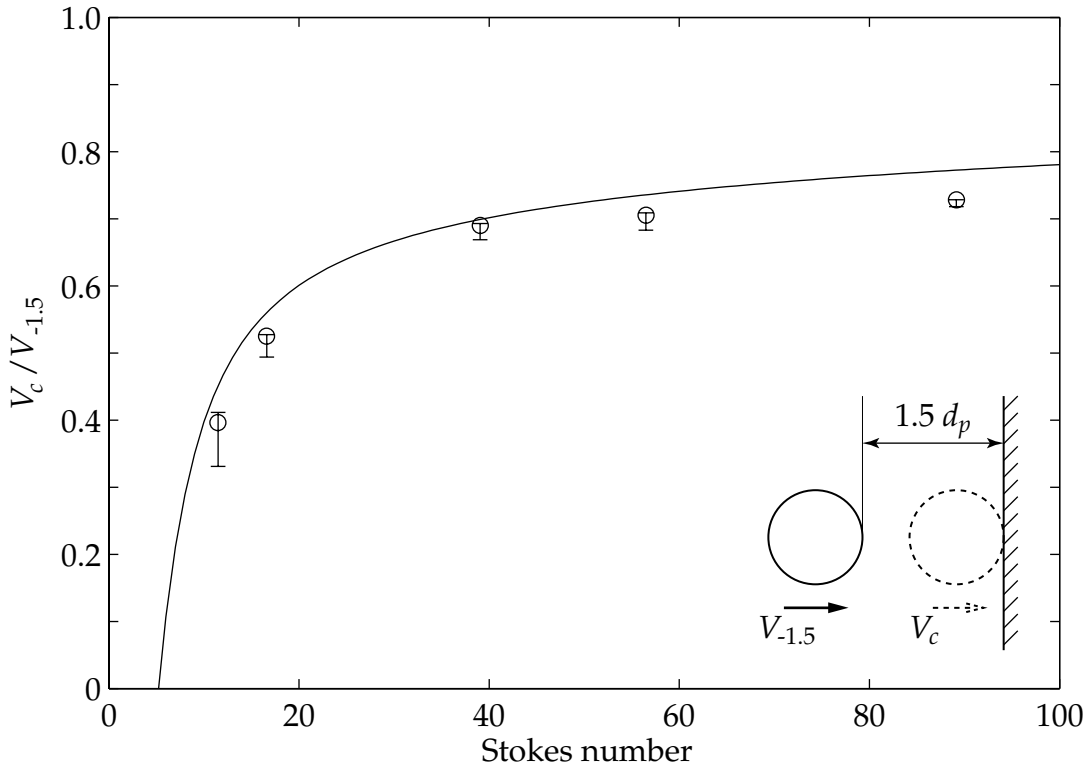

Figure 5.4: Velocity ratio for a glass sphere approaching a wall from a distance of 1.5 particle diameters up to a gap separation of 1/100 of a particle radius, as a function of *St* at a distance of $1.5d_p$ from the wall. The solid line corresponds to the numerical integration of equation (5.4).

In order to estimate the impact velocity, an approximation has been made for the purposes of this study. The correction λ applied to Stokes's law by Brenner (1961) is assumed to be applicable in the case of nonlinear drag. Following Brenner, the drag force felt by a sphere approaching a wall in Stokes flow conditions is given by the expression

$$F_{drag} = 3\pi\mu d_p V \lambda, \tag{5.1}$$

where

$$\lambda = \frac{4}{3}\sinh\eta \sum_{n=1}^{\infty} \frac{n(n+1)}{(2n-1)(2n+3)} \left[\frac{2\sinh(2n+1)\eta + (2n+1)\sinh 2\eta}{4\sinh^2(n+\frac{1}{2})\eta - (2n+1)^2\sinh^2\eta} - 1 \right]. \tag{5.2}$$

The parameter η, given by $\eta = \cosh^{-1}(1+2h/d_p)$, is a function of the gap separation be-

tween the particle and the wall.

In order to modify equation (5.1) for flows at higher Reynolds numbers, an additional correction factor,

$$\phi = 1 + 0.1935 Re^{0.6305}, \tag{5.3}$$

is introduced into Brenner's drag relation. The factor ϕ is a function of V and is based on the expressions compiled by Clift, Grace, and Weber (1978) for $Re \leq 260$. Equation (5.1) can now be written as

$$F_{drag} = 3\pi\mu d_p V \phi\lambda = -mV\frac{\mathrm{d}V}{\mathrm{d}h}. \tag{5.4}$$

The change in velocity due to the drag force in equation (5.4) can be directly integrated—keeping in mind that ϕ itself is a function of the velocity of the particle—to determine the velocity drop caused by the presence of the wall. The calculated slowdown for a 6.35 mm diameter glass sphere is compared in Figure 5.4 with the slowdown determined experimentally using the pendulum setup. The measured impact velocity V_c has been scaled by the measured particle velocity $V_{-1.5}$ at a gap separation $h = 3d_p/2$. The theoretical curve corresponds to the ratio of the calculated particle velocities at distances $d_p/200$ and $3d_p/2$. The gap separation of $1/100$ of a particle radius corresponds to the resolution of the digital camera used in the experiments.

5.3 Flow field visualization

During the course of studying the hydrodynamic effect of the wall, the flow field surrounding the sphere during the collision process was briefly investigated. A few flow visualization experiments were performed to observe the development of the flow field around the colliding particles. The flow cell was illuminated from underneath with a sheet of light from a green argon-ion laser (514.5 nm). A small amount of fluorescent dye (Rhodamine B) was placed around the particle before it was released. A typical example of the produced flow field is shown in Figure 5.5, which corresponds to a 12.7 mm Delrin particle just before and after impact.

In this example a wake is observed to develop behind the sphere before the collision

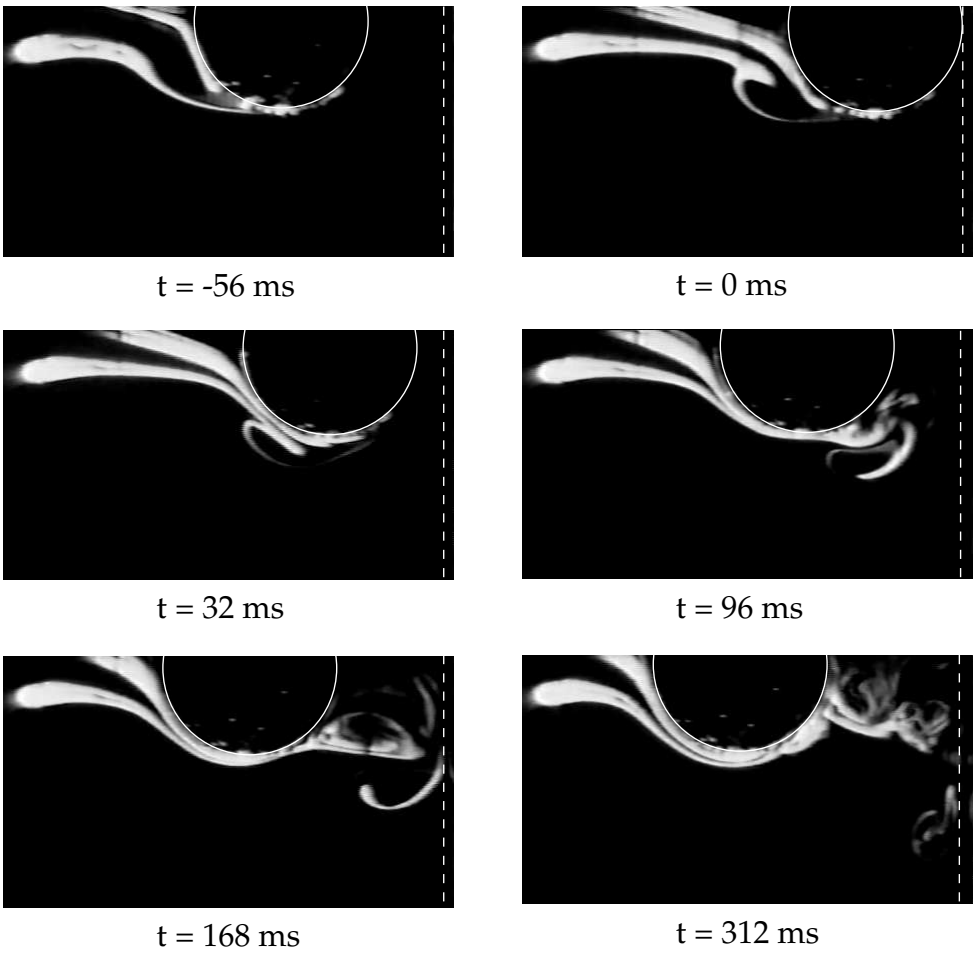

Figure 5.5: Flow field around a 12.7 mm Delrin sphere colliding with the Zerodur wall ($St = 120$). The timestamp $t = 0$ corresponds to the time of impact. For $t < 0$ the motion of the sphere is from left to right, while for $t > 0$ the sphere has rebounded and its motion is from right to left. The dashed line denotes the position of the wall. Only the the lower part of the flow field is shown.

occurs. At the moment of collision the wake detaches from the sphere and continues to move forward, in the opposite direction of the rebounding particle. As the particle moves away from the wall, a new wake is formed behind it that interacts with the original wake and produces a complex three-dimensional flow field in the gap between the sphere and the wall. A significant amount of fluid mixing is observed as a result of the rebound. The nature of the flow field was recently studied experimentally by Eames and Dalziel (2000) and by ten Cate *et al.* (2002). The latter also performed a numerical analysis based on lattice-Boltzmann simulations.

5.4 Summary

A deceleration of the particle due to the presence of the wall was observed for collisions at Stokes numbers lower than approximately 70. The distance from the wall at which the particle starts decelerating increases with decreasing Stokes number. For a Stokes number of 9, the approach is affected at a distance of approximately one particle radius.

Based on the theoretical model put forth by Brenner (1961), valid for the slow, viscous case, a modified expression incorporating some of the nonlinear drag effects of higher Reynolds numbers was proposed. The predictions from this model provide, to a good approximation, an upper bound on the distance at which the effects of a wall are no longer negligible.

Preliminary flow visualizations of the evolution of the wake generated by the motion of the sphere were obtained. A rich, three-dimensional structure was observed. Upon rebound, the wake lingers in the vicinity of the wall, with considerable mixing.

Chapter 6

Application to slurry erosion

The present chapter focuses on the erosion of a surface caused by the impact of solid particles carried by a fluid flow. The goal is to use the results obtained in Chapter 5 to estimate the collisional velocities of particles impacting a soft, ductile target in a slurry flow. Based on the estimated velocities and on the existing models for estimating the mass removal rate in dry erosion processes, a prediction of the erosion damage in a solid–liquid system is presented.

The work is entirely analytical, based on conclusions drawn from the hydrodynamic effects described in Chapter 5. In order to validate the predictions, theoretically calculated crater sizes for deformation wear are compared with the experimental results presented by Clark (1991), obtained with a slurry pot tester. A slurry pot is a device that provides a measure of the wear of cylindrical metal samples in a relatively short time. It cannot be used directly to measure the wear on components of a flow system. This type of tester presents the distinct advantage of allowing quick and easy changes in experimental conditions. The primary shortcomings of a slurry pot are the unknown fluid mechanical characteristics of the flow and the uncontrolled occurrence of particle comminution.

6.1 Erosion mechanisms

Surface erosion as a process is strongly dependent on the impact velocity of the particle causing the erosion. At a low impact velocity, the particle may not carry enough energy to exceed the plastic limit of the impacted surface and, in the absence of a cutting action, may

cause no erosion. At a higher impact velocity, a concavity with a radius of curvature similar to that of the impacting particle may be formed on the impacted surface by means of plastic deformation (Bitter, 1963). For very high speed ranges—supersonic impacts—the behavior of the impacted material changes drastically. At a supersonic impact velocity, a crater of dimension much larger than the diameter of the impacting particle is formed (Bitter, 1963).

When the elastic limit is exceeded, plastic deformation occurs in the zone of maximum stress. The resulting deformation hardens the material locally, increasing the elastic limit. Repeated collisions further increase this elastic limit until it becomes equal to the strength of the material. Any subsequent increase in the applied load—any further impacts—exceed the strength of the material and cause denudation. This type of erosion is called *deformation wear*.

For oblique collisions, the impacted material is subject to shear over an area equal to the vertical cross section of that part of the particle which has penetrated into the surface. If the shearing strength is exceeded, *cutting wear* occurs (Finnie, 1960; Finnie and McFadden, 1978; Magnée, 1995). In general, both deformation and cutting wear occur simultaneously. Depending upon the hardness and brittleness, or ductility, of the impacted material, either deformation or cutting wear may be the dominating erosion mechanism (Magnée, 1995). The focus of this chapter is on near-normal collisions on soft, ductile materials where the effects of cutting wear are negligible.

6.2 Plastic indentation

As described in §1.1 and §4.1, the interaction between two colliding spheres is described by the Hertz contact theory (Timoshenko and Goodier, 1970). A flat surface can be represented by letting one of the spheres have an infinitely large radius. The radius a of the contact area of a sphere of diameter d_p and density ρ_p impacting a flat body at a velocity V is given by equation (1.2). The equivalent load due to the impact, W, is obtained from equation (1.3). The maximum surface pressure $p_{\max} = \frac{3}{2} p_{\text{average}}$ is, from equations (1.2) and (1.3),

$$p_{\max} = \left(\frac{40}{\pi^4} \rho_p V^2 E^{*4} \right)^{1/5}. \tag{4.32}$$

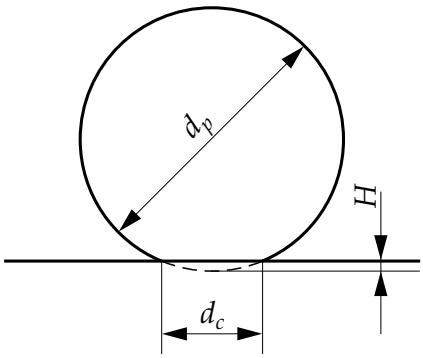

Figure 6.1: Plastic indentation of a flat surface with a sphere.

The onset of plastic deformation corresponds to $p_{\max} = \sigma_{el}$, the elastic load limit. From equation (4.32) the collision velocity at which the elastic limit is reached,

$$V_{el} = \frac{\pi^2 \sigma_{el}^{5/2}}{2E^* \sqrt{10\rho_p}}, \tag{6.1}$$

can be determined. Following Bitter (1963), the contact area is divided into two regions: a circle of diameter d_c, where plastic deformation occurs, and an annulus around it, where only elastic deformation occurs. The area of the annulus of elastic deformation is equal to the Hertzian contact area for a perfectly elastic collision in which $p_{\max} = \sigma_{el}$. The crater of depth H left behind after all of the elastic load has been removed is depicted in Figure 6.1.

For most ductile materials, σ_{el} can be assumed to be governed by the von Mises shear strain energy criterion. The von Mises criterion states that failure occurs when the energy of distortion reaches the yield energy σ_y of the material under simple tension (or compression) (Johnson, 1985). For a Hertz pressure distribution with $\nu = 0.34$, the maximum stress concentration occurs at a depth of $0.247 d_p$ and corresponds to $0.602 p_{\max}$ (Davies, 1949; Johnson, 1985). Thus, by the von Mises criterion, $\sigma_{el} = 1.66\sigma_y$ is the stress at the elastic limit. For any stress beyond σ_{el} yield is expected to occur.

The energy Q_p devoted to plastic deformation during a collision is directly proportional to the mass $M = \pi \rho_p d_p^3/6$ of the impacting particle. Bitter (1963) shows that this energy is given by

$$Q_p = \frac{1}{2} m (V - V_{el})^2 . \tag{6.2}$$

Equation (6.2) is valid as long as the particles impinge normally to the body surface.

6.3 Fluid effect on the impact velocity

For a collision in a fluid of viscosity μ and density ρ_f, the impact velocity of a particle is lower than the velocity of the same particle far away from the wall. In §5.1 it was shown experimentally that, when a wall is present, there is a further reduction of the velocity of the particle than what would be expected exclusively from drag in an unbounded fluid.

In situations where $Re \cdot x/d_p$ is smaller than unity—Re is the particle Reynolds number—the fluid inertia effects can be assumed to be negligible. In such cases, an approach based on lubrication theory can be used to calculate the retardation of the particle due to the presence of the wall. Based on a derivation by Davis *et al.* (1986), equations (3.1) and (5.4) can be rewritten as

$$F_{drag} = 3\pi\mu d_p V \frac{d_p}{2x} = -mV\frac{\mathrm{d}V}{\mathrm{d}x}.$$

The collision velocity V_c of a particle in close proximity to a wall and immersed in a viscous fluid can be obtained, to leading order, as a function of the distance x between the particle and its target,

$$\frac{V_c}{V_0} = 1 + \frac{1}{St_0}\ln\frac{x_c}{x_0}. \tag{3.2}$$

Here V_0 is the velocity at an initial distance x_0 and St_0 is the particle Stokes number at x_0. The distance x_c is the critical distance at which lubrication theory breaks down due to surface roughness elements. The mean surface roughness can be considered to be smaller than 1 μm (Clark, 1991; Joseph *et al.*, 2001).

6.4 Analysis of a slurry pot

The material removal due to the plastic deformation caused by a single impacting particle can now be calculated. Clark (1991) conducted a series of slurry pot erosion tests with dilute water–glycerol suspensions of glass beads and determined both the rate of particle impact and the dimensions of the impact craters. The slurry pot used by Clark consisted of a cylin-

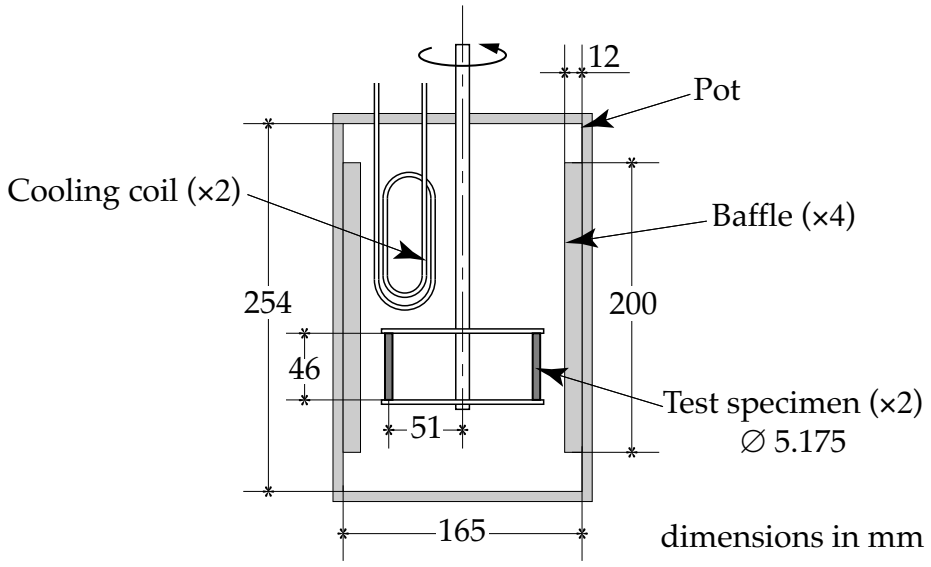

Figure 6.2: Schematic diagram of the slurry pot used by Clark (1991).

drical container of 165 mm in diameter and 254 mm in height, like the one shown in Figure 6.2. Two oxygen-free high-conductivity copper rods were used as targets. The test specimens were placed on an anchor impeller as shown in the figure. The vessel was equipped with four baffles extending into the pot to disrupt the liquid rotation during testing. The test temperature was controlled to within 1°C in order to ensure repeatable experimental conditions. Based on the hardness of the test specimens reported by Clark, measured after annealing for one hour at 300°C, an elastic load limit of 132–148 MPa can be estimated (Tabor, 1951).

The measured crater diameters reported by Clark (1991), nondimensionalized by the diameters of the impacting particles, are shown in Figure 6.3 as a function of St_N, the Stokes number based on the nominal test speed V_N. The dimensionless crater size, d_c/d_p, is a measure of the fraction of kinetic energy devoted to plastic deformation. The choice of reporting Clark's data as a function of Stokes number was made because this representation allows for a direct comparison with the results presented in Chapter 5. Furthermore, since the effective immersed coefficient of restitution was shown in Chapters 3 and 4 to be a function of Stokes number, presenting the collisional data obtained by Clark (1991) as a function of Stokes number is a natural choice. In all cases, the crater size goes to zero for

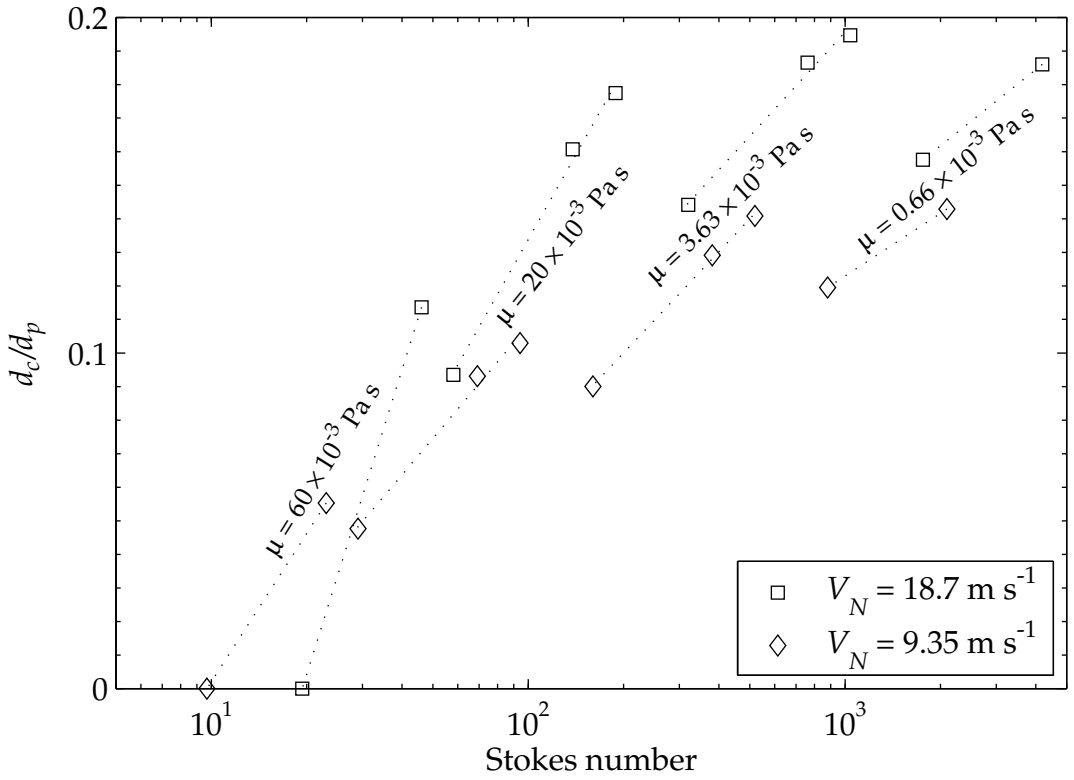

Figure 6.3: Crater diameters for the different experimental conditions explored by Clark (1991). The lines are intended to guide the eye.

St_N between 10 and 20. This range is consistent with the critical value of Stokes number, $St_{\text{crit}} \approx 10$, at which no rebound occurs (see §3.3).

Clark determined the kinetic energy of the impacting beads by comparing the craters formed in his experiment with those produced by hardness test indentation of the surface. By assuming that all the kinetic energy was expended in plastic deformation of the copper specimen, he was able to directly calculate the impact velocity. To compute a collisional velocity V_c for each of Clark's experiments without prior knowledge of the impact crater size, a far-field velocity must be determined. As a first estimate, the far-field velocity is assumed to be the nominal test speed V_N. Based on the results in Figure 5.3, the far-field is assumed to begin in the vicinity of 1.5 particle diameters away from the test specimen. By integrating equation (5.4) from $x = 3d_p/2$ to x_c, a collisional velocity V_{cN} (based on V_N) can be obtained.

The value of V_N overestimates the far-field velocity since, as the specimens are rotated

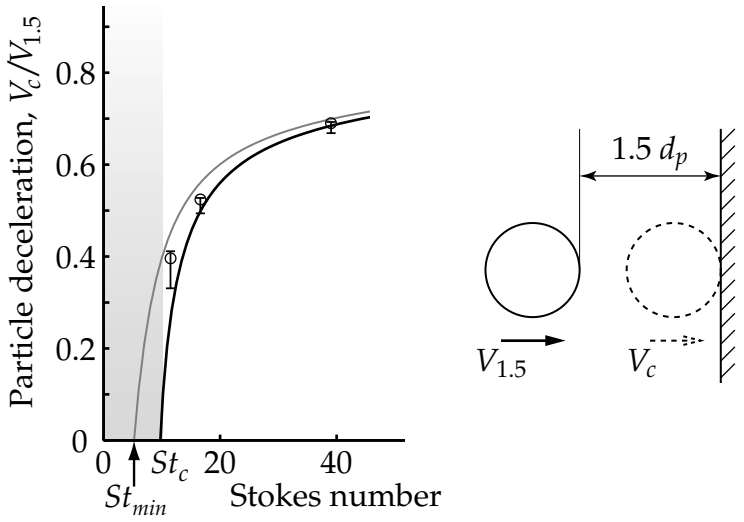

Figure 6.4: Modified deceleration of a sphere due to the presence of a wall. The theoretical curve from Figure 5.4 has been shifted so that its zero-crossing is displaced from $St_{\min}$ to St_{crit}.

around the pot tester by the impeller, the slurry is also rotated to a certain extent. This necessitates a correction to the far-field velocity. An upper bound on the correction factor can be obtained by assuming that the drag in the fluid is dominated by form drag. The areas of the baffles and of the test specimens can be determined from the dimensions of the tester shown in Figure 6.2. The projected area of the test specimens, A_s, in the direction normal to the flow is approximately 475 mm^2. The total area of the baffles, A_b, is approximately 9600 mm^2. Neglecting the effect of the frame that holds the test specimens, the swirling velocity of the rotating slurry can be estimated from the ratio A_s/A_b of the projected areas and the nominal speed of the tester, V_N. In order for the drag on the test specimens and the baffles to balance, the swirl velocity must be $V_N A_s/A_b$. Since the test specimens move at a velocity V_N, an upper bound on the collisional velocities is given by $1 - A_s/A_b$. This value is an upper bound because it is based on the assumption that the baffles contribute their entire area toward generating shape drag.

For a target impacted by a particle, the absence of a crater can be the consequence of either a purely elastic impact or no impact at all. The no impact condition is satisfied when the relative velocity of the particle with respect to the target goes to zero (from Figure 5.4, at Stokes number $St_{\min} \approx 5$). The low Stokes number region of Figure 5.4 is reproduced

in Figure 6.4. The theoretical curve, originally intersecting the horizontal axis at $St_{\min}$, has been shifted so that its zero-crossing occurs at St_{crit}. The shaded area represents the Stokes number region within which no rebound is observed for any of the experimental conditions explored in this thesis. The ratio $St_{\min}/St_{\text{crit}}$ can be used as a lower bound on the correction factor for the collisional velocities based on V_N. This lower bound on the correction factor is used in the present calculations, since it provides a better match to the results by Clark (1991) than the upper bound does.

The values of $V_c = V_{cN} St_{\min}/St_{\text{crit}}$ for the experimental conditions explored by Clark (1991) are shown in Table 6.1. The corresponding collisional Stokes numbers are also reported. Most of the collisions occur for St_c between 10 and 2000, the range explored in Chapter 3. Within this range, the approximations used for computing the collisional velocity are accurate to within 10%.

The energy Q_p devoted to plastic deformation can be calculated from equation (6.2). From this energy, the diameter d_c of the formed permanent indentation can be calculated directly from

$$Q_p = \frac{1}{4} \int_0^H \pi d_c^2 \sigma_{el} \, \mathrm{d}H, \tag{6.3}$$

since the crater has the same radius of curvature $d_p/2$ as the impacting sphere, *i.e.*, $d_c^2 = 4d_pH - 4H^2$ (see Figure 6.1). The calculated values for d_c are shown in Table 6.1; they predict the experimentally obtained crater dimensions well within the accuracy of the approximations employed. Figure 6.5 shows a comparison between the calculated and experimentally measured crater sizes. The theoretical curves slightly overpredict the crater sizes, which can be attributed at least in part to the fact that plastic hardening was not taken into consideration when deriving equations (6.2) and (6.3).

6.5 Summary

The size of the crater formed by the impact of a single particle against a ductile target was estimated for various flow conditions. An analysis based on the hydrodynamic effect of a wall on the trajectory of a particle was used to estimate the impact velocities of the solid

Table 6.1: Collisional velocities and crater diameters for a slurry pot erosion tester.

Bead diameter d_p (μm)	V_c (m s^{-1})	St_c	d_c (μm) calc.	d_c (μm) Clark (1991)
$V_N = 18.7$ m s^{-1}				
$\mu = 0.66\times10^{-3}$ Pa·s				
750	6.67	2037	158.9	–
500–600	6.62	1483	116.1	102.3
212–250	6.46	608	48.2	36.4
$\mu = 3.63\times10^{-3}$ Pa·s				
750	6.27	348	154.1	146.0
500–600	6.17	251	112.1	102.6
212–250	5.80	99	45.7	33.3
$\mu = 20\times10^{-3}$ Pa·s				
750	5.44	55	143.6	133.1
500–600	5.21	39	103.1	88.4
212–250	4.24	13	39.1	21.6
$\mu = 60\times10^{-3}$ Pa·s				
750	4.33	15	128.2	–
500–600	3.83	9	88.5	62.5
212–250	1.45	2	22.9	none
$V_N = 9.35$ m s^{-1}				
$\mu = 0.66\times10^{-3}$ Pa·s				
750	3.28	1001	111.6	–
500–600	3.25	728	81.4	78.6
212–250	3.14	295	34.4	27.6
$\mu = 3.63\times10^{-3}$ Pa·s				
750	3.01	167	107.0	105.6
500–600	2.94	120	77.6	71.0
212–250	2.69	46	31.1	20.8
$\mu = 20\times10^{-3}$ Pa·s				
750	2.43	24	96.1	77.2
500–600	2.24	17	67.7	51.2
212–250	1.42	4	22.6	11
$\mu = 60\times10^{-3}$ Pa·s				
750	1.50	5	75.5	–
500–600	1.05	3	46.3	30.4
212–250	0	0	0	none

Collisional velocities V_c and crater diameters d_c for a slurry pot erosion tester. Calculated and experimental (Clark, 1991) crater diameters are contrasted for several nominal test conditions.

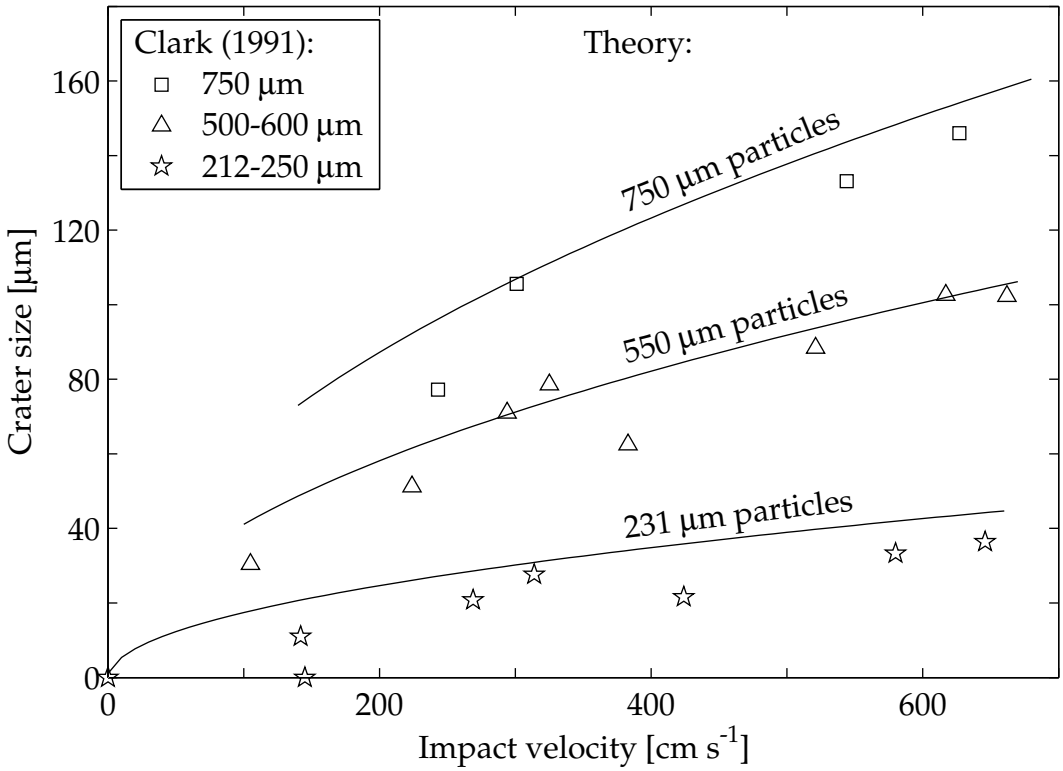

Figure 6.5: Comparison between crater diameters calculated from theory and those measured by Clark (1991).

particles in a slurry pot tester. The predicted crater sizes were calculated from the estimated impact velocities and material properties. The resulting predictions are in agreement with experimental data in the literature, suggesting that erosion rates can be estimated from theory for simple slurry flows.

Chapter 7

Conclusion

7.1 Summary

The effect of an ambient fluid on the impact and rebound of a sphere colliding with a wall was studied. An experimental pendulum apparatus consisting of a sphere attached to a thin string was used to control the trajectory of each collision. The target wall was a thick Zerodur block in most experiments; a thick Lucite wall was also used. The azimuthal orientation of the target block was adjusted so that normal and oblique collisions could be analyzed. The pendular setup and target block were placed inside a small tank so that collisions in a surrounding liquid could be performed. Steel, glass, nylon, and Delrin particles were used, in an aqueous glycerol solution. The motion of each sphere was recorded using a high-speed digital video camera. From the image analysis of the individual frames of the resulting movie, the particle's position and angular orientation were determined.

An effective coefficient of restitution, e, was defined based on the normal components of the velocity of the particle just prior to and after impact. Some benchmarking experiments with air as the surrounding fluid were performed. The results from those experiments compare favorably with results in the literature. A few trials were done with a thinner target wall, and large variations in the data were observed for walls with thickness on the order of the impacting particle's diameter. It was concluded that the experimental measurements had to be made using the thick walls in order to attain good repeatability.

In the case of an immersed collision, the effective coefficient of restitution provides an overall measure of the energy dissipated during the collision, with no distinction between

losses due to viscous dissipation and losses due to inelasticity in the contacts. The ratio of the effective coefficient of restitution to the dry coefficient of restitution, e/e_{dry}, more precisely reflects the energy losses due to the presence of the ambient fluid.

The elastic properties of the particles and the walls were found to have little effect on the value of the dry-scaled coefficient of restitution. Independent of the particles and walls used, a single curve with moderate scatter was obtained when plotting e/e_{dry} as a function of the Stokes number based on the impact velocity. The coefficient of restitution was shown to increase with increasing Stokes number. Four interrelated rebound regimes were observed:

- A critical value of $St \approx 10$ was found below which rebound does not occur. For such slow collisions, the kinetic energy of the particle is completely dissipated as viscous drag in the surrounding fluid.

- A deceleration of the particle due to the presence of the wall was observed for St between 10 and 70. In this range, the fluid inertia dominates the motion and the particle is forced to slow down due to the added mass effect of having to expel the liquid from the gap between itself and the wall.

- No apparent deceleration was observed for St above 70. The particle inertia dominates during the approach and the only slowdown observed is akin to that of an object in an unbounded fluid.

- For St of about 1000 and higher, the coefficient of restitution approached the dry value asymptotically. For such fast collisions, the fluid effects can be neglected with little loss in accuracy.

A simple analytical model based on Stokes drag and elastohydrodynamic theory was proposed. The model predicts that the dry-scaled effective coefficient of restitution increases rapidly for Stokes numbers above the critical Stokes number for no rebound. For Stokes numbers above approximately 100, the model predicts a slow asymptotic approach of e to e_{dry}. Based on this model and on the surface properties of the particles, an explanation of the variance of the data was proposed. For materials with a surface roughness comparable to the minimum distance of approach predicted by elastohydrodynamic theory, the

roughness elements are expected to protrude through the fluid layer. Under those conditions, a solid–solid contact is to be expected. The contact between roughness elements can explain the characteristic variance presented by the experimental values for *St* less than 80. The variance was on the order of the experimental uncertainty for smooth particles and considerably larger for the rougher particles.

Oblique collision experiments were performed by changing the azimuthal orientation of the target block in the experimental setup. The incidence angle was defined as the angle between the plane of the pendulum and the normal to the wall surface. The particles in the pendular setup were released without rotation, and their angular orientation was tracked throughout the collision so that any change in angular velocity could be quantified. In general, two kinds of contact are identifiable in an oblique collision: a sliding contact, where there is a relative velocity between the surfaces of the colliding object, and a rolling contact, where the rotation of the particle exactly matches its translation so that the point of contact never slips. Depending upon the magnitude of the frictional force exerted by the surfaces on one another, a collision that starts by sliding can become a rolling collision.

A three-parameter model was used to describe the measurements from the oblique collision experiments. The first parameter is the normal coefficient of restitution, defined in the same manner as the coefficient of restitution for a normal collision. The second parameter, a coefficient of rotational restitution, β, is based on the tangential components of the velocity of the point of contact just prior to and after impact. This parameter encompasses the changes in the linear and angular momentum of the colliding particle. A third parameter, the coefficient of sliding friction, μ_f, provides a measure of the tangential force acting on the particle as it slides during a collision.

A few oblique collision experiments were done in air in order to evaluate the applicability of the pendular experimental setup to these kinds of collisions. The results from those measurements are in agreement with results reported in the literature. Immersed collisions were then studied. The results from collisions of rough particles, where the average asperity size is comparable to the gap separation predicted by elastohydrodynamic lubrication theory, are qualitatively and quantitatively similar to the results from dry oblique collisions.

Some similarities were found between experiments performed with smooth spheres and

those carried out with rough spheres or without an ambient liquid. The main difference between smooth and rough collisions manifested itself as a drastically reduced friction coefficient. The roughness elements of smooth particles cannot be expected to interact with the roughness elements of a smooth wall, and therefore any frictional force exerted by the wall on the particle comes from shearing the lubrication layer.

A model was proposed to explain the observed tangential force acting on a smooth sphere during an oblique collision. This model, based on lubrication theory, takes into account the dependence of viscosity on pressure and temperature. The viscosity of most liquids increases with increasing pressure. As a particle approaches a wall, a considerable rise in pressure and temperature occurs in the gap between the two. The increase in pressure tends to increase the viscosity of the fluid in the lubrication layer, whereas the temperature rise tends to lower the viscosity. A delicate equilibrium between the two effects amounts to a change in viscosity in the gap just large enough to successfully predict the tangential force felt by an obliquely colliding smooth particle.

In order to quantify the effect of the wall on the observed slowdown of the particles for $St < 70$, a modified expression based on the theoretical analysis done by Brenner was proposed. The modified expression is based on the assumption that the creeping flow solution of a sphere approaching a wall is valid for Reynolds numbers on the order of 100 as long as a modified drag coefficient function of Re is used when calculating the drag. The predictions from this model provide, to a good approximation, an explanation of the observed slowdown of a particle in the range of St from 10 to 70.

The analysis of the particle slowdown was used in an attempt to predict erosion rates in particulate flows. In erosion problems, the wear of a surface depends upon several factors, including the fluid flow conditions, the impacting particle material properties, and the surface properties of the eroded object. While the material properties can be determined from independent measurements, the flow conditions are in general much harder to evaluate. Existing theories on the wear of plastic surfaces were combined with the predictions from the model obtained for the slowdown of a particle discussed above. The size of the crater formed by the impact of a single particle against a ductile target was estimated to good agreement with experimental data in the literature.

7.2 Future directions

The complexity of the flow field around the particle affects the nature of the rebound. For the larger Stokes numbers studied in this thesis, the model presented in §5.1 is not able to accurately predict the effect of the wall due to the unsteady nature of the flow field. Further analysis of the flow around the particle could prove useful towards understanding the full range of collisional conditions that may be encountered in applications.

Several questions are raised by the observed structure of the wake. One of them has to do with the heat transfer related to a collision. In §4.4, a bound on the temperature increase of the liquid in a lubricated collision was estimated. It was mentioned there that the convective cooling is generally negligible during a collision, due to the time and length scales involved. In the big picture, however, convection may be a key player. As the wake moves past a sphere bouncing off a wall, it carries fluid from the bulk of the system toward the wall. Once the particle has moved away, the wake left behind persists for a considerable amount of time. The mixing of the fluid originally near the wall with fluid from several particle diameters into the flow may considerably impact the thermal distribution of a solid–liquid system. A greater understanding of the energy transfer could prove useful in studying several industrial processes.

Also of interest, and not explored in this thesis, is the problem of the impact between two particles. The results obtained here for single-particle collisions should be applicable within certain bounds to collisions between two particles, with some additional complexities. For instance, the added mass effect responsible for the particle slowdown described in §5.1 can be expected to induce a long-range interaction between the particles.

As was mentioned in the Introduction, it is not uncommon for existing numerical simulations of solid–liquid flows to introduce a repulsive force that prevents contact between two solid surfaces. The repulsive force is introduced to prevent the model of the surrounding fluid from breaking down as the gap separation between the surfaces tends to zero. A simple model like the one presented in §3.3 may prove useful towards improving the computational efficiency of such numerical simulations, with little or no sacrifice of the physical accuracy of the model.

The predictions of crater diameter size presented in Chapter 6 were compared with the experimental results obtained by Clark. However, no experimental measurement of crater diameters was performed during the course of the present work. In order to better validate the predictions made, an experimental study of erosion based on the pendular setup would be ideal. Under the controlled conditions provided by the pendulum, a systematic study of the effects of impact angle, incident velocity, and surrounding fluids could further expand the present knowledge in the field of erosion in fluid–particle systems.

Appendix A

Sample preparation

The pendulums used in the experiments were made by attaching thin fly-fishing casting lines to the various spheres with cyanoacrylate contact glue. The procedure for making one pendulum follows:

1. Clean and degrease the sphere. In general, acetone should be used to clean the spheres; acetone dissolves any cyanoacrylate glue that might have been left behind on the sphere from a previous experiment. For plastic spheres soluble in acetone, the cleaning and degreasing should instead be done with isopropanol.

2. Dry and wipe the sphere with a lint-free cloth or lens-cleaning paper.

3. Place the sphere on a washer on the lab bench, to prevent it from rolling.

4. Apply a small drop of cyanoacrylate glue to the top of the sphere, as shown in Figure A.1(a).

5. Hold the fishing line vertically with its tip in the middle of the drop of glue. The line should be held perpendicular to the surface of the sphere such that the tip barely touches the sphere.

6. With a pair of tweezers, hold the string in place as shown in Figure A.1(b).

7. Let the assembly sit still for at least 24 hours.

8. Carefully remove the tweezers and lift the assembly by the fishing line. The sphere should at this point be firmly attached to the string.

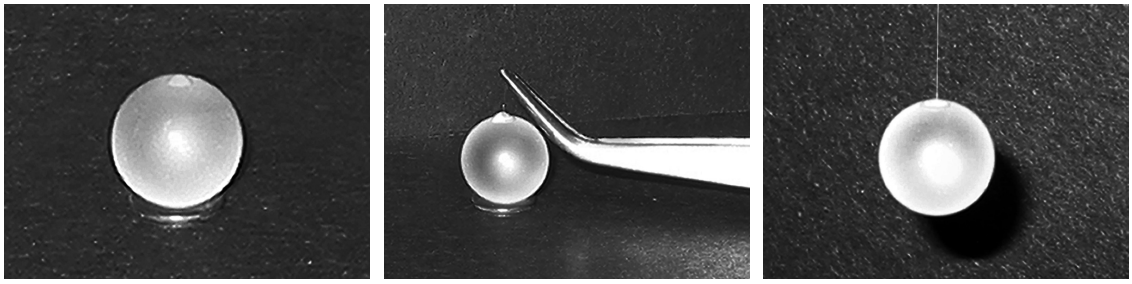

(a) Glue droplet (b) Pendulum assembly (c) A finished pendulum

Figure A.1: Attachment of a nylon string to a steel ball bearing.

9. Immerse the sphere in water. Any remaining acetone in the cyanoacrylate glue will promptly dissolve in the water, strengthening the bond.

10. Dry the sphere with a lint-free cloth or lens-cleaning paper.

11. Inspect the attachment point. If any defects are present, detach the string and repeat the entire process. A small deviation of the string from the perpendicular is acceptable, and can be corrected by hand by bending the string.

A finished pendulum looks like the one shown in Figure A.1(c). It should be noted that the first 12 hours of the glue curing time are particularly critical; any strong vibration or inadvertent motion may move the tweezers relative to the sphere and break the bond. A clean, out of the way area is best for sample preparation.

Appendix B

Particle tracking algorithm

In order to track the position and rotation of the particles in the experiments, high-speed video imaging was used. The individual events, captured with a high-speed video camera, were archived to **S-VHS** tape at a playback rate of 10 frames per second. The taped video was then digitized using a Power Macintosh G3 with an Audio/Video Personality Card and saved as an uncompressed AVI movie.

B.1 Methodology

Full-resolution uncompressed AVI movies were chosen for the processing of the high-speed video because they can be readily imported into MATLAB[1] for subsequent processing. The high-speed camera used, a Redlake *Motion*Scope® 8000S, is a black-and-white camera with an 8-bit sensor. In order to preserve as much information as possible, the AVI movies were encoded using 65 536 shades of gray.

The lighting of the experimental setup was done in such a way that the background of the recorded images appeared dark and defocused, as seen in Figure B.1(a). Once the full-resolution AVI movie had been read into MATLAB, each frame of the movie was processed as an individual image. The contrast of each image was enhanced by mapping the darkest shade of gray in the image to black and the lightest one to white, to take advantage of the full black–white dynamic range. Figure B.1(b) shows the result of applying this contrast enhancement to the image in Figure B.1(a). The particle edges were then found using the

[1] MATLAB® is a registered trademark of The MathWorks, Inc.

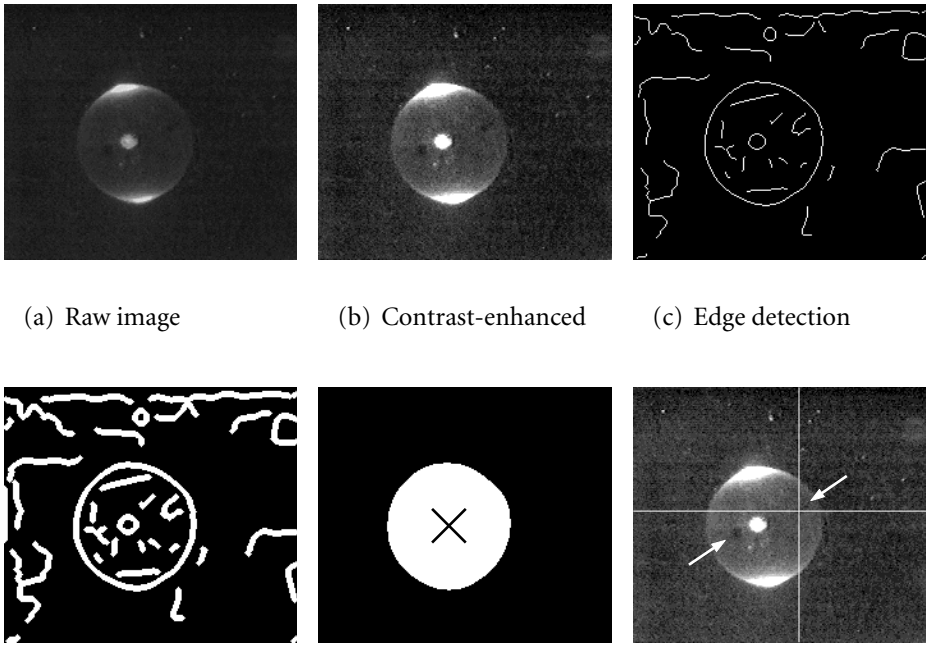

(a) Raw image (b) Contrast-enhanced (c) Edge detection

(d) Dilated edges (e) Tracked disk (f) Angular orientation

Figure B.1: Tracking of the position and angular orientation of a sphere using MATLAB.

method proposed by Canny (1986), as implemented in the Image Processing Toolbox for MATLAB.

The Canny method detects edges in an image by identifying local maxima in the gradient of the intensity of the image. The gradient is calculated using the derivative of a Gaussian filter and is compared with two thresholds. Edges identified using the low threshold are included in the output only if they are connected to edges identified using the high threshold.

The raw edge image, shown in Figure B.1(c), consists of lines of one pixel in width. Such lines do not necessarily form a closed path. Since the edge of a tracked sphere should always form a closed path, the detected edges were dilated by replacing all black pixels adjacent to a white pixel with white pixels. The resulting image is shown in Figure B.1(d). The interior of the closed path was then filled with white and the edges of the disk obtained were eroded to remove the white pixels that had been artificially introduced by the dilation.

The resulting black-and-white image, shown in Figure B.1(e), is internally represented

by MATLAB as a binary matrix. Each number 1 indicates a pixel of the tracked sphere and each number 0 indicates a pixel of the background. The averages by rows and columns of the indices of all the 1-valued pixels correspond to the horizontal and vertical coordinates of the centroid of the tracked sphere, respectively. The black cross shown in Figure B.1(e) indicates the position of the centroid of the sphere. The method described above is implemented in the function `track`, listed in §B.2.1.

Two black dots were painted on each sphere at almost diametrically opposing locations, like those shown by the arrows in Figure B.1(f). These dots were used to determine the angular orientation of the sphere. The coordinates of each dot were determined within MATLAB using the mouse as an input device. The cross-hair lines shown in Figure B.1(f) indicate the position of the cursor at the time when the rightmost point was selected. From the slope of a line joining the two selected points, the angular orientation of the particle was determined. This process is implemented in the function `rotmeas`, listed in §B.2.2.

B.2 Source code

B.2.1 Tracking of the particle translation (`track.m`)

The following MATLAB function takes as input a set of MAT-files that contain frames from an AVI movie. The output is a data structure that contains a sub-structure with the coordinates of the centroid of the tracked particle, a sub-structure with the dimensions of the particle, and two vectors with the number of frames tracked and skipped. The function includes documentation that can be accessed through the `help` command in MATLAB.

```
function particle = track(name,range,step,cut)
% TRACK – Tracks a particle using frames from an AVI movie
%   TRACK(NAME,RANGE,STEP,CUT) returns a data structure with the
%   substructures GEOM and POS, and with two vectors: a vector of
%   FRAME numbers and a vector of SKIPped frames.
%
%   The structure GEOM contains vectors for WIDTH and HEIGHT of the
%   analyzed FRAMEs.
%
%   The structure POS contains the position vectors X and Y for the
%   center of the particle.
%
```

```
%   See also ROTMEAS.

%   Gustavo Joseph, 25 January 2003

if nargin == 3, cut=0; end %% i.e., no wall clip mask

start = min(range);
finish = max(range);

NumFrames = finish - start + 1;

%%%%%
%% initialize variables
%%%%%

%% Thresholds for detecting skipped frames (raw) and for dealing
%% with non-uniform lighting conditions
thresh.raw = 0.82;
thresh.top = 1.0;
thresh.bot = 1.0;
thresh.split = 0.45;
thresh.perc=thresh.top;

%% Position and dimensions of the video image
orig.x = 40;
orig.y = 27;
mask.w = 230;
mask.h = 200;

%% Masks for obscuring the target wall
mask.clos = round(0.4*mask.h):round(0.6*mask.h);
mask.cut = cut;
rect = [orig.x+mask.cut orig.y mask.w-1-mask.cut mask.h-1];
frame.mask = ones(mask.h,mask.w-mask.cut);

%% Structuring elements for particle tracking
seex = strel('disk',2,0);
sere = strel('disk',35,0);

%% Counters
frame.prev = 0;
frame.bw.prev = 0;
frame.num = start - 1;
skip = 0; %% count of skipped frames

%%%%%
%% Frames input
%%%%%

frame.info = aviinfo(name);

if start>frame.info.NumFrames,
  error(['Movie contains ',num2str(frame.info.NumFrames),' frames']);
```

```
end

if finish>frame.info.NumFrames, finish=frame.info.NumFrames; end

%% The AVI movie is saved as a series of MAT-files, each one with
%% 100 frames. Segments is a vector which states how many frames
%% to read from the respective MAT-file
segments = nonzeros( [ (mod(-start,100)+1); ones( ( NumFrames - ...
      mod(-start,100) - 1 - mod(finish,100) ) / 100 , 1)*100; ...
      mod(finish,100) ] );

if NumFrames<100 & ceil(start/100)==ceil(finish/100) ,
 segments = [ NumFrames ];
end

H.debug = 0;
%H.debug = figure; %% Uncomment this line for debugging

%%%%%
%% Tracking body
%%%%%

for ind1 = 1:length(segments),

 block = ceil(ind1 - 1 + start/100); %% segment number for filename

 load(['frames/frames',num2str(block),'.mat']);

 if ind1 == 1,
  if ceil(start/100)==ceil(finish/100),
   low = start - 100*floor((start-1)/100);
  else
   low = 101 - segments(ind1);
  end
  offset = low - 1; %% offset of start of the first frame segment
  high = low + segments(ind1) - 1;
 else
  low = 1;
  high = segments(ind1);
 end

 %% Loop through the frames in this segment
 for ind2 = low:high,

  count = (ind1 - 1)*100 + ind2;
  F = mov(ind2);
  [frame.raw,map] = frame2im(F);
  frame.curr = ind2gray(frame.raw,map);
  frame.bw.curr = im2bw(frame.curr,thresh.raw);

  if frame.bw.curr == frame.bw.prev,
   disp(['Skipped repeated frame ' num2str(count)])
   skip = skip + 1;
```

```
else
  frame.num = frame.num + 1;
  if mod(frame.num,step) == 0,
    %% this frame will be tracked
    ind = count - skip - offset;

    %% Remove image border
    frame.crop = imcrop(frame.curr,rect);

    %% Equalize image to a uniform level of grey
    thresh.level = graythresh(histeq(frame.crop))*thresh.perc;

    %% Detect particle edges
    frame.bw.crop = edge(frame.crop,'canny',[],2.0);
    %% Remove edges that correspond to the target wall
    frame.bw.crop = frame.bw.crop & frame.mask;
    %% Remove shadow from target wall
    frame.bw.crop(mask.clos,1) = 1;

    %% Dilate the image to ensure that the edge is a closed path
    frame.bw.crop = imdilate(frame.bw.crop,seex);
    %% Fill the closed paths, hence locating the particle
    frame.bw.crop = imfill(frame.bw.crop, 'holes');

    %% Remove pixels artificially added to eliminate wall shadow
    frame.bw.crop(mask.clos,1) = 0;
    %% Add pixels with luminance larger than thresh.level
    frame.bw.crop = frame.bw.crop | im2bw(frame.crop,thresh.level);

    %% Filter out edge noise
    frame.bw.crop = imopen(frame.bw.crop,sere);

    %% If debugging is enabled, display tracked image
    if H.debug ~= 0,
      figure(H.debug);
      imshow(double(frame.bw.crop) );
      daspect([1 1 1]);
    end

    %% Compute particle dimensions and centroid coordinates
    [i,j]=find(frame.bw.crop);

    %% If no pixels are found, the frame is skipped
    if isempty(i)
      skip = skip + 1;
    else

      %% Horizontal dimensions
      xmin = min(j) - 1;
      xmax = max(j) + 1;
      particle.geom.width(ind) = xmax - xmin;

      %% Vertical dimensions
```

```
          ymin = min(i) - 1;
          ymax = max(i) + 1;
          particle.geom.height(ind) = ymax - ymin;

          %% Centroid coordinates
          particle.pos.x(ind) = mean(j);
          particle.pos.y(ind) = mask.h - mean(i);

          %% If the partcle has crossed into a different illumination
          %% zone, change the threshold value
          if particle.pos.y(ind) < (thresh.split*mask.h),
            thresh.perc = thresh.bot;
          end

          particle.frame(ind) = frame.num;
          particle.skip(ind) = skip; %% number of frames skipped so far

        end
      else
        %% this frame was skipped
        skip = skip + 1;
      end
    end
    frame.bw.prev = frame.bw.curr;
  end
end

%% number of frames skipped between the previous frame and this one
particle.skip = diff([0 particle.skip]);

%% Wait for a second before closing the debugging image
if H.debug ~= 0,
  pause(1);
  close(H.debug);
end
```

B.2.2 Tracking of the particle rotation (`rotmeas.m`)

The following MATLAB function takes the data structure generated by the particle translation tracking function `track` listed above and adds to it three sub-structures containing the orientation angle of the tracked particle and the coordinates of the points used for tracking the angular orientation. The function includes documentation that can be accessed through the `help` command in MATLAB.

```
function particle = rotmeas(name,frames,skipped,cut)
% ROTMEAS - Angle with respect to the horizontal from an AVI movie
%   ROTMEAS(NAME,FRAMES,SKIPPED,CUT) returns a data structure with
```

```
%   the substructures POS, DOT1 and DOT2.
%
%   The input consists of the NAME of the AVI movie to use, a vector
%   with the FRAMES to read, a vector detailing SKIPPED frames during
%   the original tracking, and an optional integer CUT declaring the
%   masking for eliminating the wall from the image. Very few error
%   checks are performed. It is the responsibility of the previous
%   tracking to provide reliable FRAMES and SKIPPED information.
%
%   The structure POS contains the position vectors X and Y for the
%   center of the particle, as well as a crude value for the
%   orientation ANGLE. A value of -1 in the ANGLE is used to
%   signify that an error occured when determining the angle.
%
%   The structures DOT1 and DOT2 contain the position vectors
%   X and Y for the orientation tracking marks that are painted
%   on the particle for the experiment.
%
%   See also TRACK.

%   Gustavo Joseph, 25 January 2003

if nargin == 3, cut=0; end %% no wall clip mask

NumFrames = length(frames);

if length(skipped) ~= NumFrames,
  error('Incorrect number of SKIP elements.');
end

frames = frames + cumsum(skipped);

start = min(frames);
finish = max(frames);

%%%%%
%% initialize variables
%%%%%

%% Position and dimensions of the video image
orig.x = 40;
orig.y = 27;
mask.w = 230;
mask.h = 200;

%% Masks for obscuring the target wall
mask.cut = cut;
rect = [orig.x+mask.cut orig.y mask.w-1-mask.cut mask.h-1];
frame.mask = ones(mask.h,mask.w-mask.cut);

%%%%%
%% Frames input
%%%%%
```

```
%% The AVI movie is saved as a series of MAT-files, each one with
%% 100 frames. Segments is a vector which states how many frames
%% to read from the respective MAT-file
segments = nonzeros( [ (mod(-start,100)+1); ones( ( NumFrames - ...
      mod(-start,100) - 1 - mod(finish,100) ) / 100 , 1)*100; ...
      mod(finish,100) ] );

if NumFrames<100 & ceil(start/100)==ceil(finish/100),
  segments = [ NumFrames ];
end

%% Initialize figure. Black background is easier on the eyes
H.finds = figure;
whitebg(1,'black')
count = 0;

%%%%%
%% Tracking body
%%%%%

for ind1 = 1:length(segments),

  block = ceil(ind1 - 1 + start/100); %% segment number for filename

  load(['frames/frames',num2str(block),'.mat']);

  low = sum( frames <= 100*(block-1) ) + 1;
  high = sum( frames <= 100*block ) ;

  %% Loop through the frames in this segment
  for ind2 = low:high,

    ind = mod( frames(ind2) - 1, 100 ) + 1;

    F = mov(ind);
    [frame.raw,map] = frame2im(F);
    [frame.curr,map]=cmunique(frame.raw,map);

    frame.curr = imcrop(frame.curr,rect);

    %% Pink makes the dots easy to see on screen
    colormap(pink)

    %% Display particle with a natural aspect ratio
    imagesc(frame.curr);
    daspect([1 1 1]);

    %% Read two sets of coordinates from mouse input
    [x,y]=ginput(2);

    count = count + 1;
```

```
    %% Compute angle between the dots from the mouse input
    if (x(1)==x(2) & y(1)==y(2)),
      particle.pos.ang(count) = -1;
    else
      particle.pos.ang(count) = atan2(y(2)-y(1),x(1)-x(2)) ...
                            *180/pi ... %% angle in degrees
                            + 180; %% from 0 to 360
    end
    particle.dot1.x(count) = x(1);
    particle.dot1.y(count) = y(1);
    particle.dot2.x(count) = x(2);
    particle.dot2.y(count) = y(2);

  end
end

%% Close figure with particle image
close(H.finds);
```

Appendix C

Physical properties of glycerol

Glycerol (1,2,3-propanetriol) is a liquid at room temperature. Commonly known as glycerin, it has a molecular weight of 92.09 g mol^{-1}. It is viscous, stable, hygroscopic, clear, odorless, noncorrosive, sweet tasting, very low in toxicity, and is classified by the Food and Drug Administration as "Generally Recognized As Safe" (GRAS). It has a freezing point of 17°C and a boiling point at atmospheric pressure of 290°C.

Glycerol is fully miscible with water, and a common means of determining the glycerol content of an aqueous solution is to measure the specific gravity of the mixture. Table C.1 shows the density of glycerol–water solutions at various concentrations and temperatures, from which the true specific gravity—the ratio of the weight of a glycerol–water mixture to the weight of an equal volume of pure water at its maximum density—can be calculated. Table C.2 shows the apparent specific gravity—as measured by a hydrometer—of aqueous solutions of glycerol up to 80% glycerol by weight. These tables are taken from data sheets provided by Dow Chemical Synthetic Glycerine Products and are in agreement with the tabulated data presented by Green and Maloney (1997).

The viscosity of aqueous glycerol solutions from 0 to 100% concentrations and 0 to 70°C temperatures is given in Table C.3. These data, also from The Dow Chemical Company, are in agreement with those reported by Lide (2001). Once the concentration of glycerol has been determined from Table C.2 by means of a hydrometer, the viscosity of the mixture can be determined from the tabulated data.

Table C.1: Density of glycerol–water solutions.

Glycerol	Density ($g\,cm^{-3}$)				
(% wt.)	15°C	15.5°C	20°C	25°C	30°C
100	1.26415	1.26381	1.26108	1.25802	1.25495
99	1.26160	1.26125	1.25850	1.25545	1.25235
98	1.25900	1.25865	1.25590	1.25290	1.24975
97	1.25645	1.25610	1.25335	1.25030	1.24710
96	1.25385	1.25350	1.25080	1.24770	1.24450
95	1.25130	1.25095	1.24825	1.24515	1.24190
94	1.24865	1.24830	1.24560	1.24250	1.23930
93	1.24600	1.24565	1.24300	1.23985	1.23670
92	1.24340	1.24305	1.24035	1.23725	1.23410
91	1.24075	1.24040	1.23770	1.23460	1.23150
90	1.23810	1.23775	1.23510	1.23200	1.22890
89	1.23545	1.23510	1.23245	1.22935	1.22625
88	1.23280	1.23245	1.22975	1.22665	1.22360
87	1.23015	1.22980	1.22710	1.22400	1.22095
86	1.22750	1.22710	1.22445	1.22135	1.21830
85	1.22485	1.22445	1.22180	1.21870	1.21565
84	1.22220	1.22180	1.21915	1.21605	1.21300
83	1.21955	1.21915	1.21650	1.21340	1.21035
82	1.21690	1.21650	1.21380	1.21075	1.20770
81	1.21425	1.21385	1.21115	1.20810	1.20505
80	1.21160	1.21120	1.20850	1.20545	1.20240
79	1.20885	1.20845	1.20575	1.20275	1.19970
78	1.20610	1.20570	1.20305	1.20005	1.19705
77	1.20335	1.20300	1.20030	1.19735	1.19435
76	1.20060	1.20025	1.19760	1.19465	1.19170
75	1.19785	1.19750	1.19485	1.19195	1.18900
74	1.19510	1.19480	1.19215	1.18925	1.18635
73	1.19235	1.19205	1.18940	1.18650	1.18365
72	1.18965	1.18930	1.18670	1.18380	1.18100
71	1.18690	1.18655	1.18395	1.18110	1.17830
70	1.18415	1.18385	1.18125	1.17840	1.17565
69	1.18135	1.18105	1.17850	1.17565	1.17290
68	1.17860	1.17830	1.17575	1.17295	1.17020
67	1.17585	1.17555	1.17300	1.17020	1.16745
66	1.17305	1.17275	1.17025	1.16745	1.16470
65	1.17030	1.17000	1.16750	1.16475	1.16195
64	1.16755	1.16725	1.16475	1.16200	1.15925
63	1.16480	1.16445	1.16205	1.15925	1.15650
62	1.16200	1.16170	1.15930	1.15655	1.15375
61	1.15925	1.15895	1.15655	1.15380	1.15100
60	1.15650	1.15615	1.15380	1.15105	1.14830
59	1.15370	1.15340	1.15105	1.14835	1.14555
58	1.15095	1.15065	1.14830	1.14560	1.14285
57	1.14815	1.14785	1.14555	1.14285	1.14010
56	1.14535	1.14510	1.14280	1.14015	1.13740
55	1.14260	1.14230	1.14005	1.13740	1.13470
54	1.13980	1.13955	1.13730	1.13465	1.13195
53	1.13705	1.13680	1.13455	1.13195	1.12925
52	1.13425	1.13400	1.13180	1.12920	1.12650
51	1.13150	1.13125	1.12905	1.12650	1.12380

continued on next page

Table C.1: *continued from previous page*

Glycerol	Density ($g\,cm^{-3}$)				
(% wt.)	15°C	15.5°C	20°C	25°C	30°C
50	1.12870	1.12845	1.12630	1.12375	1.12110
49	1.12600	1.12575	1.12360	1.12110	1.11845
48	1.12325	1.12305	1.12090	1.11840	1.11580
47	1.12055	1.12030	1.11820	1.11575	1.11320
46	1.11780	1.11760	1.11550	1.11310	1.11055
45	1.11510	1.11490	1.11280	1.11040	1.10795
44	1.11235	1.11215	1.11010	1.10775	1.10530
43	1.10960	1.10945	1.10740	1.10510	1.10265
42	1.10690	1.10670	1.10470	1.10240	1.10005
41	1.10415	1.10400	1.10200	1.09975	1.09740
40	1.10145	1.10130	1.09930	1.09710	1.09475
39	1.09875	1.09860	1.09665	1.09445	1.09215
38	1.09605	1.09590	1.09400	1.09180	1.08955
37	1.09340	1.09320	1.09135	1.08915	1.08690
36	1.09070	1.09050	1.08865	1.08655	1.08430
35	1.08800	1.08780	1.08600	1.08390	1.08165
34	1.08530	1.08515	1.08335	1.08125	1.07905
33	1.08265	1.08245	1.08070	1.07860	1.07645
32	1.07995	1.07975	1.07800	1.07600	1.07380
31	1.07725	1.07705	1.07535	1.07335	1.07120
30	1.07455	1.07435	1.07270	1.07070	1.06855
29	1.07195	1.07175	1.07010	1.06815	1.06605
28	1.06935	1.06915	1.06755	1.06560	1.06355
27	1.06670	1.06655	1.06495	1.06305	1.06105
26	1.06410	1.06390	1.06240	1.06055	1.05855
25	1.06150	1.06130	1.05980	1.05800	1.05605
24	1.05885	1.05870	1.05720	1.05545	1.05350
23	1.05625	1.05610	1.05465	1.05290	1.05100
22	1.05365	1.05350	1.05205	1.05035	1.04850
21	1.05100	1.05090	1.04950	1.04780	1.04600
20	1.04840	1.04825	1.04690	1.04525	1.04350
19	1.04590	1.04575	1.04440	1.04280	1.04105
18	1.04335	1.04325	1.04195	1.04035	1.03860
17	1.04085	1.04075	1.03945	1.03790	1.03615
16	1.03835	1.03825	1.03695	1.03545	1.03370
15	1.03580	1.03570	1.03450	1.03300	1.03130
14	1.03330	1.03320	1.03200	1.03055	1.02885
13	1.03080	1.03070	1.02955	1.02805	1.02640
12	1.02830	1.02820	1.02705	1.02560	1.02395
11	1.02575	1.02565	1.02455	1.02315	1.02150
10	1.02325	1.02315	1.02210	1.02070	1.01905
9	1.02085	1.02075	1.01970	1.01835	1.01670
8	1.01840	1.01835	1.01730	1.01600	1.01440
7	1.01600	1.01590	1.01495	1.01360	1.01205
6	1.01360	1.01350	1.01255	1.01125	1.00970
5	1.01120	1.01110	1.01015	1.00890	1.00735
4	1.00875	1.00870	1.00780	1.00655	1.00505
3	1.00635	1.00630	1.00540	1.00415	1.00270
2	1.00395	1.00385	1.00300	1.00180	1.00035
1	1.00155	1.00145	1.00060	0.99945	0.99800
0	0.99913	0.99905	0.99823	0.99708	0.99568

Table C.2: Specific gravity of glycerol–water solutions.

Glycerol	Apparent specific gravity			
(% wt.)	15/15°C	15.5/15.5°C	20/20°C	25/25°C
80	1.21290	1.21260	1.21090	1.20925
79	1.21015	1.20985	1.20815	1.20655
78	1.20740	1.20710	1.20540	1.20380
77	1.20465	1.20440	1.20270	1.20110
76	1.20190	1.20165	1.19995	1.19840
75	1.19915	1.19890	1.19720	1.19565
74	1.19640	1.19615	1.19450	1.19295
73	1.19365	1.19340	1.19175	1.19025
72	1.19090	1.19070	1.18900	1.18755
71	1.18815	1.87950	1.18630	1.18480
70	1.18540	1.18520	1.18355	1.18210
69	1.18260	1.18240	1.18080	1.17935
68	1.17985	1.17965	1.17805	1.17660
67	1.17705	1.17685	1.17530	1.17385
66	1.17430	1.17410	1.17255	1.17110
65	1.17155	1.17130	1.16980	1.16835
64	1.16875	1.16855	1.16705	1.16560
63	1.16600	1.16575	1.16430	1.16285
62	1.16320	1.16300	1.16155	1.16010
61	1.16045	1.16020	1.15875	1.15735
60	1.15770	1.15745	1.15605	1.15460
59	1.15490	1.15465	1.15325	1.15185
58	1.15210	1.15190	1.15050	1.14915
57	1.14935	1.14910	1.14775	1.14640
56	1.14655	1.14635	1.14500	1.14365
55	1.14375	1.14355	1.14220	1.14090
54	1.14100	1.14080	1.13945	1.13815
53	1.13820	1.13800	1.13670	1.13540
52	1.13540	1.13525	1.13395	1.13265
51	1.13265	1.13245	1.13120	1.12995
50	1.12985	1.12970	1.12845	1.12720
49	1.12710	1.12695	1.12570	1.12450
48	1.12440	1.12425	1.12300	1.12185
47	1.12165	1.12150	1.12030	1.11915
46	1.11890	1.11880	1.11760	1.11650
45	1.11620	1.11605	1.11490	1.11380
44	1.11345	1.11335	1.11220	1.11115
43	1.11075	1.11060	1.10950	1.10845
42	1.10800	1.10790	1.10680	1.10575
41	1.10525	1.10515	1.10410	1.10310

continued on next page

Table C.2: *continued from previous page*

Glycerol	Apparent specific gravity			
(% wt.)	15/15°C	15.5/15.5°C	20/20°C	25/25°C
40	1.10255	1.10245	1.10135	1.10040
39	1.09985	1.09975	1.09870	1.09775
38	1.09715	1.09705	1.09605	1.09510
37	1.09445	1.09435	1.09335	1.09245
36	1.09175	1.09165	1.09070	1.08980
35	1.08905	1.08895	1.08805	1.08715
34	1.08635	1.08625	1.08535	1.08455
33	1.08365	1.08355	1.08270	1.08190
32	1.08100	1.08085	1.08005	1.07925
31	1.07830	1.07815	1.07735	1.07660
30	1.07560	1.07545	1.07470	1.07395
29	1.07295	1.07285	1.07210	1.07135
28	1.07035	1.07025	1.06950	1.06880
27	1.06770	1.06760	1.06690	1.06625
26	1.06510	1.06500	1.06435	1.06370
25	1.06250	1.06240	1.06175	1.06115
24	1.05985	1.05980	1.05915	1.05860
23	1.05725	1.05715	1.05655	1.05605
22	1.05460	1.05455	1.05400	1.05350
21	1.05200	1.05195	1.05140	1.05095
20	1.04935	1.04935	1.04880	1.04840
19	1.04685	1.04680	1.04630	1.04590
18	1.04435	1.04430	1.04380	1.04345
17	1.04180	1.04180	1.04135	1.04100
16	1.03930	1.03925	1.03885	1.03850
15	1.03675	1.03675	1.03635	1.03605
14	1.03425	1.03420	1.03390	1.03360
13	1.03175	1.03170	1.03140	1.03110
12	1.02920	1.02920	1.02890	1.02865
11	1.02670	1.02665	1.02640	1.02620
10	1.02415	1.02415	1.02395	1.02370
9	1.02175	1.02175	1.02155	1.02135
8	1.01935	1.01930	1.01915	1.01900
7	1.01690	1.01690	1.01675	1.01660
6	1.01450	1.01450	1.01435	1.01425
5	1.01210	1.01205	1.01195	1.01185
4	1.00965	1.00965	1.00955	1.00950
3	1.00725	1.00725	1.00720	1.00710
2	1.00485	1.00485	1.00480	1.00475
1	1.00240	1.00240	1.00240	1.00235

Table C.3: Viscosity of glycerol–water solutions.

Glycerol	Viscosity (cP)[†]							
(% wt.)	10°C	20°C	25°C	30°C	40°C	50°C	60°C	70°C
100	3900	1410	906	612	284	142	81.3	50.6
99	3090	1150	743	500	235	122	69.1	43.6
98	2460	939	603	409	196	104	59.8	38.5
97	1950	765	501	340	166	88.9	51.9	33.6
96	1580	624	417	281	142	77.8	45.4	29.7
95	1270	523	350	237	121	67.0	39.9	26.4
94	1040	437	296	202	105	58.4	35.4	23.6
93	860	367	251	172	89	51.5	31.6	21.2
92	729	310	213	147	78.3	44.8	28.0	19.0
91	592	259	181	127	68.1	39.8	25.1	17.1
90	498	219	157	109	60.0	35.5	22.5	15.5
85	223	109	78	58	33.5	21.2	14.2	10.0
80	116	60.1	45.3	33.9	20.8	13.6	9.42	6.94
75	65.2	35.5	27.1	21.2	13.6	9.25	6.61	5.01
70	38.8	22.5	17.6	14.1	9.40	6.61	4.86	3.78
65	25.3	15.2	12.06	9.85	6.80	4.89	3.66	2.91
60	17.4	10.8	8.673	7.19	5.08	3.76	2.85	2.29
50	9.01	6.00	5.041	4.21	3.10	2.37	1.86	1.53
40	5.37	3.72	3.181	2.72	2.07	1.62	1.30	1.09
30	3.49	2.50	2.157	1.87	1.46	1.16	0.956	0.816
20	2.41	1.76	1.542	1.35	1.07	0.879	0.731	0.635
10	1.74	1.31	1.153	1.03	0.826	0.680	0.575	0.500
0	1.308	1.005	0.893	0.800	0.656	0.549	0.469	0.406

[†] $1\,\mathrm{cP} = 1\times10^{-3}\,\mathrm{Pa\cdot s}$.

Bibliography

R. K. Adair (2002). *The Physics of Baseball*, 3rd edn. New York: Perennial.

G. Barnocky and R. H. Davis (1988). Elastohydrodynamic collision and rebound of spheres: experimental verification. *Phys. Fluids* **31**(6), 1324–1329.

G. Barnocky and R. H. Davis (1989). The influence of pressure-dependent density and viscosity on the elastohydrodynamic collision and rebound of two spheres. *J. Fluid Mech.* **209**, 501–519.

J. G. A. Bitter (1963). A study of erosion phenomena. *Wear* **6**, 5–21, 169–190.

F. P. Bowden and D. Tabor (1950). *The Friction and Lubrication of Solids*. Oxford: Clarendon Press.

H. Brenner (1961). The slow motion of a sphere through a viscous fluid towards a plane surface. *Chem. Engng Sci.* **16**, 242–251.

L. J. Briggs (1945). Methods for measuring the coefficient of restitution and the spin of a ball. *J. Res. Nat. B. of Standards* **34**(RP1624), 1–23.

A. Cameron (1981). *Basic Lubrication Theory*, 3rd edn. Chichester: Ellis Horwood Ltd.

J. Canny (1986). A computational approach to edge-detection. *IEEE T. Pattern Anal.* **8**(6), 679–698.

R. W. Carpick, D. F. Ogletree, and M. Salmeron (1997). Lateral stiffness: A new nanomechanical measurement for the determination of shear strengths with friction force microscopy. *Appl. Phys. Lett.* **70**(12), 1548–1550.

A. ten Cate, C. H. Nieuwstad, J. J. Derksen, and H. E. A. Van den Akker (2002). Particle imaging velocimetry experiments and lattice-Boltzmann simulations on a single sphere settling under gravity. *Phys. Fluids* **14**(11), 4012–4025.

C. Cattaneo (1938). Sul contatto di due corpi elastici: distribuzione locale degli sforzi. *Accademia dei Lincei, Rendiconti, series 6* **XXVII**, 342–348, 434–436, 474–478.

P. S. Y. Chu and A. Cameron (1962). Pressure viscosity characteristics of lubricating oils. *J. Inst. Petrol.* **48**(461), 147–155.

H. M. Clark (1991). On the impact rate and impact energy of particles in a slurry pot erosion tester. *Wear* **147**(1), 165–183.

R. Clift, J. R. Grace, and M. E. Weber (1978). *Bubbles, Drops, and Particles*. New York: Academic Press.

J. Colchero, M. Luna, and A. M. Baró (1996). Lock-in technique for measuring friction on a nanometer scale. *Appl. Phys. Lett.* **68**(20), 2896–2898.

R. M. Davies (1949). The determination of static and dynamic yield stresses using a steel ball. *Proc. R. Soc. Lond.* A **197**, 416–432.

R. H. Davis, D. A. Rager, and B. T. Good (2002). Elastohydrodynamic rebound of spheres from coated surfaces. *J. Fluid Mech.* **468**, 107–119.

R. H. Davis, J. M. Serayssol, and E. J. Hinch (1986). The elastohydrodynamic collision of two spheres. *J. Fluid Mech.* **163**, 479–497.

W. R. Dean and M. E. O'Neill (1963). A slow motion of viscous liquid caused by a slowly rotating solid sphere. *Mathematika* **10**, 13–24.

I. Eames and S. B. Dalziel (2000). Dust resuspension by the flow around an impacting sphere. *J. Fluid Mech.* **403**, 305–328.

Edmund Scientific (2003). Happy & Unhappy Balls. Scientifics Item No. CR-30391-29. URL <http://www.scientificsonline.com/>

D. Elata (1996). On the oblique compression of two elastic spheres. *Trans. ASME: J. Appl. Mech.* **63**(4), 1039–1041.

I. Finnie (1960). Erosion of surfaces by solid particles. *Wear* **3**(1), 87–103.

I. Finnie and D. H. McFadden (1978). On the velocity dependence of erosion of ductile metals by solid particles at low angles of incidence. *Wear* **48**(1), 181–190.

S. F. Foerster, M. Y. Louge, A. H. Chang, and K. Allia (1994). Measurements of the collision properties of small spheres. *Phys. Fluids* **6**(3), 1108–1115.

R. Glowinski, T. W. Pan, T. I. Hesla, and D. D. Joseph (1999). A distributed Lagrange multiplier fictitious domain method for particulate flows. *Int. J. Multiphas. Flow* **25**(5), 755–794.

R. Gohar (2001). *Elastohydrodynamics*, 2nd edn. London: Imperial College Press.

A. J. Goldman, R. G. Cox, and H. Brenner (1967). Slow viscous motion of a sphere parallel to a plane wall—I. Motion through a quiescent fluid. *Chem. Engng Sci.* **22**(4), 637–651.

W. Goldsmith (1960). *Impact*. London: Edward Arnold Ltd.

P. Gondret, E. Hallouin, M. Lance, and L. Petit (1999). Experiments on the motion of a solid sphere toward a wall: From viscous dissipation to elastohydrodynamic bouncing. *Phys. Fluids* **11**(9), 2803–2805.

P. Gondret, M. Lance, and L. Petit (2002). Bouncing motion of spherical particles in fluids. *Phys. Fluids* **14**(2), 643–652.

D. W. Green and J. O. Maloney, eds. (1997). *Perry's Chemical Engineers' Handbook*, 7th edn. New York: McGraw–Hill.

H. H. Hu (1996). Direct simulation of flows of solid–liquid mixtures. *Int. J. Multiphas. Flow* **22**(2), 335–352.

K. L. Johnson (1985). *Contact Mechanics*. New York: Cambridge University Press.

G. G. Joseph, R. Zenit, M. L. Hunt, and A. M. Rosenwinkel (2001). Particle–wall collisions in a viscous fluid. *J. Fluid Mech.* **433**, 329–346.

H. K. Kytömaa and P. J. Schmid (1992). On the collision of rigid spheres in a weakly compressible fluid. *Phys. Fluids A* **4**(12), 2683–2689.

D. R. Lide, ed. (2001). *CRC Handbook of Chemistry and Physics*, 82nd edn. Boca Raton: CRC Press.

A. E. H. Love (1927). *A Treatise on the Mathematical Theory of Elastisity*, 4th edn. Cambridge University Press.

C. K. K. Lun and S. B. Savage (1987). A simple kinetic theory for granular flow of rough, inelastic, spherical particles. *Trans. ASME: J. Appl. Mech.* **54**(1), 47–53.

J. Lundberg and H. H. Shen (1992). Collisional restitution dependence on viscosity. *J. Engng Mech. Div. ASCE* **118**(5), 979–989.

A. Magnée (1995). Generalized law of erosion—Application to various alloys and intermetallics. *Wear* **181**(2), 500–510.

N. Maw, J. R. Barber, and J. N. Fawcett (1976). The oblique impact of elastic spheres. *Wear* **38**(1), 101–114.

N. Maw, J. R. Barber, and J. N. Fawcett (1981). The role of elastic tangential compliance in oblique impact. *Trans. ASME: J. Lubric. Tech.* **103**(1), 74–80.

M. H. McLaughlin (1968). *An experimental study of particle–wall collision relating to flow of solid particles in a fluid*. Engineer's degree thesis, California Institute of Technology, Pasadena, California.

R. D. Mindlin (1949). Compliance of elastic bodies in contact. *Trans. ASME: J. Appl. Mech.* **16**, 259–268.

R. D. Mindlin and H. Deresiewicz (1953). Elastic spheres in contact under varying oblique forces. *Trans. ASME: J. Appl. Mech.* **20**, 327–344.

N. Nguyen and A. J. C. Ladd (2002). Lubrication corrections for lattice-Boltzmann simulations of particle suspensions. *Phys. Rev. E* **66**, 046708.

M. E. O'Neill (1964). A slow motion of viscous liquid caused by a slowly moving solid sphere. *Mathematika* **11**, 67–74.

M. E. O'Neill (1967). A slow motion of viscous liquid caused by a slowly moving solid sphere: an addendum. *Mathematika* **14**, 170–172.

A. V. Potapov, M. L. Hunt, and C. S. Campbell (2001). Liquid–solid flows using smoothed particle hydrodynamics and the discrete element method. *Powder Tech.* **116**(2–3), 204–213.

Redlake (2002). *Instructions for Operating the MotionScope® S and C Series High Speed Video Cameras*. San Diego. Manual No. 9400-0018, Revision J.

J. R. Smart and D. T. Leighton (1989). Measurement of the hydrodynamic surface-roughness of noncolloidal spheres. *Phys. Fluids A* **1**(1), 52–60.

M. B. Smith and R. R. Hannah (1996). High-permeability fracturing: The evolution of a technology. *J. Pet. Tech.* **48**(7), 628–633.

R. Sondergaard, K. Chaney, and C. E. Brennen (1990). Measurements of solid spheres bouncing off flat plates. *Trans. ASME: J. Appl. Mech.* **57**(3), 694–699.

D. Tabor (1951). *The Hardness of Metals*. Oxford University Press.

T. R. Thomas (1999). *Rough Surfaces*, 2nd edn. London: Imperial College Press.

S. P. Timoshenko and J. N. Goodier (1970). *Theory of Elasticity*, 3rd edn. McGraw–Hill.

K. Walton (1978). The oblique compression of two elastic spheres. *J. Mech. Phys. Solids* **26**(3), 139–150.

O. R. Walton (1993). Numerical simulation of inelastic, frictional particle–particle interactions. In M. C. Roco, ed., *Particulate Two-Phase Flow*, chap. 25, pp. 884–911. Boston: Butterworth–Heinemann.

R. Zenit and M. L. Hunt (1999). Mechanics of immersed particle collisions. *Trans. ASME: J. Fluid Engng* **121**(1), 179–184.

R. Zenit, M. L. Hunt, and C. E. Brennen (1997). Collisional particle pressure measurements in solid–liquid flows. *J. Fluid Mech.* **353**, 261–283.

J. P. Zhang, L. S. Fan, C. Zhu, R. Pfeffer, and D. W. Qi (1999). Dynamic behavior of collision of elastic spheres in viscous fluids. *Powder Tech.* **106**(1–2), 98–109.

This thesis was prepared in LaTeX 2_ε, using the class file written by Daniel M. Zimmerman and available on the Caltech Library System website. It was typeset directly to Adobe Portable Document Format on a Power Macintosh G3 running Mac OS X, using pdfTeX as included in Thomas Esser's teTeX distribution. The figures were prepared using MATLAB® and the schematic diagrams were drawn in Adobe® Illustrator® 10. The `crunch, crunch, crunch...` was done with *MATHEMATICA*® and MATLAB®.

The typeface used for the main text is Minion, designed by Robert Slimbach. The typewriter font is a combination of Courier by Howard Kettler for the upright characters and Lucida Sans Typewriter by Charles Bigelow and Kris Holmes for the slanted characters. The Greek characters and mathematical symbols in formulas are taken from Computer Modern by Donald Knuth, with the exception of the summation symbol, which comes from Adobe Symbol. The font used for text in figures and diagrams is Palatino™ by Hermann Zapf.